Technische Universität München

Fakultät für Elektrotechnik und Informationstechnik

Lehrstuhl für Biologische Bildgebung

3D mesoscopic scale optoacoustic imaging using linear array transducers

Andrei-Chakib Chekkoury-Idrissi

Dedicated to my parents,
Graciela and Abdelhak Chekkoury.

Abstract

In the past decade, mesoscopic imaging received significant attention due to a shift of focus from imaging small transparent samples and parts of organisms to studies of entire organs and animals. In order to capture a more complete picture of the biological phenomena in the entire sample under investigation, traditional optical imaging methods like histological imaging were recently complemented by methods like selective plane illumination microscopy (SPIM) and optical projection tomography (OPT). SPIM and OPT were shown to attain good resolution ($10\,\mu m$) and penetration depth ($500\,\mu m$) in transparent samples, but image performance degrades in scattering samples. For this reason toxic chemical clearing procedures of the sample are performed, limiting the application of these techniques in bigger samples to *ex-vivo* scenarios. Multispectral optoacoustic imaging (MSOT) can provide high-resolution mapping of optical absorption up to a few centimeters depth into tissue, being based on the photoacoustic effect (conversion of pulsed light to ultrasound through optical absorption). Due to light scattering into tissue, optoacoustic imaging is intrinsically a volumetric imaging technique, and OA detection geometries should be matched to record 3D information. Throughout this work, three different volumetric detection geometries are introduced and used to record complex anatomical, molecular, and functional information at mesoscopic scale.

On a first step, I present an OA imaging system using a high-frequency linear array recording volumetric information from small scattering samples. The geometry is implemented in the context of a SPIM microscope, using the thin sheet of light as optical excitation source. The illumination plane is co-aligned with the focal plane of the transducer array, and 3D imaging is obtained by stacking the cross-section images. Merging two imaging modalities can thus provide a combined source of contrast and is suitable for biological studies investigating samples (fish or small organisms) from early up to later stages of development, where the samples become opaque and microscopy techniques are not efficient anymore.

The second part of this work focuses on modeling and hardware integration of two particular OA properties: on one hand, optical excitation of biological tissue with nano-second lasers generates ultrasonic waves with peak frequency corresponding to different object sizes. This effect combined with the recording abilities of ultrasonic detectors like central frequency and recording bandwidth

define the range of structures a transducer can record. On the other hand the positioning of ultrasonic detectors around the sample plays a crucial role in image quality and ultimately on the extracted information content. Accounting for this properties, a second geometry based on a broad illumination system is presented. The implementation uses a dual detector array scanned in a novel tomographic manner, to record volumetric information from intact, non-chemically processed samples. The combination of multispectral optoacoustic mesoscopy techniques using dual detector arrays, revealed novel biological insights in tracking and detecting the localization of nanoparticles and fluorochromes. The detection bandwidth spanned by the system ranges from 0.5 kHz, up to 40 MHz, attaining isotropic in-plane resolution values of $\approx 30\,\mu\text{m}$.

The third detection geometry presented in the current work was developed for *in-vivo* imaging of cancer tumor models. This solution comes as a need to analyze intact subcutaneous or orthotopic tumor models in *in-vivo* organisms, as currently available 3D OA systems are operating in either *ex-vivo* mode, or are too complex for entire volumetric imaging. Moreover, performing longitudinal studies is further simplified by capturing 3D data, reducing the need to consistently select the same plane of imaging in the 2D systems. The presented modality offers the ability to study intact tumors located on the living organisms without interfering with the growth, vascularization or supporting animal. The system extracts volumetric information from implanted tumors, attaining an almost homogeneous resolution of $\approx 80\,\mu\text{m}$ in the entire mesoscopic scale sample ($1\,\text{cm}^3$), opening up a broad range of applications and uses in the context of cancer imaging, drug delivery and treatment monitoring.

Zusammenfassung

Mesoskopische optische Bildgebung hat im letzten Jahrzehnt zunehmende Beachtung gefunden, weil eine Verschiebung der biologischen Herangehensweisen weg von kleinen, transparenten Proben und Schnitten durch Organe hin zu Studien mit intakten Organen oder ganzen Tieren stattgefunden hat. Um ein vollständigeres und genaueres Bild der biologischen Vorgänge in der gesamten untersuchten Probe zu erhalten wurden etablierte optische Bildgebungsmethoden wie die histologische Mikroskopie in den vergangenen Jahren um neue Methoden wie die Lichtblattmikroskopie (SPIM) oder die optische Projektionstomographie (OPT) ergänzt. Mit SPIM und OPT konnten hohe Auflösungen ($10\,\mu$m) und größe Eindringtiefen erreicht werden, jedoch nimmt die Bildqualität in streuenden opaken Proben rasch ab. Deshalb müssen solche Proben mit chemischen Reinigungsverfahren präpariert werden und die Bildgebung für größere Proben ist auf *ex-vivo* Studien beschränkt. Die multispektrale optoakustische Bildgebung (MSOT) kann optische Absorption mit hoher räumlicher Auflösung mehrere Zentimeter tief im Gewebe messen, da sie auf dem optoakustischen Effekt, der Umwandlung von gepulstem Licht über optische Absorption in Ultraschallwellen, fußt. Auf Grund der starken Lichtstreuung ist die optoakustische Bildgebung von Haus aus eine volumetrische Bildgebungsmodalität und die Geometrie der Ultraschalldetektoren sollte darauf ausgelegt werden, 3D Daten zu erfassen. Im Verlauf dieser Arbeit werden drei verschiedene volumetrische Detektionsgeometrien vorgestellt, mit denen komplexe anatomische, molekulare und funktionale Bildinformationen auf mesoskopischer Skala gewonnen werden konnten.

Im ersten Teil wird ein optoakustisches Bildgebungssystem mit hochfrequentem Mehrkanalwandler mit linear angeordneten Elementen beschrieben, das der volumetrischen Bildgebung von kleinen, opaken Organismen dient. Die Systemgeometrie ist mit einem SPIM kombiniert, wobei das dünne, in der Fokalebene der Detektoren liegende Lichtblatt zur optischen Anregung benutzt wird und Volumendarstellungen durch Aneinanderfügen der einzelnen Schnittbilder erreicht werden. Die Verbindung beider Bildgebungsmodalitäten kann daher komplementäre Kontrastmechanismen ausnutzen und eignet sich für die Untersuchung biologischer Modelorgansimen (z.B. Zebrafisch oder Taufliege)

von den ersten bis hin zu fortgeschrittenen Entwicklungsstadien, in denen der Körper opak wird und Mikroskopietechniken keine zufriedenstellenden Ergebnisse mehr liefern können.

Der zweite Teil dieser Arbeit widmet sich der Modellierung und der messtechnischen Umsetzung zweier optoakustischer Eigenheiten: Zum einen resultiert die Anregung mit Laserpulsen im Nanosekundenbereich in breitbandigen Ultraschallwellen mit Frequenzen, deren Wellenlängen den verschiedenen Objektstrukturen entsprechen. Deshalb bestimmen die Eigenschaften der Ultraschallwandler, insbesondere die Mittenfrequenz und die relative Bandbreite, die Größenordnungen der Strukturen, die erfasst werden können. Zum anderen spielt die Auswahl der Messorte rund um die Probe eine entscheidende Rolle für die erzielbare Bildqualität und damit letztendlich für die Beantwortung biologischer Fragestellungen. Es wird eine zweite Systemgeometrie entwickelt, die auf einer homogenen optischen Signalanregung beruht und die diese beiden Aspekte besonderes berücksichtigt. Das System benutzt zwei unterschiedliche Mehrkanaldetektoren, die die Probe in einem neuartigen tomographischen Muster abrastern, um volumetrische Bilder von intakten, chemisch nicht vorbehandelten Proben aufzunehmen. Die Kombination aus multi-spektraler optoakustischer Mesoskopie und zwei sich ergänzenden Detektoren hat neue biologische Erkenntnisse im Bereich der Lokalisierung und zeitlichen Nachverfolgung von Nanopartikeln und Fluorophoren ermöglicht. Die Detektionsbandbreite des Systems reicht von 0,5 kHz bis hin zu 40 MHz und führt zu einer Auflösung von ca. $30\,\mu m$ in der betrachteten Ebene.

Im dritten Teil wird ein System vorgestellt, das zur *in-vivo* Bildgebung von Tumormodellen entwickelt wurde. Dieses System kann im Gegensatz zu bisherigen optoakustischen 3D Systemen, die nur im *ex-vivo* Modus arbeiten oder mit denen die Abbildung des gesamten Volumens zu aufwändig ist, auch intakte subkutane oder orthotope Tumormodelle *in-vivo* abbilden. Außerdem werden longitudinale Studien durch die Aufnahme ganzer Volumina erleichtert, weil dadurch die wiederholte, in 2D Systemen unvermeidbare Auswahl ein und derselben Schnittbildebene entfällt. Das vorgestellte System bietet die Möglichkeit intakte Tumore im lebenden Tier zu beobachten ohne dabei Tumorwachstum, -vaskularisierung oder das Wirtstier zu beeinflussen. Mit Hilfe des Systems können Volumina ganzer implantierter Tumore abgebildet und es kann eine annähernde isotrope Ortsauflösung von ca. $80\,\mu m$ in der gesamten mesoskopischen Probe erreicht werden. Diese Eigenschaften eröffnen eine ganze Reihe neuer Anwendungen auf den Gebieten der Krebsforschung, der Medikamentenentwicklung oder Therapieüberwachung.

Acknowledgment

First and foremost, I would like to thank Prof. Vasilis Ntziachristos for offering me the opportunity to be working with him in such an interesting and cutting edge field of research. I would like to thank him for giving me the first insights into optical imaging technologies and for planting the seed of further exploration in the field of biomedical imaging, for guiding, mentoring and supporting my ideas and efforts as a researcher.

I would like to thank Prof. Dr. Bjoern Menze and Prof. Dr. Bernhard Wolfrum for accepting to participate in the graduate committee and their approval of this thesis.

Several of the topics presented in this dissertation are presented in published papers, or are in preparation for submission. The reproduction of the materials (text, figures and tables) is performed with permission from respective journals, and clearly indicated through the body of this work, as well as appropriately cited in the reference section.

For guiding me through the first years of my PhD, I would like to thank Dr. Miguel Caballero, Dr. Andreas Bühler, Dr. Alexander Dima and especially Dr. Jérôme Gâteau. To Dr. Gâteau I am much obliged for him being a never depleting source of encouragement and support. His knowledge and scientific perspective have helped my initiation in the field as well as provided a continuous source of feedback and ideas. With great pleasure I remember the late nights at the lab and fruitful discussions on ultrasonic transducers and scanning geometries. His guidance, passion and friendship have tremendously influenced the outcome of my work, for which I am indebt. I would like to thank Prof. Amir Rosenthal and Prof. Daniel Razansky for extensive, positive and extremely helpful discussions on a broad range of scientific subjects related to the present work.

This work would have not been possible without help from external collaborators, which I would like to acknowledge: Dr. Annette Feuchtinger and Prof. Axel Walch for help and validation with *ex-vivo* imaging; Dr. Tobias Schmitt-Manderbach and Dr. Timo Mappes (Zeiss AG) for all their work and scientific contribution related to the first generation of the OA-SPIM setup presented in this work; to Dr. Neal Burton, Dr. Wouter Driessen, Josef Konradl from iThera Medical for their expertise and help related to my work.

I am grateful to Mr. Stratis Tzoumas and Mr. Panagiotis Symvoulidis for being never ending sources of support, good advice and amazing friendship.

Table of Contents

Chapter 1.

Introduction

1.1. Optoacoustic Imaging in the context of Medical Imaging

The ascent of imaging technologies over the last past decades has enabled medical and biological imaging to rise from imaging only anatomical information of the human body (X-Ray CT, MRI or Ultrasound), to visualizing and quantifying bodily function in terms of physiology and metabolism, up to sensing and following molecular activity at a cellular level in intact living organisms (MRI, PET, SPECT and Optical Imaging).

Medical imaging technology can be grouped from three different perspectives: based on the energy of the electromagnetic spectrum used to interrogate tissue (X-rays, Positrons, photons), based on the operating regime with regard to resolution and penetration depth (microscopic, mesoscopic or macroscopic), or based on the type of extracted information (anatomical, functional, cellular or molecular)[1] [2]. In anatomical imaging, the information extracted is concerned with the analysis of the structures inside the sample of interest, and can identify the general shape and anatomy of organs, bones and other tissues. Anatomical imaging can provide information regarding typical or structural malformations of the samples. In functional imaging, the objective is to quantify and measure changes of bodily functions like metabolism, chemical composition and blood flow, generally focusing on extracting physiological activities within a sample of interest. Molecular imaging, emerging as a technique imaging the fundamental molecular pathways inside living samples, is responsible for the detection of small changes at the cellular level. This is most of the times achieved using a variety of extrinsically administered probes with appropriate pharmacokinetics, aiming at enabling the visualization of the expression and activity of particular molecules, cells and biological processes and the influence to therapeutic action.

In the context of medical imaging, optical imaging techniques are convenient alternatives to other modalities, as they are highly sensitive, fast, easy and relatively inexpensive. In addition, optical imaging offers safe tissue interrogation by using non-ionizing radiation. Optical imaging relies on the physical effects generated by light interaction with tissue: absorption, scattering and light generation. Based on these three different events, particular contrast sources in biological tissue can be recorded, and can generate anatomical, functional and molecular information.

Optical imaging techniques are considered to be indispensable tools to most biological laboratories existent today. In particular, the most used available tools are the microscopy techniques, mostly due to the ability of high-resolution imaging of biological tissue with sub-micrometer resolution, but also due to limitations in the technological development of other modalities surpassing the restrictions imposed by optical imaging in bigger samples. Overall, the slow development of particular technologies enabling the study of big samples like entire animals, re-oriented the laboratory practice to smaller and implicitly generated a more cumbersome understanding of the entire function or anatomy of a living organism. Optical microscopy techniques, due to light scattering and absorption in tissue, offer limited interrogation of thin, or relatively transparent samples. As demands on imaging deeper structures in opaque tissue increased, alternative technologies emerged, enabling macroscopic scale optical imaging by means of Fluorescent Molecular Tomography (FMT) [3] and Diffuse optical tomography (DOT) [4]. However, these pure optical tomographic imaging methods are bound to a trade-off between penetration depth and spatial resolution: the resolution drops significantly to the millimeter range after only a few milliliters depth.

In recent years, due to increasing developments in the field of laser technology and ultrasonic detection, optoacoustic imaging (OA) emerged as a novel biomedical imaging technique. Through extensive efforts OA imaging offered the possibility to overcome several of the limitations imposed by traditional optical imaging. Optoacoustic imaging, by combining the advantages of two different imaging technologies namely optical imaging and ultrasonic detection, provides high-resolution optical imaging at penetration depths ranging from a few hundred micrometers to several centimeters in tissue, where classical optical methods for imaging through intact tissue samples or through entire animals have the drawback of reduced performance due to high photon scattering.

1.2. Optoacoustic: a hybrid imaging modality

Optoacoustic imaging, as a hybrid biomedical imaging modality relies on the detection of ultrasonic waves generated within tissue following the absorption of short laser pulses by optically absorbing structures. After tissue excitation and energy absorption in the tissue, broadband ultrasonic waves are generated due to the thermoelastic effect. The generated sound waves propagate outward of the tissue where they are recorded by acoustic detectors. The contrast in optoacoustic images is produced by structures absorbing energy, and the resulting pressure waves are directly proportional to the size of the absorbers. Therefore, ultrasonic resolution and optical contrast can be achieved. The ability to resolve optical contrast sources with ultrasonic resolution is a unique characteristic that enabled optoacoustic imaging to investigate structures ranging from microscopic to macroscopic sizes in high resolution with good temporal resolution.

These characteristics enabled optoacoustic imaging applications in a broad spectrum of interest, ranging from microscopy applications all the way to clinical translations. Optoacoustic microscopy, enabled functional visualizations of tissue beyond the penetration depth achieved by conventional optical imaging modalities like confocal microscopy or two-photon microscopy [5], while retaining microscopic resolution. Currently the implementation is widely adapted and combined with traditional microscopy techniques to extract different contrast information from the same sample [6]. On a pre-clinical stage, optoacoustic imaging enabled studies at the structural, functional and molecular level in *in-vivo* animals [7] [8]. Small animal optoacoustic imaging systems have been used in imaging cancer [9], cardiovascular activity [10] or neuroimaging processes [11]. The optoacoustic application in pre-clinical stage offers great promises for biological research as well as in the area of drug discovery and delivery. On a clinical stage level, the combination of a broad range of contrast sources with good imaging speed and high sensitivity would enable the translation of optoacoustic technology, offering great expectations in intra-vascular [12] and endoscopic [13] optoacoustic imaging devices, as well as breast imaging [14] hardware approaches.

1.3. Mesoscopic Imaging [1]

Powerful insights into biological phenomena can be gained by imaging at depths greater than the microscopic level ($<1\,\text{mm}$ depth), but smaller than the macroscopic scale ($>1\,\text{cm}$), termed throughout this work the mesoscopy scale [2]. The main rationale for this intent is to gain a more complete picture of bigger samples compared to the results provided by the microscopy techniques. *In-vivo* applications of mesoscopic imaging [16] have focused on developing insects, small animal embryos and extremities or implanted subcutaneous tumors. From an *ex-vivo* approach, anatomical and pathological information about tissue samples at mesoscopic scale is of relevance for a better understanding of physiological processes, or for treatment and/or surgical planning based on the analysis of sample biopsies. Currently the gold standard for extracting precise anatomical information from mesoscopic samples requires undergoing a labor intensive and destructive procedure of fixing the tissue followed by tedious systematic histological analysis [17]. Another commonly used approach imaging particularly the anatomy of the circulatory system of different excised organs creates corrosion casts, for example of the renal vascular system [18] or uses X-ray microtomographic imaging [19]. More recently, selective plane illumination microscopy (SPIM) [20] and optical projection tomography (OPT) [21] have been the method of choice for imaging samples in the mesoscopic regime without physical sectioning.

Optical projection tomography (OPT) and selective plane illumination microscopy (SPIM) techniques have been used to image small samples with microscopic resolution. Optical projection tomography attains a $20\,\mu\text{m}$ resolution for specimens with a thickness of up to 15 millimeters, but such performances rely on the chemical treatment of tissue with chemicals allowed to diffuse into tissue in order to offer tissue clearing from photon scattering and render the tissues transparent. Targeting anatomical and functional imaging, OPT has been used *ex-vivo* to obtain high-resolution 3D images of both fluorescent and non-fluorescent biological samples. So far several applications targeting anatomical and functional imaging using OPT have been presented; in [21] optical projection tomography is used for generating 3D images of embryonic structures after tissue-specific labeling by certain antibodies. The study showed an interesting insight on embryonic structures and on fluorescent labeled biological tissues in entire organisms, allowing a more complex analysis of mutant samples revealing abnormalities not previously accounted for by anatomy atlases. Accord-

---

[1]addapted from [15]

ingly OPT can be used in developmental biology and gene function studies for detecting aspects of mutant morphology like complex developing phases of the nervous system or rapid mapping of the tissue distribution of RNA and protein expression. More specific applications were introduced in [22], where by means of OPT a direct correlation between total islet β-cell volume and the onset of type-1 diabetes was established. *Ex-vivo* imaging of chemically treated adult mouse pancreata was performed upon specifically labeling the islet β-cell structures. Post-processing methods were used in order to segment and assess position, shape and size of the islets after a calibration step using confocal images of the same sample. The method is found to be convenient for quantitative studies being a promising approach for studying complex biological structures in entire organs at the expense of a complex and time-consuming procedure of optical clearing the tissue before imaging.

Selective plane illumination microscopy (SPIM) is a similar approach, which uses sheets of light to illuminate tissue, a strategy that generates fewer scattered photons in the volume compared to planar illumination, and can reach better resolutions ($6\,\mu m$) in weakly scattering tissues up to a thickness of several hundred micrometers deep. In [20] SPIM was used to image cleared excised organs and entire embryonic samples. This microscopy technique obtained cellular resolution throughout the entire fixed mouse brain and detected single GFP-labeled neurons in excised hippocampi. Moreover, three-dimensional images of dendritic trees and spines of populations of CA1 neurons are presented in isolated hippocampi. SPIM was also shown to enable visualization of the entire circulatory system including blood capillaries of whole mouse embryos and also the complete body, including muscles and the optic lobes, of a Drosophila melanogaster fly. In [23] SPIM is presented as a high-resolution imaging solution for acquiring fast dynamic changes in small sized living organisms. A transgenic line of fish embryo expressing GFP in somatic and smooth muscles as well as in the heart was used to showcase the abilities of SPIM to resolve all anatomical organs of the sample attaining a resolution of $6\,\mu m$ as deep as $500\,\mu m$ inside the animal. Longitudinal studies imaging the evolution of the embryo were carried out over a period of 3 days, without reported detrimental effects. The heart function and development were studied on the transgenic fish embryo and fast frame recording allows picturing the heartbeat. By means of selective plane microscopy, more opaque samples were investigated and a time-lapse imaging of embryogenesis of a fruit fly Drosophila melanogaster revels the ability to image different stages of development. Given the sub-cellular resolution SPIM attains, the method can be suitable for a wide range of organisms, ranging from small entire embryonic structures to single cells. Neverthe-

less, scattering compromises the performance of these methods as it blurs the photon trajectories and leads to resolution loss within a few tens of microns of photon propagation. A method that models the photon propagation to yield improved performance with imaging scattering organisms was also considered [16]. This technique showed improved imaging capacity to OPT when imaging the drosophila pupa which depending on the development stage may exhibit significant photon scattering. Ultimately however, this method is also affected by scattering and increasing specimen size effectively reducing the resolution achieved.

Optoacoustics offer a breakthrough in handling photon scattering in optical imaging. In contrast to optical resolution optoacoustic microscopy that is similarly affected by photon scattering, optoacoustic mesoscopy implemented with high frequency ultrasonic transducers operates with fully diffusive light. The resolution in this case obeys the ultrasound diffraction limits and is therefore insensitive to photon diffusion. Consequently high-resolution optical imaging can be achieved through penetration depths ranging from a few hundred micrometers to several millimeters. However, tissue acts as a high-pass filter of ultrasonic frequencies. Therefore the deeper the penetration the stronger the attenuation of high ultrasonic frequencies that are responsible for high-resolution imaging. This limitation defines also the limits of optoacoustic mesoscopy-since sub-100 micron resolutions for example can be only achieved at depths up to approx. 1-2 cm.

So far, optoacoustic imaging at single wavelength excitation has been widely studied and found to be useful in a broad range of applications at mesoscopic scale, among which tumor vascularization studies [24], mapping sentinel lymph nodes [25] or for detecting atherosclerotic plague [12]. By considering the possibility of successive light excitation at different wavelengths, multispectral optoacoustic tomography (MSOT) [26] was shown to enable the discrimination between sources of absorption having different spectral signatures. Multispectral optoacoustic imaging has been proven useful in particular for the detection of exogenous biomarkers [27] [28] or oxygen saturation levels.

So far, to our knowledge, truly volumetric multispectral optoacoustic imaging in the mesoscopic regime was not yet investigated in a configuration able to record a very broad range of frequencies. Independent studies with singular detector arrays were investigated, but were limited by the scanning geometry or by the hardware specifications. Throughout this work, the necessity of filling the gap between microscopy and macroscopy will be explored, and possible solutions provided by the current implementations will be proposed.

1.4. Why three-dimensional Optoacoustic Imaging

Due to light scattering in biological tissue and to the 3D propagation of the sound waves generated post-excitation in the tissue, optoacoustic imaging is intrinsically a 3D modality. Appropriate imaging systems recording the time-resolved pressure signals must be placed around the sample, so that the initial pressure distribution generated by optical absorption into tissue can be recorded. Additionally, from a visualization point of view, the third spatial dimension is a forever sought-after feature in medical imaging. By analyzing three dimensional datasets a more complete picture can be generated of anatomical, functional or even molecular information. This would allow a more confident conclusion to be extracted with respect to either volumetric malformations of major anatomical structures, dye distribution and circulation patterns during pharmakokinetics studies, or a better assessment and treatment of cancer tumors.

So far, three-dimensional (3D) optoacoustic imaging has mostly been implemented and used at macroscopic scale to image individual organs or the entire body of small animals [29, 30], and also moved towards clinical practice by focusing on breast imaging [14] or hand-held applications [31]. While on the macroscopic scale, multispectral optoacoustic imaging is already used to extract the molecular signature of several intrinsic and extrinsic contrast agents [32], in the mesoscopic scale regime, volumetric imaging combined with the ability to extract molecular and functional information from multispectrally acquired datasets has only been obtained with 2D imaging systems by stacking-up the cross-section images [26].

Currently, most optoacoustic pre-clinical systems use an array of detectors focused on a plane, in order to create cross-sections of the imaging sample. The data acquisition using an array of elements is fast, allowing real-time visualization of the 2D sections [33]. Another implementation used to record optoacoustic signals, employed a single focused element detector rotated around the sample [34, 35, 36]. In this implementation, the illumination is usually delivered from the top or the bottom part of the sample, while the transducer is rotated around the sample, describing a complete 360 degree detection. Depending on the transducer's specifications and the sample under investigation, appropriate transducers are selected and the scanning parameters are adjusted. These systems generate 2D cross-sections of the sample. In order to record 3D volumes, the detector interrogated a different cross-section by using linear stages to position the interrogation plane to a different level. By successive movements of the detectors and possibly of the illumination or of the sample, the 2D sections

are stacked, and 3D volumes are created. By stacking these cross-sections, the volumetric data-set has a rather poor resolution due to the physical limitations in the focusing properties of the array. Moreover, from a detection perspective, as light diffuses in the tissue the cross-sections are influenced by signals originating on regions outside of the plane of interest, degrading the quality of the cross-section.

1.5. Aim and motivation of this work

The goals of this work are four fold:

- Study, analyze, and exploit the benefits of using linear arrays in optoacoustic imaging.

- Perform an in-depth study on three different scanning geometries, concluding on the benefits and limitations of linear array implementations in optoacoustic imaging.

- Study and capitalize on the advantages of broadband recording of optoacoustic signals and their capabilities with regard to three-dimensional mesoscopic optoacoustic imaging.

- Apply an adjusted and optimal detection geometry to a given biological problem in order to gain novel insights from a biological perspective.

Chapter 2.

Theoretical and Technical Background

In the current section the underlining physical concepts responsible for optoacoustic image formation are summarized: from the initial conditions necessary for OA wave generation and the required hardware specifications, to wave propagation, characteristics of the detection hardware and post-processing steps required for image formation.

2.1. Optoacoustic Principles

2.1.1. The optoacoustic effect

Optoacoustic imaging, also termed photoacoustic imaging, relates to the effect of acoustic wave generation following transient light absorption. Optoacoustic imaging originates from the discovery of the photophone by Alexander Graham Bell in 1880 [37], but technological developments on lasers and ultrasonic sensing only enabled biomedical applications of the optoacoustic imaging in the early 21st century.

The optoacoustic (OA) effect correlates the generation of ultrasound waves in response to rapid heating of a tissue, generated by the optical absorption. A minimal OA system and the principle of OA wave generation are presented in *fig.* 2.1. The fundamental phenomenon underlining optoacoustic image formation can be summarized as follows: electromagnetic radiation delivered to an absorbing material will result in local heating, followed by thermal expansion and pressure wave generation. The generated sound waves will propagate outward of the material and ultrasonic detectors, placed outside of the tissue, will record these pressure waves. Due to variations of the acoustic impedance in different media and corresponding variation of the speed of sound (in air the
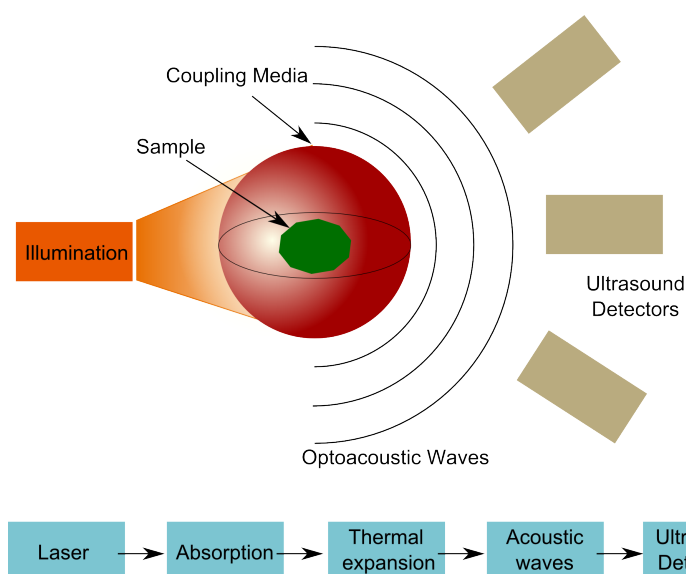
Figure 2.1.: A minimal optoacoustic setup and the optoacoustic wave generation: The sample is illuminated by a transient light intensity. Following absorption a local temperature rise will be observed and pressure waves will be generated after thermoelastic expansion of the tissue. Ultrasonic detectors are displaced around the sample to record the optical absorption into tissue.

speed of sound is approx. 331 m/s, while in tissue it can be approximated to 1540 m/s), a coupling medium is used to transmit the acoustic waves to the ultrasonic detectors. Following ultrasonic detection, the signals are recorded and digitized for further processing. Depending on the location of ultrasonic detectors around the absorbing material, tomographic reconstruction of a 2D image or a 3D volume can be done, where each value of a pixel/voxel will be related to the absorbed radiation inside the tissue.

2.1.2. OA Signal Generation

In the current section we review the mechanisms related to the generation of an ultrasonic wave following the optical excitation. Optoacoustic images are intrinsically an estimate of the distribution of the acoustic pressure that arises after the absorption of a pulse of light. The following equation are compiled and adapted from [38], [39] and from [40].

Considering a region with a distribution of absorbers termed μ_a, and a light pulse of duration t_p, then the distribution of absorbed optical energy, during

the pulse is defined by the heating function $H(r, t)$. The thermal energy per unit volume per unit time, converted by the radiation applied to the sample, at spatial position r and time t describes the energy change depending on the temperature variation, and we consider it of the form:

$$H(r, t) = \mu_a(r)\phi(r, t)\,, \tag{2.1}$$

where μ_a is the absorption coefficient and ϕ is the optical radiation fluence rate (i.e. the optical intensity per surface unit). The fluence depends on the incident light fluence on the tissue surface, and the light propagation up to the measuring position $\vec{r}$. It is thereby dependent on the optical absorption and scattering coefficients μ_a and μ_s of the medium. Assuming the duration of the laser pulse is short enough to ensure no changes in the density, then the resulting change of pressure caused by the increase of temperature, dependent on the optical properties and the local fluence can be defined by:

$$p_0(\vec{r}) = \Gamma\mu_a(\vec{r})\phi(\vec{r})\,, \tag{2.2}$$

where Γ is a dimensionless parameter relating the efficiency of the conversion of temperature to pressure, termed the Grüneisen parameter ($\Gamma = \frac{c^2\beta}{C_p}$, with c the speed of sound, β the isobaric volume expansion coefficient, and C_p the specific heat).

The relation between temperature increase and pressure generation states that for a temperature rise of one millikelvin the equivalent pressure rise level will be 8 mbar (=800 Pa)[41].

2.1.3. OA Wave propagation

Considering an initial induced pressure caused by the temperature increase, the acoustic wave equation for the $p(r, t)$ at position r and time t, initiated by this source, is termed the general optoacoustic equation and can be written as [39, 40]:

$$\left(\frac{\partial^2 p(\vec{r}, t)}{\partial t^2}\right) - c^2\nabla^2 p(\vec{r}, t) = \Gamma\frac{\partial H(\vec{r}, t)}{\partial t}\,, \tag{2.3}$$

where $p(r, t)$ is the acoustic pressure that can be measured using the ultrasonic detectors.

By considering the heating function $H(\vec{r, t}) = H_r(\vec{r}) \cdot H_t(t)$, with $H_r(\vec{r}) = \mu_a(\vec{r}) \cdot \phi(\vec{r})$ and $H_t(t)$ a Dirac-delta ($H_t(t) \approx \delta_t$), the propagation of the acoustic

waves in tissue media can be described in terms of a Green's function of the form:

$$G(\vec{r}, \vec{r'}, t) = \frac{\delta(t - \frac{|\vec{r} - \vec{r'}|}{c})}{4\pi|\vec{r} - \vec{r'}|} \, , \tag{2.4}$$

where Ω is the volume of the optoacoustic source composed of a multitude of points $\vec{r'}$. The solution to the wave equation (2.3) given by using a Green function [42] recorded at point $\vec{r}$ and time t after the excitation can be written on the form:

$$p(\vec{r}, t) = \frac{\Gamma}{4\pi c^2} \frac{\partial}{\partial t} \left[\int_\Omega H_r(\vec{r'}) \cdot \frac{\delta(t - \frac{|\vec{r} - \vec{r'}|}{c})}{|\vec{r} - \vec{r'}|} d\vec{r'} \right] \tag{2.5}$$

In the following work the ultrasonic transducers used to record the pressure waves were broadband detectors, with enhanced sensitivity around the central frequency. In *fig.* 2.2 **a** simulation of the theoretical optoacoustic signals generated by three absorbers with different radii are displayed. The simulation was performed by recording the OA signal generated as per the equation 2.5, and recorded by an ultrasonic transducer placed at 7.5 mm away from the sample. The distance corresponded to one of the detectors which was used during the current work. *Figure* 2.2 a shows signal shape in the time-domain, represented as an "N" shaped signal generated by the three absorbers with radii of 10, 20 and $50\,\mu$m. It can be observed that as a general characteristic, the signal amplitude is proportional to the absorber size(i.e. big absorbers will have a higher amplitude, as they absorb more energy). In *fig.* 2.2 **b**, the frequency spectrum of the three absorbers is presented. It can be seen that optoacoustic signals contain both low and high-frequencies. Moreover, the small absorbers will generate higher frequencies, while the big absorbers will generate signals with a lower frequency content. These observations lead to important considerations in optimal OA signal recording: small structures will generate high frequencies and will absorb less energy compared to bigger structures that will absorb more energy. The high-frequency signals generated from small structures will be more attenuated than bigger structures, and the attenuation follows an exponential law [43, 44]. In addition, as discussed in section 6.1.2, ultrasonic transducers operating at high-frequencies will need to compensate for the low signal-to-noise ratio of the small structures (=high-frequencies).
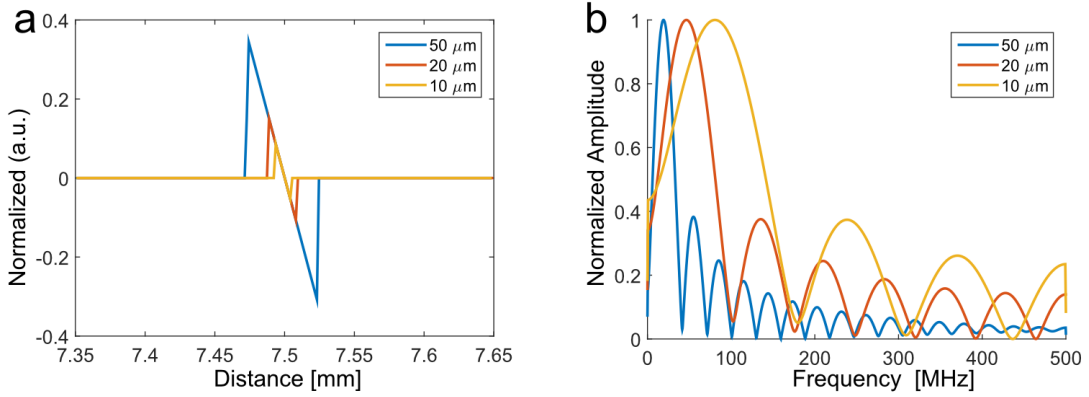
Figure 2.2.: Optoacoustic signal and frequency content. Optoacoustic signal generated from a sphere with different radii in (a) time domain and (b) in frequency domain

2.1.4. Directivity and limited-view detection

The generated OA signals can be reconstructed based on inversion formulas available for specific detection geometries. In standard environments, the detection and reconstruction algorithms for OA imaging can be grouped depending on the detection geometry: considering the 2D case, recording can be done along a line or a circle, or in 3D, along a sphere, a cylinder or a plane. In laboratory implementations though, the exact detection geometries specified by these exact inversion formulas, are difficult to be implemented because of spatial or hardware limitations. Generally, application and hardware dependent constrictions limit the ability to gather enough "views" of the object of interest. The consequences of partial-detection lead to a non-stable boundary detection problem, where sharp detailed points due to not having sufficient detection views will become blurred. Theoretically, the boundaries which cannot be efficiently detected can be identified in advance, and previous efforts have been done in studying the effects of limited view detection in OA imaging [45], in x-ray tomography[46] or in diffraction tomography [47]. Although previous studies performed an in-depth analysis of the directivity of OA signals in custom made experimental setups [48], in the present work we will briefly summarize the most common detection geometries together with the occurrences of limited-view detection.

Following energy deposition, absorption, and thermal expansion, the acoustic waves propagated from the objects need to be recorded. In *fig.* 2.3 a, the object and the waves propagating outwards are depicted in the context of a limited view detection geometry. Given a detection aperture covering an angle θ, it

can be seen that several acoustic wave emitting directions will not be recorded by this geometry, resulting in distortions and artifacts during the reconstruction step. The problem of reconstructing the acoustic absorption in objects which are not entirely "seen" by the detecting geometry has been studied in the context of sonar [49] and considered in previous studies involving OA imaging [50, 51, 45, 52, 53]. To summarize, for a stable reconstruction of a boundary located at a position $\vec{r}$, at least one of the two normal directions to the boundary at $\vec{r}$ must intersect the measurement surface. The schematic presented in *fig.* 2.3 **a**, depicts the normal directions to the absorbing surface of the object in the context of an incomplete detection aperture. The "visible" region, or the stable boundary, is depicted by the yellow line, while the red surface highlights the non-detectable region. In *fig.* 2.3 **b**, **c** and **d**, several typical detection geometries used in optoacoustic imaging are presented. In the case of the cylindrical view geometry (*fig.* 2.3 **b**, although from a detection perspective the sample is completely enclosed into a finite cylinder, the two objects (yellow) have boundaries which will not be accurately recorded by the detectors. For example, the object on the right side of the cylinder will have one normal direction (red-dotted line) not intersecting in any point the detection geometry. For the second object, the one on the left side of the cylinder, it can be seen that at least one of the normal (red-dotted line) directions intersects the detection geometry (we refer the interested reader to [50] for additional discussion on cylindrical configurations). By analyzing a circular geometry (or spherical in 3D), it can be seen that objects not inside the convex hull defined by the detection geometry will have edges not stably reconstructed. In *fig.* 2.3 **c**, the circular detection geometry is depicted, where detectors are placed along a circle around the sample. It can be seen that the two absorbers inside the circular surface will have their normals intersecting the detection geometry in at least one point. The objects placed outside of the detection geometry will emit waves which cannot be recorded by the current geometry, and as a consequence, the boundary information as well as the reconstruction stability will be inaccurate. The circular detection situation was further analyzed in [45], where the effects of a convex hull covering different apertures, generates a much more complex detection pattern for stable boundary detection. In the case of planar detection geometry, *fig.* 2.3 **d**, the detection plane is limited to a single side access around the sample, and therefore cannot record any wave generated parallel to the detection planes (red-dotted line parallel to the depicted detectors).

In order to better understand the effects of limited view and spatial directivity of the optoacoustic signals, in the following, results of different detection geometries simulating OA configurations are presented (*fig.* 2.4). The theoret-
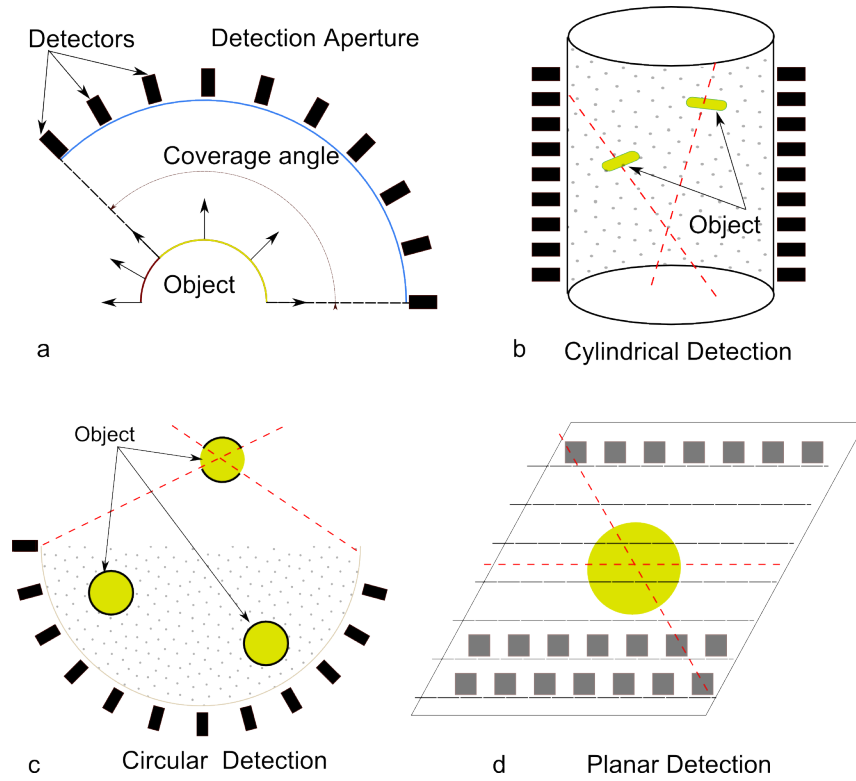
Figure 2.3.: Signal directivity in typical detection geometries. (**a**) Object and signal directivity with regard to the detection aperture; (**b**) Cylindrical geometry and directivity patterns of absorbing objects; (**c**) Circular Detection and (**d**) Planar detection;

ical image is presented in *fig.* 2.4 **h**: seven absorbers are positioned on a 2D plane, spaced by a $5\,\text{mm}$ distance. The signals were simulated as per equation 2.5. From a detection point of view, the simulation was performed by positioning a grid of detectors around the sample of interest. The simulation was performed in the context of isotropic absorbers and directional detection, but similar concept would apply for directive absorbers in the context of isotropic or directive detectors. In the current simulation, the positioning of the detectors was performed based on the detection geometry presented in section 5.2.1. For all simulations, the translation range covered a $20\,\text{mm}$ range, in steps of $0.75\,\text{µm}$. For simulating the linear translation of the detectors, the angular coverage was set to a single position (*fig.* 2.4 **a**). For all other simulations, the rotation angle was incremented from 15 to 360 degree (*fig.* 2.4 **b** - **g**). The home (0 degree) position of the detection geometry corresponds to the horizontal *x-axis* in the first circular quadrant. In *fig.* 2.4 **a** the covered detection area was limited to a

single angular position, and simulated a linear translation of the detector along a $20\,\mathrm{mm}$ range, in steps of $0.75\,\mathrm{\mu m}$. It can be seen that all seven absorbers have an elongated appearance along the translation axis (in this case the vertical axis) while the background appears to be polluted by noise originating from the reconstruction algorithm (see section 2.4). *Figures* 2.4 **b-g** show the simulation results by increasing the detection angle to 15, 30, 45, 90, 180 and 360 degrees. It can be seen that by increasing the angular detection aperture, the artifacts generated by the limited view effects are reduced. The absorbers spherical appearance is improved with the increase of detector positions, as more normal directions intersect the detection surface. In *fig.* 2.4 **l-r**, a magnified view of the top-left absorber is presented conditioned by increasing aperture detection. In the initial configuration, the absorber looks elongated, but it can be observed that by increasing the detection aperture, the accuracy of the reconstruction is increased due to more "views" of the detector on this particular structure. Moreover, as described in section 5.2.1, it can be observed that a 180 degree coverage provides an artifact-free reconstruction of the absorbers along the entire field of view, while reducing the background noise. Comparing the 180 degree detection with a full-view 360 degree coverage shows reduced levels of background noise, as well as a more homogeneous reconstruction of the absorber. By analyzing the entire plane of microspheres, it is visible that by doubling the detection coverage area, the results do not improve considerably, as a result of the full-view criterion fulfilled by the scanning geometry for in-plane structures. *Figure* 2.4 **j** presents a horizontal profile through the three absorbers of the lower-row (green arrow in *fig.* 2.4 **a**). It can be seen that by increasing the number of angles covering the simulated surface, the amplitude of the absorbers increases. A similar observation can be extracted from the vertical profile (red arrow in *fig.* 2.4 **g**).

2.2. Optical excitation

As optoacoustic imaging relies on delivering short pulses to absorbing material/tissue, in the current section, the general characteristics and requirements of optical parametric oscillator (OPO) lasers used during these studies are introduced.
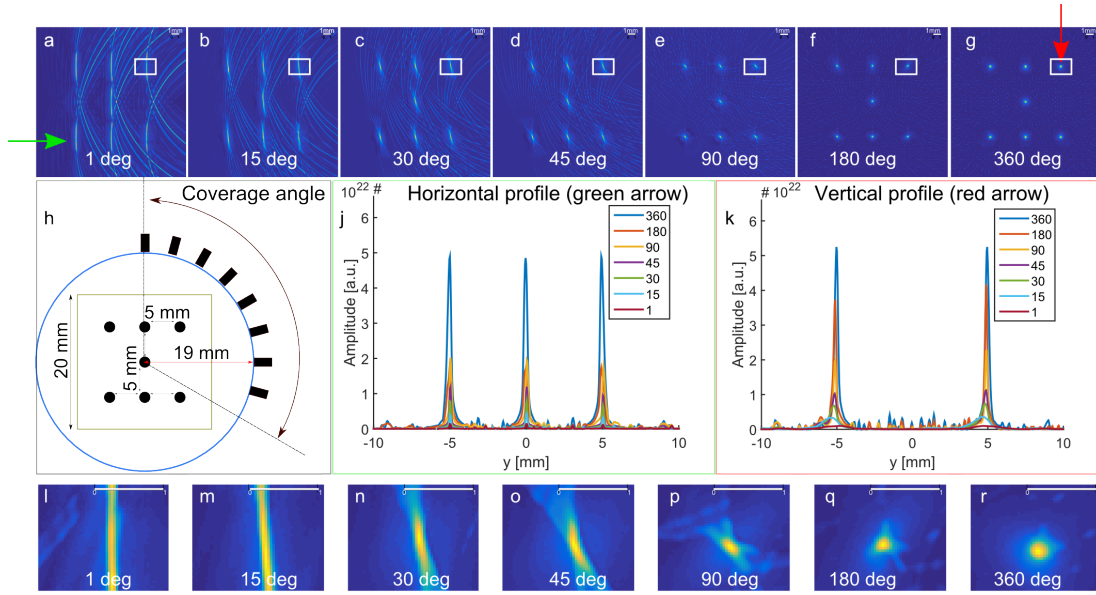
Figure 2.4.: Influence of detector position on reconstruction quality. Configuration simulation of angular detection coverage (**h**) and magnified insets: single angle (**a**) and (**l**), 15 degrees (**c**) and (**m**), 30 degrees (**c**) and (**n**), 45 degrees (**d**) and (**o**), 90 degrees (**e**) and (**p**), 180 degrees (**f**) and (**q**), 360 degrees (**g**) and (**r**). Vertical profile along a vertical (**k**) and horizontal (**j**) direction (see red (in **g**) and green (in (**a**) arrows).

2.2.1. Pulse duration for stress and thermal confinement

For generating optoacoustic signals, two conditions must be full-field with regard to the duration of the excitation pulses (τ): thermal and stress confinement. The **thermal confinement** dictates that the duration of a laser pulse, must be short enough such that thermal diffusion during the emitted excitation pulse can be ignored. The following equation dictates the thermal confinement

$$\tau_{th} = \frac{d_c^2}{\alpha_{th}},\qquad(2.6)$$

where α_{th} is the thermal diffusivity and d_c is the characteristic dimension of the heated region.

The second condition which must be fulfilled during OA signal generation is the **stress confinement**, and is defined as:

$$\tau_s = \frac{d_c}{c},\qquad(2.7)$$

where c is the speed of sound.

These two conditions apply the necessary limitations for optoacoustic image formation: if the laser pulse-width(τ) is much shorter than τ_{th} the excitation is considered to be in thermal confinement, meaning that the heat conduction during the excitation is negligible. Moreover, if the laser pulse-width is shorter than τ_s, the excitation is considered to be in stress confinement, meaning that the stress propagation inside the sample can be considered negligible. In current optoacoustic implementations, both these conditions must be fulfilled in order to achieve a good signal amplitude and high resolution

$$\tau < \frac{d_c}{c} < \frac{d_c^2}{\alpha_{th}}. \tag{2.8}$$

For example, in order to achieve the stress and thermal confinement, laser pulses must be shorter than $1\,\mu s$ to be used [54]. The meaning of the above, is also related to the theoretical achievable resolution, and holds that for a resolution of $150\,\mu m$ a laser with a τ_{th} pulse duration of $100\,ns$ would suffice. In practice, for the optoacoustic implementation presented throughout this thesis, the laser was operating at 10 Hz, delivering $10\,ns$ pulses duration, well bellow the imposed conditions.

2.2.2. Multispectral excitation

Optoacoustic imaging has been implemented so far using a broad range of frequencies of the electromagnetic spectrum: X-rays have been used to excite biological tissue with an embedded carbon rod absorber [55], while the radiofrequency and microwave spectrum has been used to record optoacoustic signals [56]. Most commonly, optoacoustic imaging relies on the visible and near-infrared range of the electromagnetic spectrum, because the contrast provided by absorption at these optical wavelengths is of biological interest. The latter region, the near-infrared range, is used due to an increased penetration depth of light in biological tissue, based on a reduced absorption of blood and water in this region.

In optoacoustic imaging, a single wavelength used for optical excitation of the tissue, will generate contrast originating from the absorbers in the tissue, and will render a so-called anatomical image of the sample. The main source of contrast in optoacoustic imaging is related to the photo-absorbing compounds present in the sample under investigation. These absorbing structures can be either intrinsic (contained by the native sample), or extrinsically administered.

The most absorbing structures in biological tissue are the two compounds of hemoglobin: oxygenated and deoxygenated together with melanin, lipids and water components. In the near-infrared window (from 650 to 950 nm), the particular excitation wavelengths used in this work for tissue excitation, the main absorbers are blood at the short wavelengths, and water and lipids at long wavelengths. When imaging an extrinsically injected agent, or a genetically expressed absorber [57, 27], the intrinsic components can influence the detection of the targets of interest. This is the reason why, ideal extrinsic contrast agents should exhibit a high molar extinction coefficient, and a low quantum yield [26]. From a technical point of view, the extrinsically administred contrast agents, as well as the ones genetically expressed must exhibit a sharp absorption peak in the excitation range, ideally in the NIR window for enhanced penetration depth. By performing multispectral excitation (*fig*. 2.5), the spectral signature of specific absorbers can be extracted after additional post-processing steps (see section 6.3.4). In order to perform multispectral excitation, the required protocol involves sequential excitation at different wavelengths in the case of tunable lasers, or the use of multiple lasers operating at different single wavelengths.
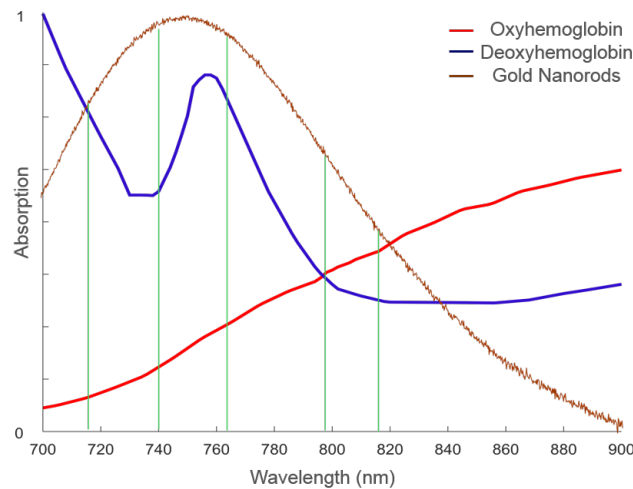
Figure 2.5.: Spectral signature of 3 absorbers: oxy- and deoxy - hemoglobin and Gold Nanorods. Vertical lines corresponding to possible excitation wavelengths.

The results presented in this thesis relied both on imaging the intrinsic as well as extrinsic signature of absorbers. Chapter *4* and *5* rely on the intrinsic absorption in order to extract anatomical images from biological samples, while chapters *6* and *7* show the possibility of detecting organic dyes and formulations of gold nanorods using the developed systems.

2.2.3. Excitation lasers

In the current studies, two different tunable lasers (optical parametric oscillator (OPO)) were used, both with a short pulse duration of under $10\,\text{ns}$:

- Optical parametric oscillator laser - Phocus II, Opotek Inc., Carlsbad, California, having a pulse width of $6\,\text{ns}$ and a repetition rate of 10 Hz. The laser was tunable in the $690 - 950$ nm range, and delivered a peak power of 70 mJ per pulse (at 760 nm)
- Optical parametric oscillator laser - Spitlight DPSS 250 ZHG-OPO, Innolas, Germany The Spitlight-DPSS 250 ZHG-OPO (Innolas, Germany) is a nanosecond optical parametric oscillator (OPO) laser. The laser generates 7 ns pulses with 15 mJ per pulse (at 473 nm), at a repetition rate of 50 Hz. The laser is tunable in the $418 - 710$ nm range.

2.3. Ultrasound signal detection

Ultrasonic detectors lie at the core position of an optoacoustic system, as they represent the modality of detecting the pressure signals after laser excitation of the tissue. The ultrasonic detectors are characterized based on several defining characteristics: central frequency, detecting material composition and shape. In the following, we will briefly introduce the main characteristics and specifications of ultrasound detectors, their fabrication technology and the main considerents limiting this technology.

2.3.1. Fabrication Technology

From a detection technology point of view, several methods can be involved in detecting ultrasound signals, and are presented in the following:

- Piezoelectricity is the ability of a particular material to transduce a mechanical pressure into an electric charge. It is the most common used form of detecting ultrasound signals, as a large variety of materials can be found in nature or can be easily manufactured. A major advantage of these detectors is that they can be produced in different sizes and shapes, ensuring flexibility in focusing capabilities or custom made detection geometries. The piezoelectric materials, either found in natural state or synthetically produced are based on crystals and can operate in both modes: as either generating an electrical voltage as a consequence to applied mechanical pressure or the other way around. This is termed transducer, and is the underlining effect in ultrasound

systems. In the case of optoacoustic imaging, the ultrasound detectors are used only in receive mode, where the ceramic element (piezoelectric transducer (PZT) in this work) records the acoustic waves generated in the energy absorbing sample.
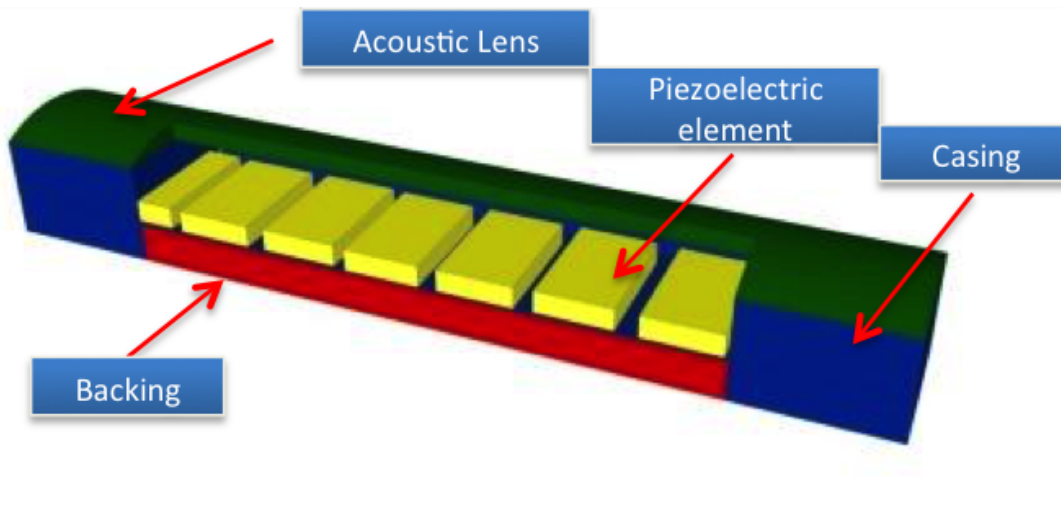
Figure 2.6.: PZT Linear focused transducer array - Building components (Adapted from [58])

The schematic of a generic ultrasound transducer is presented in *fig.* 2.6, where a series of single elements (yellow) are placed together in order to create a linear array. Generally, a transducer is composed of a piezoelectric material, the backing and the matching layer [59]. The backing layer, placed behind the detecting element, is used to dampen the resonance by reducing the ringing of the PZT crystal. The matching layer, placed on top of the detecting element, is used in order to enable the transmission. Particularly, the response of the array to the envisioned application, accounting for human, biological or the immersion medium in which the transducer will be operating must be considered when the transducer is designed. This is a necessary constrain to be imposed, as the acoustic impedance is different in different media. In the case of linear arrays, an acoustic lens is usually included, in order to improve the detecting capabilities of the array to sound waves originating in the vicinity of a plane.

• Capacitive micro-machined ultrasonic transducers(CMUT) are a new technology recently used for optoacoustic imaging [60] [61] due to a theoretically broader detection bandwidth, enhanced sensitivity and reduced noise levels.

CMUT arrays can easily integrate the electronics at the transducer level, minimizing the addition of noise on the recorded channels, providing a better image quality [62].

- Optical detection techniques, typically based on interferometry modalities have been used for recording the optoacoustic signals generated in biological tissue [63]. The Fabry-Perrot detection technique allows for a broadband recording of signals. Generally, optical detectors have the benefit of miniaturization without loosing sensitivity, and could be successfully used in applications requiring minimal invasive access (intravascular catheters or endoscopy). Moreover, the detectors can be rendered transparent to the excitation light, enabling backward-mode imaging capabilities. Optical interferometry comes at the expense of difficulties in parallelizing the acquisition procedure, as only one raster-scanning point by point acquisition is enabled.

2.3.2. Frequency

Frequencies used in medical ultrasound are in the range of 1-20 MHz, and appropriate detectors are usually selected for different applications. The center frequency of a transducer defines the resolution and the imaging depth: a low frequency (higher wavelength) transducer will have a lower resolution but a higher penetration depth, while a higher frequency (lower wavelength) transducer will provide increased resolution at the price of reduced penetration depth. Reduced penetration at high ultrasonic frequencies is due to the increased attenuation dependence with frequency.

In optoacoustic imaging as in ultrasound imaging, the same principles of resolution versus penetration depth hold. In currently existing pre-clinical systems, the ultrasonic detectors are usually operating at a center frequency ranging from $4\,\mathrm{MHz}$ - $10\,\mathrm{MHz}$, providing a theoretical axial resolution under $375\,\mathrm{\mu m}$ (the corresponding wavelength for a speed of sound in water of $1500\,\mathrm{m/s}$ and frequency at $4\,\mathrm{MHz}$ is related by the formula $\lambda = \frac{c}{f}$).

A special consideration must be directed towards the transducer's electrical response. The electrical impulse response(EIR) of a transducer describes the response of a detector to an excitation impulse. The EIR is dependent on the transducer's specifications being affected by the piezoelectric material used and the converting electronics (cable and electric impedance of recording electronics). The influence of the transducer's response on the recorded signal is equivalent to a band-pass filter with a center frequency around the resonant frequency of the detector. In order to correct the recorded signals for distortions

on the recorded amplitude and phase response, the transducer's response must be initially characterized. The characterization of the EIR of particular transducer arrays was an extensively analyzed topic, and the results and methods are available to the interested reader in [64] and in [65]. However, recording the EIR of a transducer is experimentally challenging, especially for high-frequency transducers [66].

2.3.3. Shape

In medical ultrasound transducers, the detectors usually used are grouped according to their shape and angle of acceptance of the element, into four categories: linear, curved, phased and annular arrays. A linear array is composed by a series of elements (usually between 64 and 512 elements) displaced on a flat surface, characterized by generating a rectangular imaging. The annular arrays are transducer arrays characterized by a spatial distribution of the elements in a concentrical manner, on the surface of the transducer.

In the current work the detection was achieved using two different linear arrays, both of them containing 128 elements densely packed along a line (see *fig.* 2.6 for details and table 2.1 for transducer specifications). A large aperture combined with market availability of probes with a broad range of frequencies (also over 20 MHz) were the main reasons for selecting linear arrays over other detecting geometries. The arrays have a small element size in one direction, allowing for a large angle of acceptance, while the focusing along the other direction allows for enhanced sensitivity and reduced distortion produced by sources positioned in the focal zone. The size of individual elements is always a trade-off between sensitivity, directivity and compact size: a big element size will enable a more sensitive detection of pressure waves to the detriment of a narrower directivity pattern, while a compact and small detecting element will ensure a convenient operation of the array with a large angle of acceptance to the detriment of a lower sensitivity.

An important factor to be accounted for in optoacoustic signal detection is the directivity of the detecting elements of the transducer array. Given a finite sized detecting element, it has been shown that the acoustic wave will arrive at the detecting element at different time points, causing an enlargement of the detected wave compared to the original, plus a lower amplitude compared to if it has summed coherently. This characteristic, together with the directivity of the elements are known as the spatial impulse response, and the interested reader is redirected to work presented in [64] and in [65].

Table 2.1.: Linear Transducer Arrays - Specifications

	Low-frequency	High-frequency
Center frequency of the transducer	6 MHz	24 MHz
Focal Distance	19 mm	7.5 mm
Element Width	300 μm	70 μm
Element Height	4 mm	1.5 mm
DAQ Specifications	40 MS/s	125 MS/s

2.3.4. Acoustic Focusing

Based on the focusing capabilities, the ultrasonic detectors used in optoacoustics can be grouped into three main categories: cylindrically focused, spherically focused and unfocused.

Spherically detectors, are focused on a line and are most commonly used on optoacoustic microscopy measurements, where the detector is raster scanned along the x and y dimensions, in order to record signals [5] [67].

Cylindrically focused detectors provide an enhanced sensitivity pattern along a plane, typically shaped as a thin slice. In the present work, all ultrasonic detectors, were cylindrically focused, in order to improve the sensitivity of detection along the z-plane. Cylindrically focused transducers have been used so far in optoacoustic implementations, where a single element was rotated around the sample, in order to define a circular surface and acquire a 2D cross section[68]. A similar detection geometry used an array of detectors placed around a circular surface in order to parallelize the acquisition procedure [33].

Unfocused detectors are sensitive to signals originating in front of the detecting surface, and in optoacoustic implementations are required to sample as dense as possible the entire detection area.

2.3.5. Data Acquisition Cards

Data acquisition cards were used to convert the measured signals in analog form, to a digital form that was then stored for further processing. We have used two different data custom built acquisition systems. The analog to digital converters (ADC or DAQ), are characterized by two different characteristics:

• Sampling rate: In order to correctly convert an analog signal, the Nyquist theorem states that the sampling rate must be at least double the highest

frequency recorded by the system. In the current implementations the two different DAQ, operated at 40 MSamples/s for the low-frequency linear array (maximum recorded frequency 12 MHz), and at 125 MSamples/s for the high-frequency array (maximum recorded frequency 40 MHz). Given the transducer specifications, the sampling rate ensured a good digitalization of the measured signals, by providing three times the minimal required sampling rate.

- Resolution: The digitalization resolution is usually expressed as a number of bits, encoding the capability of the hardware to detect the variation of the signal. The resolution of the current experimental setups were operating at a 12 bit level resolution over a 16 mV range.

The ADC's used in the systems presented in this thesis, allowed parallel simultaneous detection along all 128 elements. The recorded signals were transferred for later processing on the PC, via an Ethernet interface operating at 1 gigabit per second rates, and were custom build.

2.4. Image Reconstruction

In order to obtain a meaningful representation of the acquired optoacoustic signals the data must be reconstructed. Image reconstruction for optoacoustic imaging, resumes to the problem of solving the initial pressure distribution p_0 in the object, knowing the measured pressured $p(r, t)$ measured at time instant t, and sensor position r. The mathematical problem of image reconstruction has been an important topic of research over the past decade, and different implementations have been presented.

To reconstruct the internal source distribution (p_0) the solution is given by the universal back-projection formula [69]:

$$p_0(\vec{r}) = \int_{\Omega_0} \frac{d\Omega_0}{\Omega_0} \left[2p(\vec{r_0}, c \cdot t) - 2 \cdot c \cdot t \frac{\partial p(\vec{r_0}, c \cdot t)}{\partial (c \cdot t)} \right] \Bigg|_{t=\frac{|\vec{r}-\vec{r_0}|}{c}} \tag{2.9}$$

where Ω_0 is the solid angle subtended by the entire surface S_0 with respect to the reconstruction point $\vec{r}$ inside S_0, and

$$d\Omega_0 = \frac{dS_0}{|\vec{r} - \vec{r_0}|} \frac{n_0^s |\vec{r} - \vec{r_0}|}{|\vec{r} - \vec{r_0}|} \tag{2.10}$$
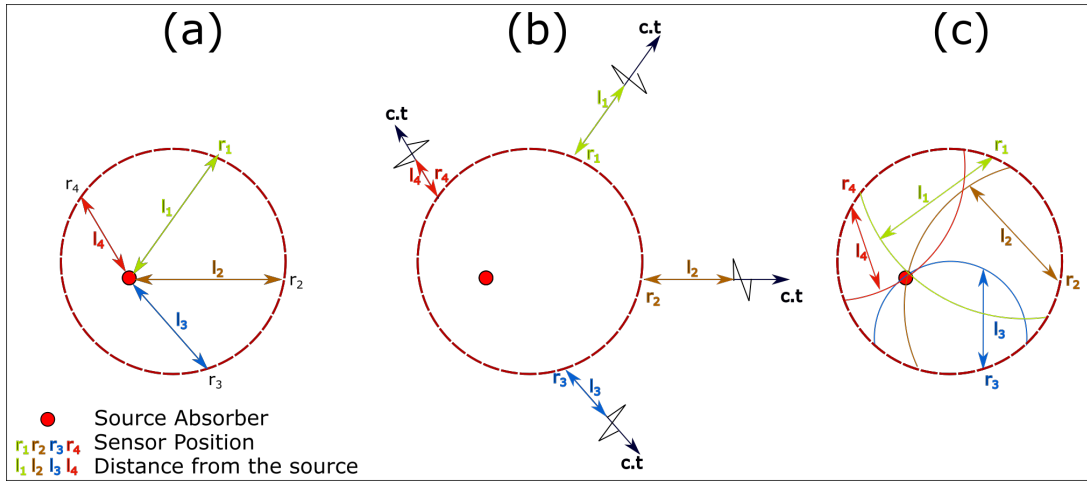
Figure 2.7.: Graphical representation of the backprojection algorithms. (**a**) The source point is detected at four different sensor positions ($r_1...4$) at distances ($l_1...4$). (**b**) The detected signals and their delays corresponding to the distance to the detector. (**c**) The signals are back-projected onto arcs with radius equal to the distance ($l_1...4$). Coherent summation of signals occurs only at the position of the initial abosrber [70].

The term $\frac{d\Omega_0}{\Omega_0}$ is a weighting factor for the contribution of each detection element dS_0, and it partially accounts for the directivity of the detectors. The back-projection method relies on essentially back-propagating the measured signals to a spherical surface (in 3D) or to an arc (in 2D). A more intuitive description of the backprojection algorithm is presented in *fig.* 2.7. In *fig.* 2.7 **a**, a source point (red absorber) is detected at four different sensor locations (r_1, r_2, r_3, r_4) at given locations (l_1, l_2, l_3, L_4) away. In *fig.* 2.7 **b**, the acoustic signals measured at the sensor position are presented including the delays proportional to the distances (l_1, l_2, l_3, l_4). The third step is to project the signals (*fig.* 2.7 **c**) to an arc (or a sphere in 3D) with a radius equal to the original distance (l_1, l_2, l_3, l_4). It can be seen that the position where the signals intersect corresponds to the unique position of the absorber source.

During the present work, the algorithm previously presented was slightly adjusted by removing the first term inside the squared brackets from equation 2.9, and only back-projecting the derivative of the pressure. The influence of the non-derivative term can be considered negligible, as the detection geometries operated on the far-field assumption [71, 70].

For particular modifications of the reconstruction algorithm used in specific configurations, we refer the reader to the chapters of interest: linear detection geometry - chapter *4*; cylindrical detection geometry - chapter *5* and *6*; conical -

chapter *7*.

2.5. Phantom & Animal Procedures

The work presented herein consists of experimental data acquired on three different types of samples: (1) synthetic phantoms which refer to samples containing controlled absorbers of known size and shape, custom arranged and positioned during the manufacturing procedure; (2) organs excised from laboratory mice; (3) *in-vivo* experiments performed on living mice. In the current, a description of the preparation and the protocols used during the experimental procedures is given.

- Synthetic phantoms preparation

  The supporting structures including the synthetic absorbers (phantoms) were created using 6 ml syringes, with a diameter of 12 mm. The supporting material was created using 1.6% w/m agar gel (Agar for microbiology, Fluka analytical). The agar gel was used as a supporting medium as it mimics the acoustic properties of soft tissues and is acoustically matched to the coupling medium used throughout the experimental procedures (water). For light scattering and homogeneous illumination of the samples, Intralipid-20% (Sigma) was added to the solution 0.8% v/v.

- Ex-vivo sample preparation - without contrast media

  The biological samples - i.e. the brain, or the kidney - were excised from CD1 adult mouse (Charles River Laboratories, Germany GmbH). The samples did not undergo any clearing or perfusion procedures. The samples were embedded in a 12 mm diameter cylinder of turbid agar gel (*fig.* 6.10 **a**). The gel was prepared by mixing 1.6% w/m agar gel (Agar for microbiology, Fluka analytical) with 0.8% v/v intralipid-20% (Sigma), and was used as supporting material for the tissue.

- Ex-vivo sample preparation - with injected media:

  All contrast agents were injected intravenously into the tail vein as aqueous solutions. The animal model used was CD1 mouse (Charles River Laboratories, Research Models and Services, Germany GmbH).

  IRDye 800CW: $20\,\mathrm{nmol}$ of IRDye 800CW(Li-Cor) diluted in a total volume of $100\,\mu\mathrm{L}$ saline solution were injected. The final blood concentration was approximately $100\,\mu\mathrm{mol}$.

Gold nanoparticles: an injection of $50\,\mu L$ conjugated gold nanoparticles, at a concentration of 6e10 particles/$1\,\mu L$ was administered.

All animals were sacrificed 15 minutes after the injection, allowing sufficient circulating time for the dye to reach the organs. Ten minutes after the animal euthanasia the kidneys were excised and embedded in a supporting turbid agar gel in a cylindrical mold (12 mm in diameter and 3.5 cm in height). The agar gel was made by mixing 1.6% w/m agar gel (Agar for microbiology, Fluka analytical) with 0.8% v/v Intralipid 20% (Sigma). All animals were treated in accordance with institutional and Bavarian government regulations in frame of the approved animal protocol.

- In-vivo sample preparation and handling

The in-vivo experiments, presented in chapter 7, were performed on mice bearing different breast tumor model carcinoma, implanted subcutaneous or orthotopically. The 4T1 tumor models ware implanted on adult female animals - athymic Nude-Foxn1 mice (Harlan, Germany). All imaging procedures were performed under anesthesia using 1.8% Isoflurane with 100% O2 and were approved by the Government of Upper Bavaria (animal protocol registration number: 55.2.1.54-2632-102-11). The cells were authenticated by the ACTT by several analysis tests: Post-Freeze viability, Morphology, Mycoplasma contamination, post freeze cell growth, interspecies determination; bacteria & fungal contamination. Additional mycoplasma contamination tests were also performed.

2.6. Validation Methods

Throughout the current work, three different validation modalities have been used: optical microscopy techniques, cryosection imaging and ultramicroscopy techniques. The broad variety of validation methods that has been used can be justified by the complementary contrast sources these modalities achieve. For example, optical microscopy techniques have been used to validate the presence of nano-particles, or during the H&E staining validation. The cryosection imaging was used to confirm the presence of fluorescent contrast agent in cross-sections, while the ultramicroscopy techniques were applied in order to gain a three-dimensional understanding of anatomical information.

Optical Microscopy

The slides containing $10\,\mu\mathrm{m}$ cryo-sections were first pre-fixed in 4% PFA (Santa Cruz Biotechnology Inc., Dallas, Texas, USA). Then, they were rinsed with distilled water and incubated 30 seconds with Haemotoxylin acide by Meyer (Carl Roth, Karlsruhe, Germany) to stain the cell nuclei. The slides were then rinsed in tap water again before incubation for 1 second in Eosin G (Carl Roth, Karlsruhe, Germany) to stain cellular cytoplasm. After rinsing in distilled water, the slides were dehydrated in 70%, 94% and 100% ethanol and incubated for 5 minutes in Xylene (Carl Roth, Karlsruhe, Germany) before being cover slipped with Rotimount (Carl Roth, Karlsruhe, Germany) cover media. Representative slides were observed using a Leica DM 2500 upright microscope, and pictures taken using a Leica EC3 color camera (Leica Microsystems, Wetzlar, Germany).

Gold nanorod localization was performed by means of darkfield microscopy. Selected representative fresh-frozen $12\,\mu\mathrm{m}$ thick slices through the kidneys were collected and imaged to confirm the distribution of gold nanorods. Darkfield microscopy was performed using a Leica DM 2500 upright microscope mounted with an oil darkfield condenser (NA=1.2-1.4) and with a 10x oil objective HC PL APO and an x40 HCX PL APO (Leica Microsystems, Wetzlar, Germany). Pictures were taken using a DFC 360FX color camera (Leica Microsystems, Wetzlar, Germany).

Cryosection Imaging
Validation of both anatomical information and molecular distribution was performed using a cryosectioning device [72]. After the optoacoustic experimental procedure, the sample was frozen to $-80°\mathrm{C}$ in order to preserve the tissue and chromophore distribution. The sample was sliced using a cross section step of $100\,\mu\mathrm{m}$ and for each slicing plane photographic images recording the color and fluorescence information were taken by using appropriate filters. Fluorescence excitation was performed using a filter at $740\,\mathrm{nm} \pm 40\,\mathrm{nm}$ on a white light and detection was done using a $785\,\mathrm{nm}$ long-pass emission filter.

Ultramicroscopy
3D Ultramicroscopy validation was performed using a commercial available device (LaVision BioTec, Bielfeld, Germany). For enhanced vessel visualization an injection i.v. of $2\,\mathrm{nmol}$ Lectin-InvivoTag750 (PerkinElmer, Rodgau, Germany) was performed 5 minutes before the animal was sacrificed and the sample (kidney or tumor) was excised. The sample was fixed in PaxGene (PreAnalytiX, Hilden Germany) as described in [73] and followed a chemical procedure of optical clearing according to [74]. After dehydration in a ascending ethanol series (3x 70%, 2x 80%, 1x 90%, 1x 95%, and 2x 100% for 30 minutes each, 100% over night) the sample was transferred in a clearing solution of dimethylether (Sigma Aldrich) for 3 days at $4°$. The cleared specimen was scanned using a

x0.63 magnification with a x2 objective lens (MVPLAPO 2x, Olympus, Hamburg, Germany), achieving an in-plane resolution of $5.1\,\mu m$, and $4\,\mu m$ along the vertical dimension. In order to visualize the specific lectin-InvivoTag750 signals a filter-set with excitation range $740/35$ and emission range $795/50$ was used.

Chapter 3.

Tomographic geometries for three dimensional optoacoustic imaging

The current section will provide an overview of optoacoustic imaging systems employed in generating three dimensional information. In the present section, a general overview of the optoacoustic systems is presented followed by a more specialized description of systems using linear arrays. As the main work presented in this dissertation is based on using linear arrays, a sub-section including the limitations of current geometries will be presented. The current chapter is separated from the previous section by presenting the advantages and limitations of OA systems from a hardware and detection geometry point of view. The chapter is meant to orient the reader in the context of state-of-the-art 3D OA systems, while enabling a better understanding and motivation for the work developed in the current context.

3.1. Scanning configurations in optoacoustic imaging

In this section, a review of the state-of-the-art optoacoustic systems will be given in order to present the prior art and place the presented geometry in the context of optoacoustic imaging system design. Given the direction of the current work, the classification will be performed based on the detection geometry used to record the signals. This is by no means an exhaustive review of all existing optoacoustic systems, but rather a short summary of systems, presented to summarize the major categories of implementations.

Different tomographic scanner configurations have been proposed to capture the broadband ultrasound field generated by the excited volume. These configurations mostly differ by the tomographic geometry employed, and the spatiotemporal characteristics of the ultrasound detectors [75], which both influence the image quality in terms of resolution and spatial fidelity. A large solid an-

gular coverage, together with a large field of view, is generally sought after to ensure achieving high resolution over the entire sample. Scanners are usually designed for a specific application, accounting for the size of the sample. Because the center frequency and limited bandwidth of a specific detector define the size and shape of structures it is able to detect (section 2.3), careful considerations must be taken into account when designing such a system. The three most common detection geometry used in optoacoustic imaging are summarized in *fig.* 3.1.
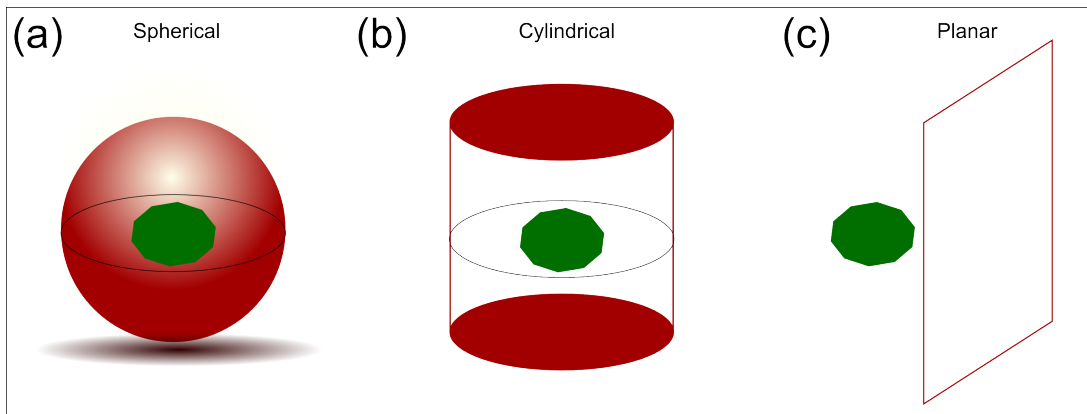
Figure 3.1.: The three most common detection geometries used in optoacoustic imaging; (**a**) Spherical (**b**) Cylindrical (**c**) Planar. The implementations can be performed by using single detectors, or with arrays of detectors (approached in this work). green shape - absorbing object

The spherical detection surface (*fig.* 3.1 **a**) describes a detection geometry completely encompassing the sample under investigation. It can provide nearly isotropic resolution and is therefore considered the ideal choice for optimal image quality in optoacoustic tomography. In [76] and [77], a detection geometry placing detectors on a spherical pattern is presented. The modality is using a custom made 128 elements placed on a semi-spherical structure, actuated by a rotation stage, moving the detecting element in order to increase the sampling positions. A similar detection geometry is described in [29], where an arc-shaped 64 element transducer array is rotated around the object, describing a spherical detection geometry. The illumination is provided orthogonally to the array using a two-arm fiber bundle delivering pulses of laser light. The system attains a theoretical resolution of $500\,\mu\mathrm{m}$, and is able to record biological information from individual organs and blood vessels in the entire body of a mouse. Another approach, also a spherical detection geometry, [78] has showed

good resolution at penetration depths of up to $1.5\,\mathrm{cm}$ in living tissue, by using a 256 elements cup-like placed on a spherical surface, and illumination originating at the bottom extremity of the hemisphere. However, for this last system, the sample is not fully enclosed in the detection surface, which leads to limited view artifacts.

In the cylindrical implementation (*fig.* 3.1 **b**), a detection surface mimicking a confined cylinder is used to record the acoustic signals. Initial OA implementations to create 2D cross-sections of biological tissue used a single, cylindrically focused transducer rotating around the sample to acquire signals [8]. A similar configuration used a cylindrical transducer to record signals from a rotating sample, in order to create 2D cross-sections [68]. In both these approaches, the thickness of the acquired cross section depends on the focusing properties of the detector used, and can severely influence the quality of the images, by including out-of-plane signals in the plane of interest. Improving the illumination patter by reducing it to a thin plane of light has showed to create OA images at mesosopic scale [79]. These initial implementations were capable of volumetric imaging, by translating the sample, or the detector array, along a z-plane and repeating the acquisition procedure. These initial approaches were further developed, by parallelizing the acquisition procedure with the addition of several other detection elements [33, 80, 81].

In the planar detection mode (*fig.* 3.1 **c**), the detector is scanned over a flat surface in order to produce images of the sample. One implementation introduced in [82] uses a spherically focused transducer to detect the OA signals generated by an absorbing sample, by scanning the transducer along the x and y dimensions. This raster-scanning detection modality [83] [25] was implemented with a high-frequency single element transducer, recording a broad range of frequencies in mesoscopic samples [67]. Other planar geometries, made use of linear arrays translated along a single dimension, in order to obtain volumetric datasets [84, 85, 86, 87, 88, 89]. Due to an increased number of detectors, this modality parallelizes the acquisition of OA signals. The parallel acquisition of OA signals reduces the acquisition time, enabling thus a convenient time frame for multispectral acquisitions. Alternatively to piezoelectric detectors, optoacoustic signals have been recorded using a Fabry-Perot interferometer [63], where an interrogating laser beam is raster scanned on the surface of a planar transparent sensor in order to detect the pressure waves.

MSOT 256 Optoacoustic System

In the current work a commercially available optoacoustic system was used for a comparison experiment, so a short schematic and the characteristics will be presented in the following.
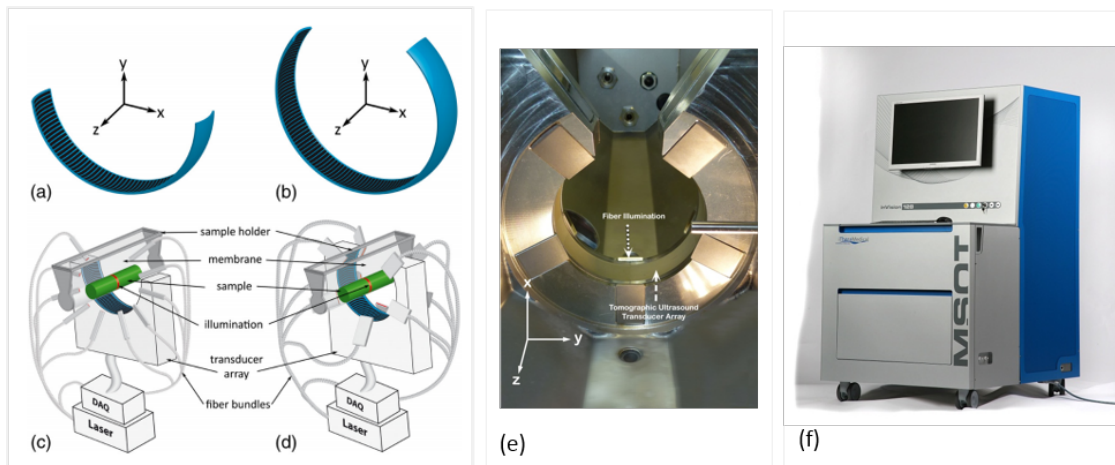
Figure 3.2.: MSOT 256 System (reproduced from [90]): (**a**) and (**c**) MSOT 64 system, (**b**) and (**d**) MSOT 256 system; (**e**) Photograph of the MSOT 256 chamber, presenting the curved array and the illumination fibers; (**f**) Photograph of the MSOT 256 cart;

Figure 3.2 presents the concept of the MSOT 64 and the newer MSOT 256 systems (iThera Medical GmbH, Germany). The optoacoustic implementation using a curved array with 64 elements is presented in *fig.* 3.2 **a** and **c**. The elements are positioned along the curved array, spanning 172 angular degrees [91]. Sample illumination is achieved using fiber bundles positioned around the array to create a uniform illumination ring of approx. 7 mm width, oriented in the focal plane of the transducer. An updated implementation is presented in *fig.* 3.2 **b** and **d**, where the number of elements has been increased to 256 and the angular coverage was spanning 270 degrees [92]. The center component of both these systems was the custom made cylindrically focused curved array with center frequency at 5 MHz, and covering a sensitivity band of up to 7.5 MHz. In both systems, the samples are submerged in a water tank positioned horizontally. Before submersion, living samples are wrapped in thin polyethylene membrane to protect the animal, and anesthesia and oxygen supplies are provided through a breathing mask. The systems produce cross-section 2D images, by translating the sample through the focal plane of the transducer.

3.2. Linear arrays in optoacoustic imaging: Prior art

From a technological development point of view, optoacoustic imaging relies on technical advances provided by two different fields: on one hand, optical

excitation is dependent on the specifications of the lasers, while acoustic detection is strictly connected to developments on the ultrasound sensing field. As piezoelectric detectors are commonly used in ultrasound imaging, and particularly linear arrays, in the present work we will show the benefits of adapting this readily available technology to the field of optoacoustics.

Previously, ultrasonic linear arrays have had limited use as detectors for optoacoustic imaging. Due to recent advances in data-acquisition system design together with a better understanding of their acquisition capabilities the situation has started to change. Linear ultrasonic arrays are convenient, cheap, and a readily available technology. By combining them with custom built data-acquisition systems, parallel acquisition can be performed, considerably reducing the acquisition time compared to single element detectors. Moreover, the custom built implementations can accommodate for particular requirements depending on the envisioned application, like bigger probes with bigger elements and increased sensitivity, or smaller arrays with higher central frequency, smaller elements and increased detection acceptance angle.

Several custom made configurations as well as commercially available arrays were used in different scanning geometries in order to record optoacoustic signals. In [82], a linear array with a centre frequency of 30 MHz, mounted on a linear stage, was translated over the sample in order to image subcutaneous vasculature in rats, and also dye accumulation and clearance in the sentinel lymph node (2008). The same transducer was used in order to visualize the irregular beating heart of a mouse [88], or the pulsatile motion of the human vasculature[93]. In [94], a standard 128 channel ultrasonic linear array probe acquiring in real-time at 10 Hz, centered at 5 MHz, was used to identify the vasculature in the human arm, by linearly translating the array along a single dimension. This system integrates the illumination next to the ultrasonic detector's casing, creating a broad illumination pattern around the focal plane of the transducer. A similar approach was presented in [95] where a linear translation of a linear array with a center frequency of 7.5 MHz was used to acquire optoacoustic images of the human finger, arm and leg.

Other acquisition modalities using linear arrays involved a rotation of the sample or of the transducer in order to perform tomographic acquisitions at a cross-section level (2D). We refer to these geometries as cylindrical implementations, as the displacement of detecting elements around the sample forms a cylinder. In [30] a 128 element linear array with a central frequency of 5 MHz was used to record optoacoustic signals from biological samples. The focal plane of the linear array was placed perpendicular to the vertical axis, corresponding to the axis of rotation. The sample was rotated using a stepper mo-

tor, while the linear array was stationary. The system recorded cross-sections of *ex-vivo* mouse samples. By rotating the transducer around the head area of a mouse, and delivering illumination from the top, in [96] a 128 element linear transducer array used to detect optoacoustic signals from an intact mouse brain.

3.3. Understanding the capabilities of linear arrays

The experimental procedures performed in this work used two different 128-element cylindrically focused linear array transducers, which are presented in *fig.* 3.3, and are characterized by the three axis of resolution (*fig.* 3.3).
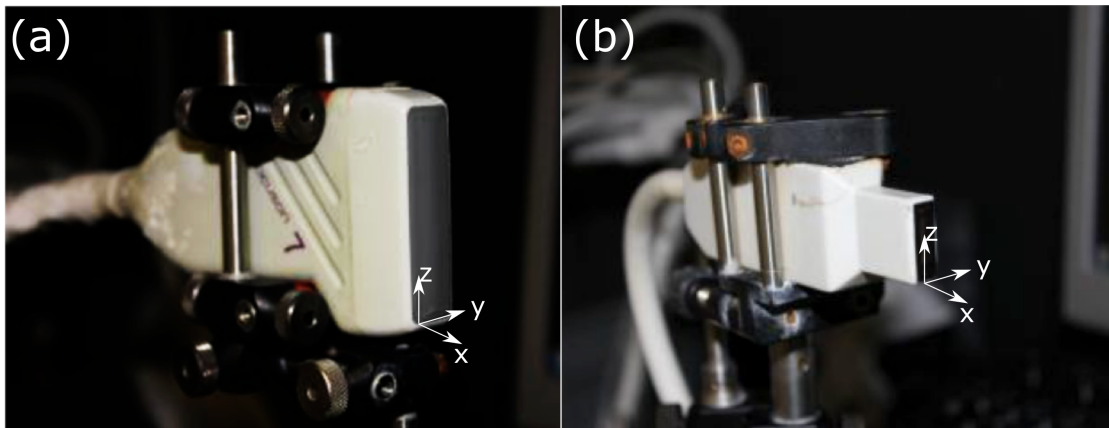
Figure 3.3.: Photograph of the linear transducer arrays (128 elements); (**a**) Low Frequency Siemens L7 probe and (**b**) Vermon 24 MHz Transducer

1. Low-frequency: 6 MHz center frequency, 300 μm inter-element pitch, 4 mm element height, 19 mm focal distance, Acuson L7, Siemens Healthcare)

2. High-frequency - 24 MHz center frequency, average pulse-echo −6 db bandwidth of 60%, 70 μm inter-element pitch, 1.5 mm element height, 7.5 mm focal distance, Vermon

Figure 3.4 **a**, provides a schematic of the resolution components characterizing a cylindrical element, and governing the behavior of cylindrically focused linear arrays. From a resolution point of view, the linear arrays are characterized by three components, the so-called: axial, lateral and elevation resolution. In the current section a general discussion on the abilities of ultrasonic detectors with regard to resolution is provided.

Figure 3.4.: Resolution components of focused linear array; (**a**) Resolution terminology for a single element (**b**) Sensitivity field of a single element in the lateral and (**c**) elevation dimension

The axial resolution provided by an ultrasonic transducer depends on the duration of the recorded OA signal pulse duration, and is defined as the minimum distance for which two absorbing structures located along the path of the ultrasound beam (perpendicular to the array) can be discriminated. The spatial pulse length (SPL) is defined as the product between the pulse duration and the speed of sound. For a high-frequency transducer the spatial pulse length will be short, while for a low-frequency transducer the SPL will be long.

The axial resolution is defined as [97]

$$\delta_x = 0.88\lambda_c \,, \tag{3.1}$$

where λ_c is the wavelength corresponding to the low-pass cutoff frequency of the array.

The lateral resolution is defined as the minimum distance that can be differentiated between two absorbing structures situated along the linear array (z-axis). An increased lateral resolution corresponds to a reduced width of the ultrasound beam. The lateral resolution is dependent on the distance to the transducer array and the aperture of the array along the z dimension. Since the characteristics of the array's detection spot having maximum sensitivity are considered important during the current implementations, the general sizes of this area will be given.

In the case of the lateral dimension, the width of the element defines the

properties relating the angle of acceptance with regard to the width (dimension along z) (w) of the sensor: let α be the angle of acceptance and λ corresponding to the frequency characteristic of the transducer, the angle of acceptance will be: $sin(\alpha/2) = 0.514\lambda/w$. This characteristic will ensure that for a transducer with a width of the element ranging between $\lambda/2$ and $\lambda/3$ the sensitivity field will have a short near field range, followed by a large divergence. By considering a linear array, the stack of elements will ensure a large angle of acceptance on the entire aperture of the probe, by enabling a large overlapping zone of the sensitivity patterns of neighboring elements. The sensitivity field of a single element can be seen in *fig.* 3.4 **b**. In conclusion, the lateral resolution of a linear array depends on the lateral aperture of the probe, as well as on the detection geometry used.

Additionally, the center frequency and geometrical specifications of the transducer define the spot providing the maximum sensitivity for detection. The characterization for a focused linear array could be split into two particular properties: on one hand the lateral dimension, describing the behavior along the *xz* plane (*fig.* 3.4 **b**), while on the other hand the elevation dimension, characterizing the transducer along the *xy* plane (*fig.* 3.4 c).
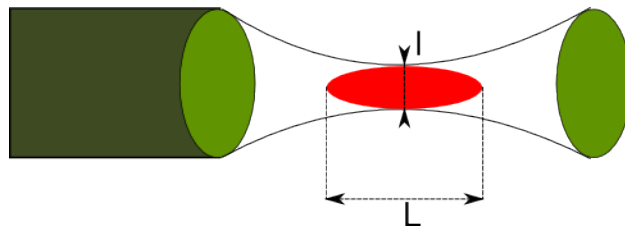
Figure 3.5.: Sensitivity area specifications for focused transducers.

The elevation resolution (along the y-axis) provided by a linear array is dependent on the focusing capabilities of the detector:

$$\delta_y = \lambda_c F_\# \,, \tag{3.2}$$

where $F_\# = \frac{F}{D}$, with F the focal distance of the detector and D the height of the active element. In the case of linear array's used the $F_\#$ was 4.75 for the low-frequency array (6 MHz) and 5 for the high-frequency transducer (24 MHz), resulting in a narrow aperture and a deteriorated elevation resolution.

In the case of the elevation dimension, the properties of the acoustic lens as well as the diameter of the detecting element, define the characteristics of the sensitivity along this dimension. *Figure* 3.5 presents a visual representation of

the sensitivity field properties along the elevation dimension (*fig.* 3.4 **c**). The first value characterizing the sensitivity pattern of a focused element along the yx is the length of the focal spot, termed here l:

$$l \approx \lambda \frac{F}{D} \tag{3.3}$$

The second property characterizes the width of the focal spot:

$$L = 7\lambda(\frac{F}{D})^2 \tag{3.4}$$

As previously mentioned (section 2.3), the presence of the acoustic lens, provides enhanced sensitivity for a region with a length L and diameter l. For example, for a transducer having a focal length of 7.5 mm, an element height of $1.5\,\text{mm}$, the length of the focal area will be $L = 7 * (1500/24) * (7.5/1.5)^2 \approx 1cm$ and the width $l = (1500/24) * (7.5/1.5) = 312.5\,\mu\text{m}$.

3.4. Limitations of current geometries

Although using linear arrays in optoacoustic imaging has several advantages, careful considerations must be taken in by-passing the limitations of this technology. Using linear arrays in optoacoustic systems comes with drawbacks regarding limited-view problems (exemplified in section 2.1.4), as well as issues concerning detection of certain absorbers which are strongly interconnected with the position and the orientation of the probe. In [98] the impact of structural orientation in 3D optoacoustic imaging using linear arrays was studied. It was shown that the anisotropic emission of elongated structures can only be recorded from certain positions and orientations of the transducer array and it can have important implications in the overall image quality since the 3D reconstructions will render inaccurate reconstructions. In [99] and in [100], an approach of integrating planar acoustic reflectors is presented in order to mitigate the effects of limited view detection. The method was applied on synthetic data, the skeleton of a leaf, as well as on excised mouse ear. Although the method showed improved detection without performing any scanning of the linear array, it requires 360 degree coverage around the scanned object, and does not account for any attenuation of the acoustic wave during the reflection process.

In addition to the sensitivity of the detection with regard to complex structure orientation, the linear arrays provide an elevation resolution one order of

magnitude worse than the axial resolution. This includes additional burden on reading and interpreting the optoacoustic datasets, as most 3D datasets results in in-homogeneous resolution. The previously presented systems employing a linear translation of the probe in order to acquire 3D data-sets are considerably limited in terms of homogeneous resolution improvements. Although previously implemented solutions rotated the array around the sample of interest in order to compensate for the limited view artifacts, they did not solve the problems of resolution homogeneity. By only rotating the array around the sample, enhanced sensitivity of the probe around the focal area hindered the possibility of obtaining homogeneous resolution datasets. In [101], the proposed scanning geometry performed a linear translation of the probe over the sample, followed by sample rotation (along the x-axis, *fig.* 3.3) and repetition of the translation. At the expense of long scanning time and single sided access the results show improvements in the reconstruction quality. Although the method accounts for the geometrical properties of linear arrays in a much better way compared to previous methods, it does not grant access around the sample, possibly introducing limited-view artifacts and hindering the ability to record volumetric information from multiple projections.

The following work presents three different systems overcoming the limitations of earlier OA imaging methods using linear arrays. In chapter 4, a linear translation geometry is presented for 3D imaging of mesoscopic scale samples. Compared to previously presented methods using a planar detection geometry, and particularly linear arrays translated over the surface of the sample, in the current geometry, the limitations in resolution degradation along the elevation dimension of the array are overcome. This is achieved by operating in a confined area of the excitation region, by using a thin plane of illumination oriented confocally to the elevation plane of the transducer. This approach, although providing only single-sided access to the sample, provides 3D datasets with homogeneous resolution along all three dimensions from small samples like zebrafish. In order to increase the field of view and accommodate entire samples sized up to 1 cm, in chapter 5, a scanning geometry recording volumetric optoacoustic datasets is presented. The scanning modality accounts for the geometrical properties of the detector, and in addition to a rotation of the detector, a translation of the focal zone over the sample is performed. This enables homogeneous in-plane resolution and a big acceptance angle, encompassing entire biological samples. In chapter 6, mesoscopic imaging is performed in a volumetric fashion, using multispectral acquisitions, in order to record the complex distribution patterns of injected dyes in entire, intact biological samples. Moreover, an in-depth study of frequency impact in OA recording on biological

information is extracted. In chapter 7, based on the previously derived capabilities of the system, an *in-vivo* adaptation of the geometry is presented. The presented method provides homogeneous resolution along all three dimensions, in the context of pure 3D recordings in a multispectral context. *In-vivo* 3D vasculature and bio-distribution of injected contrast agents is presented, enabled by resolution capabilities of $\approx 70\,\mathrm{\mu m}$, a sought-after tool for current biological studies explaining tumor growth, treatment monitoring or agent bio-distribution.

Chapter 4.

Hybrid imaging of adult zebrafish using combined SPIM & OA

The experimental setup and the results presented herein are the result of collaborative work. The author's contribution is mainly on the optoacoustic development of the hybrid setup. For these reasons, the focus on the following chapter will fall on the optoacoustic part, while the SPIM part is only presented briefly, to create a complete picture of the envisioned application and utility of the system.

In the current section, the first scanning geometry implemented in the context of this dissertation work is presented. The optoacoustic implementation used a linear transducer array, scanned in a linear translation fashion (see *fig.* 2.3 **d** for clarification). First, the motivation for such a device will be described, followed by a description of the individual components forming the hybrid system. A characterization of the optoacoustic system will be presented, and finally a conceptual study presenting combined results from both these modalities will demonstrate the system's ability.

Some of the materials of this chapter are also presented (at places with minimal or no changes) in the publication entitled:

- *"Selective plane illumination optical and optoacoustic microscopy for postembryonic imaging"* by Hsiao-Chun Amy Lin[*], Andrei Chekkoury[*], Murad Omar[*], Tobias Schmitt-Manderbach, Benno Koberstein-Schwarz, Timo Mappes, Hernán López-Schier, Daniel Razansky and Vasilis Ntziachristos, published in Laser & Photonics Reviews (September 2015) [102].

---

[*] equal contribution

4.1. Motivation

Scanning geometries in optoacoustic imaging play a crucial role on imaging quality and on the applications enabled by a certain system. A summary of previously available optoacoustic systems and the detection geometry employed was described in section 3.1. In the current work, a single sided detection geometry, operating on a pseudo-linear translation of the array is introduced (the array is static and aligned confocal to the illumination plane, while the sample is linearly translated through the illumination plane during the acquisition procedure). The geometry is implemented on a new illumination pattern, novel to the linear detection systems. The advantages and limitations of the method as well as a comparison with previous implementations are discussed in the conclusion section of this chapter.

Selective plane illumination microscopy (SPIM) and other similar fluorescent microscopy techniques using a focused sheet of light to illuminate the sample of interest are ideal imaging modalities investigating small, transparent biological samples. Recently, these modalities have shown great perspectives in imaging larger samples, at the cost of a clearing procedure, rendering the tissue optically transparent, alienating the photon scattering effects. In the typical implementation SPIM modalities rely on imaging the sample of interest with a thin sheet of light, recording 2D images with an orthogonally placed camera objective and appropriate imaging filters. Due to increased photon-scattering with depth, the penetration of SPIM imaging in transparent biological tissue is limited to a few hundred micrometers deep [103]. The central advantage of selective plane illumination microscopy techniques compared to standard bright field microscopy lies in the illumination pattern: the reduced thickness of the light sheet limits the sample's exposure to light, reducing the energy the sample is exposed to, and therefore reducing the bleaching effects. This particular characteristic allowed the development of novel insights in biological studies focusing on evolving stages of samples. The reduced photo-bleaching effects and non-invasive approach of acquiring cross-sections through entire living organisms enabled SPIM to gain access to in-depth dynamic morphological studies at early stages, where the tissue is still transparent.

Recently, several SPIM implementations have used more complex illumination modalities to improve the light-sheet thickness and uniformity. These implementations used multi-directional illumination [104], digital scanned laser light-sheet (DSLM) [105], self-reconstructing Bessel beams [106], and two photon excitation [106] to improve the illumination pattern. In spite all these efforts, SPIM's performance is considerably deteriorated once imaging scatter-

ing tissues. Developments on chemical clearing modalities not influencing the chromophores present in the tissue, allowed SPIM to image bigger biological samples, limiting the imaging to only *ex-vivo* samples sized up to a few millimeters. The quality of optoacoustic imaging on the other hand, is not severely affected by scattering of light in deep tissue. So far multispectral optoacoustic mesoscopy (MSOM) has revealed zebrafish anatomy [107] and fluorescent proteins expressed in (non-transparent) adult zebrafish and Drosophila pupae [27]. These previous studies used single detectors for acoustic detection, limiting the abilities of the system to produce three dimensional data-sets in a reasonable time frame.

In the current study, a new optoacoustic implementation centered around a SPIM microscope is presented. In the current implementation, a linear scanning geometry using an ultrasonic transducer is integrated to operate in parallel to a SPIM microscope. This hybrid instrument can theoretically enable a broad range of sizes and structures to be imaged, allowing biological studies to tracking the sample from infant stages up to adult developmental condition. By using a linear array transducer and parallel acquisition capabilities, the optoacoustic component is able to record volumetric images. From an image quality perspective, the system is developed to provide good quality images during the early development stages of the sample by using the SPIM mode, while optoacoustic imaging will provide good image quality and penetration depth in samples that become opaque at later developmental stages. Moreover, the ability to resolve multiple sources of contrast is a promising outcome of the hybrid system.

4.2. Materials and Methods

The experimental setup used in this study is presented in *fig.* 4.1. The hybrid system was composed of two separate imaging systems: the selective plane illumination microscopy and the optoacoustic imaging modality. The connecting link between the two imaging techniques was the thin plane of light, used by both systems. In the current, a separate description of the building blocks focused on the individual imaging modalities will be presented.

Optical excitation in SPIM mode
Optical and optoacoustic illumination was delivered from an OPO Spitlight laser, previously introduced in section 2.2.3. The laser is tunable in the $418-710$ nm range, a spectral area that is well suited for multispectral optoacoustic as well as selective plane illumination measurements of biological samples. Op-
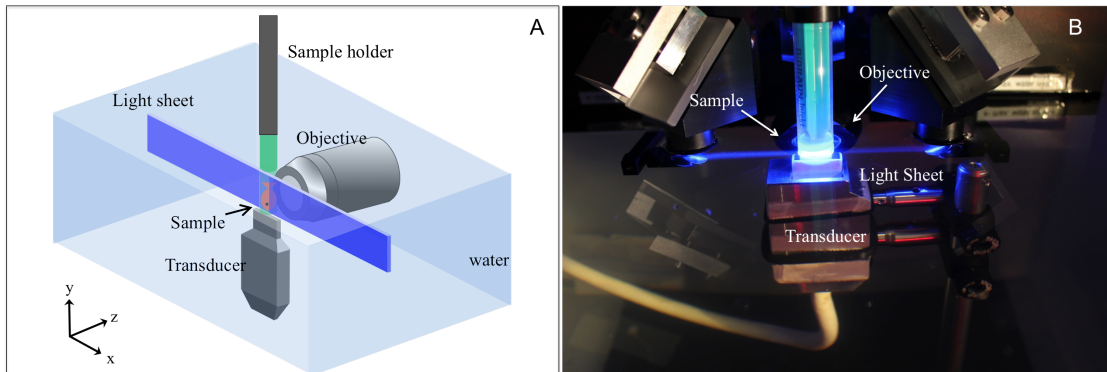
Figure 4.1.: Experimental setup. (**a**) Setup concept: the objective is orthogonal to the plane of illumination, while the focused plane of the ultrasonic transducer coincides with the thin light-sheet. (**b**) Photograph of the experimental setup.

tical excitation was delivered to the samples under investigation using a cylindrical lens ($f = 40$ mm). The cylindrical lens creates a light sheet, which is used to virtually section the object of interest. The beam waist of the light sheet depends on the optical properties of the specimen and was measured to be approximately $20\,\mu$m in the absence of scatter. In the current implementation the beam was split using a polarizing beam splitter to create a double-sided light sheet beam.

Ultrasonic transducer
Ultrasonic detection was performed with a linear ultrasonic array having 128 elements (Vermon 24 MHz). The transducer specifications were previously introduced in section 2.3. In the current implementation the transducer was fixed, arranged such that the focal plane coincides with the thin plane of illumination (*fig.* 4.1 **a** and **b**). The sample was placed on a holder, connected to one rotation stage, and two linear stages, allowing linear translation and rotation of the supporting phantom. The three positioning stages used in this implementation were necessary for aligning the sample with respect to the linear array and to the plane of illumination. The linear scanning detection geometry described herein was implemented by translating the sample, and not the transducer.

Scanning geometry - parameters and acquisition routine
During the acquisition routine, the camera objective and the linear transducer array remain stationary. In order to perform an initial alignment of the system, the transducer's focal plane and the thin plane of illumination had to be positioned along the same plane. During this calibration procedure, the focal plane of the transducer array is aligned collinear with the thin plane of illumi-
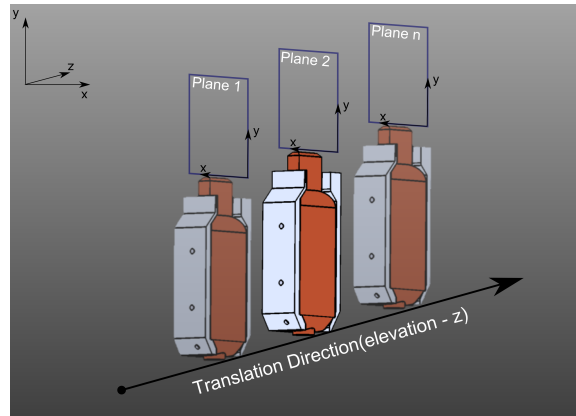
Figure 4.2.: Scanning Geometry: the ultrasonic linear transducer is placed under the sample, co-aligned with the plane formed by the thin-light-sheet.

nation. During the acquisition procedure, SPIM and OA data are acquired in consecutive steps. For the SPIM data set, the sample is translated through the illumination plane in $5\,\mu m$ steps, and the exposure time is adapted based on the sample, depending on the strength of the fluorescent signal. Consecutively, in the optoacoustic mode, the sample is translated through the illumination plane in $10\,\mu m$ steps, and a number of 20 averaged signals are recorded for each of the position. The step size was selected based on two aspects: on one hand the thickness of the illumination plane, and on the other characteristics of the ultrasonic transducer used. Based on the 24 MHz linear array used during this study, the focal spot specifications, as presented in section 2.3 are focal area length $1\,cm$ and focal area diameter $312\,\mu m$. During the experimental procedure, a sample translation step of $10\,\mu m$ ensured a good discretization of the acquisition domain.

Optoacoustic Image Reconstruction
Optoacoustic image reconstruction was performed using a GPU implementation of the algorithm presented in section 2.4. The acquired averaged signals were filtered according to the transducer specifications (2 - 40 MHz) using a 3rd order Butterworth bandpass filter. The backprojection algorithm was used to reconstruct 2D images on a grid with a pixel size of $12\,\mu m * 12\,\mu m$. In order to obtain a 3D representation of the reconstructed volume, the 2D images of the acquired cross-sections were stacked. Before reconstructing the entire volume, a representative 2D section was selected for speed of sound optimization (as described in section 5.2.3).

4.3. Combined System Characterization

In broad illumination configuration, the optoacoustic resolution depends on the ultrasonic diffraction limit [42] and is determined by the operation frequency and the geometrical characteristics of the ultrasound transducer. In the current section we present the results of the system characterization in terms of 3D resolution and spatial fidelity. The characterization was done using two different samples, created as described in section 2.5. The first phantom comprised of $10\,\mu m$ black microspheres (Carboxylated Polystyrene Microparticles, Polysciences Inc., Warrington, PA, USA) was used to characterize the 3D resolution of the system. A reconstructed MIP [2] image along the *xz* plane is presented in *fig.* 4.3 **a**, and the intensity profiles of the microspheres along each of the dimensions are presented in *fig.* 4.3 **b**. The resolution in terms of full width at half maximum (FWHM) was computed based on these profiles: the axial (*y*) and elevation directions (*z*) were determined to be $24\,\mu m$ and $20\,\mu m$, respectively, and the lateral (*x*) resolution of the system was $120\,\mu m$.
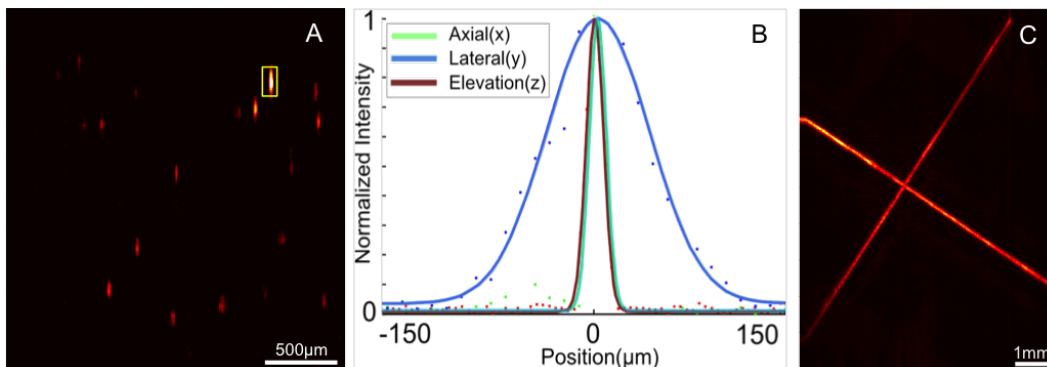
Figure 4.3.: Optoacoustic System Characterization. (**a**) MIP in the *xy*-plane of $10\,\mu m$ absorbing microspheres. (**b**) Intensity profiles along the three dimensions for the microsphere highlighted by the yellow box in **a**. (**c**) MIP in the lateral dimension *xy*-plane of the phantom comprised of the $20\,\mu m$ cross suture

The second phantom used for system characterization was composed of two black $20\,\mu m$ sutures (Nylon, non-absorbable monofilament, Vetsuture) embedded in scattering agar, arranged to build an "X" shape. The phantom was scanned in order to determine the system's ability to image a known absorbing

---

[2]Maximum intensity projection (MIP): rendering technique for 3D data-sets, projecting the maximum intensity of each pixel along a perpendicular direction with respect to the plane of visualization

structure and implicitly to determine if any inhomogeneities are present along the field of view. The phantom was placed perpendicular to the light sheet, i.e., along the *xz*-plane. *Figure* 4.3 **c** shows the MIP results through the phantom, which were used in determining the field of view (FOV) and the overall image reconstruction ability. The sutures appeared to be accurately reconstructed over a 10×10 mm^2 FOV, which is sufficiently large for the biological samples considered for this system.
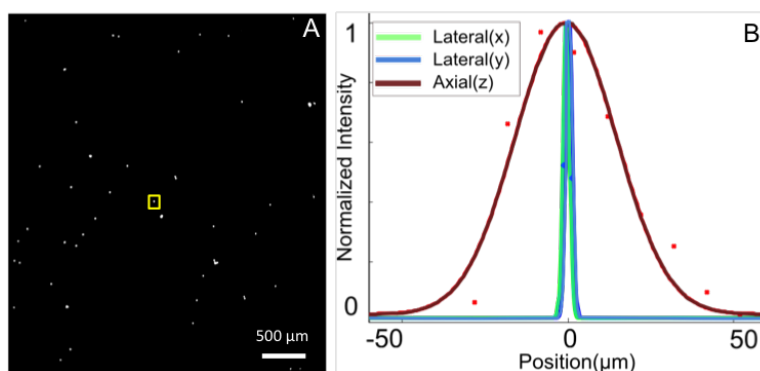
Figure 4.4.: SPIM System Characterization. (**a**) MIP of $10\,\mu$m fluorescent beads imaged using the SPIM mode. (**b**) Intensity profile of the bead highlighted by the yellow box in **a** when scanned along the *z*-axis (axial); in-plane lateral (*x* and *y* dimensions) resolution computed on $2.5\,\mu$m line-pair targets

For the SPIM mode, the system was characterized in terms of lateral (*xy*-plane) and axial (*z*-plane) resolution. The lateral resolution was computed based on a phantom comprised of resolution targets printed on a glass surface. The *xy*-resolution was found to be $2.5\,\mu$m. The axial resolution (*z*-axis) was defined by the light-sheet thickness and was measured by scanning a phantom comprised of $10\,\mu$m fluorescent beads (FluoSpheres, Life technologies) embedded in agar. The phantom was translated in $5\,\mu$m steps along the *z*-axis, and each of the image slices was acquired using a 400-ms/frame exposure time. *Figure* 4.4 **a** depicts the MIP along the *z*-axis of the fourth phantom scanned in the system. The FWHM was determined to be $36\,\mu$m. *Figure* 4.4 **b** shows the SPIM mode imaging resolutions in the three dimensions.

4.4. Application: Combined SPIM and OA on zebrafish imaging

The biological capabilities of the hybrid system were tested on an *ex-vivo* one-month old zebrafish, from a HGn39D transgenic line. The one month old zebrafish measured 10 mm in length and 3 mm in diameter. At this size, the entire thickness of the fish could be scanned using SPIM, but it would require prior chemical clearing. We imaged the fish in the hybrid system, without performing any preparation of the sample, as optoacoustic imaging is not affected by light scattering in these sort of thick specimens. The SPIM images were acquired using an excitation wavelength of 473 nm in conjunction with a $515/10$ emission fluorescence filter and an exposure time of 1.5 s/frame. The field of view of the camera objective used in SPIM acquisition mode was $3.32*2.8mm$, so in order to acquire the entire fish length, at least two separate positions had to be acquired. The first region was selected around the head area, while the second one was acquired in the tail area. The transducer array, in the current implementation had the length axis (*x-dimension*) measuring 127 elements $* 70\,\mu$m, so for the optoacoustic scan no lateral translation had to be performed, the fish being recorded on it's entirety. *Figure* 4.5 shows an overlay of the SPIM (green) and optoacoustic mesoscopy images (red) MIP along the *z*-axis. The optoacoustic overlay is reconstructed from 450 images of $20\,\mu$m thick slices, covering a total thickness of 9 mm. A bigger translation step was used during the biological sample imaging, for reduced light exposure and faster scanning times, providing no visible difference compared to the $10\,\mu$m step selected during system characterization. Moreover, the $10\,\mu$m step size ensured a safe discretization of the acquisition grid, although it was considerably smaller than the maximum wavelength corresponding to the highest recording frequency ($37.5\,\mu$m at 40 MHz). The imaged sample was a transgenic line, expressing green-fluorescent-protein (GFP) at the afferent neurons of the lateral line systems and along the trunk. The expression is recorded using SPIM mode, and is presented in the insets highlighted with the green box, *fig.* 4.5 as section 1 and section 2, respectively. Moreover, in SPIM mode several features can be distinguished, like the intricate fiber extensions around the head, the lateral line ganglia located at the anterior, posterior, dorsal and ventral sides of the ear. *Figure* 4.5 **b** and *fig.* 4.5 **c** show close-ups of the ganglion and of the ventral axon arbor structures. While the ganglia are easily recognizable in SPIM section 1, *fig.* 4.5 **b** shows that the individual somata making up the ganglia were still not well resolved due to scattering. The axon arbors seen in *fig.* 4.5 **c** are GFP positive fibers extending to terminate at neuro-

masts, which are clearly distinguishable. Optoacoustic mesoscopy images are shown to complement SPIM images by offering a complete anatomical view of the sample. The optoacoustic contrast observed is due to melanocytes and anatomical structures naturally absorbing light. Several other anatomical structures are highlighted in yellow in *fig.* 4.5 **a**. *Figure* 4.5 **d** shows a photograph of the zebrafish, used as a reference for opacity and size considerations.
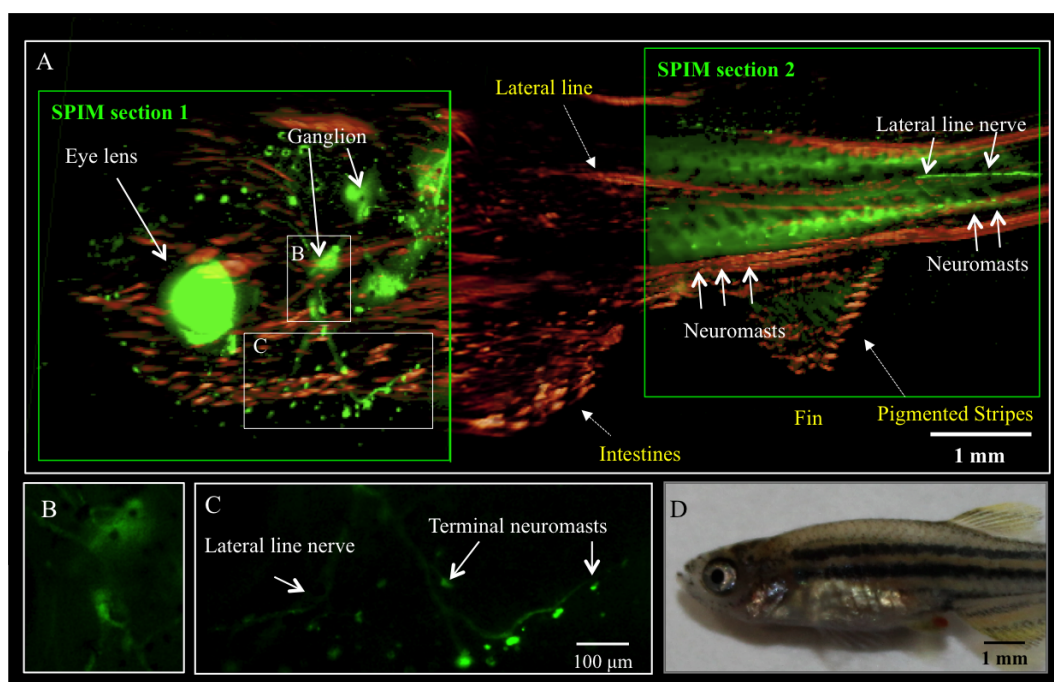
Figure 4.5.: SPIM and optoacoustic imaging - hybrid imaging of zebrafish. (**a**) Overlay of SPIM (green) and optoacoustic mesoscopy (red) images of the same zebrafish sample from the HGn39D line. (**b**) Close-up of a ganglion from SPIM section 1. (**c**) Close-up of ventral axon arbors extending to neuromasts from SPIM section 1. (**d**) Photograph of zebrafish

4.5. Discussion

Previously in the context of optoacoustic detection geometries, the same ultrasonic array has been used in a linear translation system, to image *in-vivo* mouse tumors and skin lesions [89]. In the aforementioned reference, the illumination was broad, illuminating the entire region of interest. The ultrasonic transducer

array was placed in between two flat fiber bundles. During the calibration procedure, the focal plane of the transducer was positioned to coincide with the plane of illumination. Nonetheless the illumination pattern was broad. Compared to this implementation, the current hybrid implementation is considerably superior with respect to resolution performance. The resolution characteristics of ultrasonic arrays have been previously summarized in section 2.3, but will be re-addressed here in the context. The axial resolution, or the resolution along the time axis, is dependent on the specifications of the ultrasonic transducer, and particularly the center frequency. The axial resolution, also termed the depth resolution, defines the capabilities of the system to distinguish two absorbers placed side by side along the beam direction. It is inversely dependent on the length of the ultrasound pulse. The transducer array used in the current study being a high frequency probe($>$10 MHz), attains a theoretical resolution of $20\,\mu m$ along the axial dimension, also confirmed by the practical implementation. According to the implementation, a high-frequency linear array will ensure high-resolution imaging of the biological samples, without having to address limitations on frequency attenuation issues, as the samples are rather reduced in size (zebra-fish or small organs).

The second component contributing to the spatial resolution is the lateral resolution, and is primarily dependent on the width of the transducer and central frequency specifications. The lateral resolution is defined as the ability to distinguish between two absorbers placed along the beam width. This implies that a transducer array with elements packed closer together, like the one currently used (pitch $70\,\mu m$) will provide a better lateral resolution. Moreover, a higher central frequency will enable a narrower beam width, allowing a better lateral resolution. In the case of the Vermon 24 MHz linear array used in this implementation, the $70\,\mu m$ pitch is currently considered state of the art, and closely packing 128 elements with the small inter-element spacing (kerf), allowed a wide aperture of almost 9 mm (127 elements $*$ $70\,\mu m$ pitch), enabling recording of an entire one month old fish (1 cm in length), without any mechanical scanning of the array. The theoretical resolution of the system of $20\,\mu m$, operating using optical excitation generated by the thin plane of illumination, was experimentally confirmed by scanning the $10\,\mu m$ microspheres, absorbing structures generating a broad frequency response.

The third component of spatial resolution is the elevation resolution, defining the slice thickness. Usually, this component is the limiting factor of linear arrays. In general, a focusing lens is added to the linear arrays in order to improve the resolution along this dimension, and remove the out-of-plane contributions. In the current case, the transducer array was cylindrically focused

using a silicon lens. In spite of this modality, acoustic focusing is not ideal as it is dependent on the frequency and depth of the recorded spectrum. Moreover the depth of field and the focusing of the array are dependent quantities: a deeper depth of field will come at an expense of reduced focusing capabilities, and implicitly poor resolution along the elevation dimension. Merging the three components of the spatial resolution, in a broad illumination configuration, will result in an anisotropic resolution. So far, different algorithms have focused on attenuating and improving the resolution along this dimension in linear translation systems [108], without attaining homogeneous resolution in the entire field of view. Additionally, deconvolution approaches have investigated the possibility to improve the quality of images obtained in translation based systems, but the improvements were frequency and location dependent [109]. In a previous study using the same transducer array and broad sample illumination the characterization of the system resulted in a resolution along the elevation dimension of approximately $300\,\mu\mathrm{m}$ [89]. The current setup, however, takes advantage of the slice thickness required for the light-sheet illumination and therefore offers improved elevation resolution. This metric can change for thicker samples because photon diffusion would cause broadening of the thickness of the excitation plane, but nonetheless the excitation slice thickness will remain considerably reduced compared to broad illumination setups.

In the current implementation from a detection point of view, linear arrays have a clear advantage over raster scanning techniques approaches[63] with respect to parallel acquisition. Implicitly the temporal resolution will be improved, and by taking advantage of the thin plane of illumination acoustic detection can be much better confined to the plane of origin. Raster scanning approaches could potentially increase the in-plane resolution by performing a more dense discretization of the acquisition grid. A more dense discretization grid enabled by a raster-scan approach this will induce additional time delays, but could potentially enable local shorter scans focusing only on a region of interest. Both raster scanning and linear translation geometries will still suffer from single-sided access around the sample, potentially introducing limited view artifacts. This effect can degrade the quality of acquired images by not resolving structures emitting parallel to the detection plane, in particular the ones which are positioned perpendicular to the array and in the median imaging plane. A possible solution, retaining a planar detection single-sided access geometry, has been proposed in [110], where an oscillation of the array is included in addition to the linear translation of the array. This scanning approach can mitigate the limited view effects introduced by the focusing lens, but not the artifacts and limitation introduced by the finite size of the array.

To summarize, from a combined hardware and application point of view, the advantages of using SPIM as an imaging modality are broad, and cover applications ranging from visualization of small transparent samples to cleared *ex-vivo* organs. SPIM allows volumetric visualization of small organisms, and allows tracking them through their developmental stages, due to it's high acquisition frame-rate, optical microscopy resolution and low photo-toxicity. However, the performance of SPIM imaging quickly deteriorates when applied to opaque tissue due to increased photon scattering in tissue. To overcome this limitation, in the current work, SPIM optics were merged with optical and optoacoustic readouts. The performance of this hybrid imaging system was characterized using various phantoms and by imaging a highly scattering 1 month old zebrafish, measuring $1\,\mathrm{cm}$ in length. The results revealed the system's enhanced capability over that of conventional SPIM for high-resolution imaging over extended depths of scattering content. The approach described here may enable future visualization of organisms throughout their entire development, encompassing regimes in which the tissue may become opaque.

Chapter 5.

Cylindrical Tomographic Optoacoustic Imaging

In the current chapter, a second detection geometry was investigated in the context of mesoscopic optoacoustic imaging, using linear ultrasonic arrays. The geometry performs a cylindrical coverage of the detection grid (see *fig.* 2.3 **b** for clarification). Some of the results presented in this chapter are also presented (at places with minimal or no changes) in the publication entitled:

- "High-resolution optoacoustic mesoscopy with a 24 MHz multidetector translate-rotate scanner" by Jérôme Gateau, Andrei Chekkoury and Vasilis Ntziachristos, published in the Journal of Biomedical Optics 18(10), 106005, (October 2013) [111].

5.1. Motivation

Currently, several optoacoustic tomographic configurations have been implemented using spherical, cylindrical, or planar detection surfaces. The choice of detector implementation is ultimately dictated by the envisioned application, but must consider the properties imposed by the detecting geometry, the illumination delivery path and the access to the sample under investigation. Optoacoustic imaging, due to light scattering in biological tissue, is inherently a three dimensional imaging modality. Currently, several small animal systems were implemented using curved arrays - see section 3.1 (MSOT 256). The acquisition procedure relies on translating the concave array in incremental steps, acquiring cross-sections of the sample placed inside the detection surface. The geometry attains good resolution in the *xy*-plane, but due to the focusing abilities of the array the resolution along the *z*-axis is degraded and non-uniform along the imaging plane. These effects influence the result of acquiring volumetric datasets, creating anisotropic resolution.

The previously proposed geometry (chapter 4), involving a linear translation of the transducer array is advantageous in a configuration benefiting from focused illumination, coherent with the transducer's plane of detection. This implementation confines the origin of optoacoustic signals to the thin plane used for optical excitation. From an ultrasonic detection perspective, the elevation resolution (z-plane) is considerably improved, but the single sided detection might implicitly generate limited view artifacts, and the directivity of absorbing structures can render them invisible to OA detection (i.e. a vessel parallel to the illumination plane, found in the middle plane of the array, perpendicular to the probe, will not be recorded, emitting only in directions not covered by the acceptance of the probe).

To be able to reconstruct the volumetric distribution of optical absorption, a tomographic detection where ultrasound detectors are distributed on a surface surrounding the sample is presented. The detection geometry relies on using linear arrays scanned and translated around the object in order to encompass the sample. The geometry is similar to the first generation X-Ray CT scanners, and the detection covers a large solid angular aperture around the sample, allowing true volumetric detection of the optical absorption deep inside tissue. The proposed geometry offers an alternative to complex algorithms developed to mitigate the artifacts generated by signal generated outside of the plane of interest during cross-section imaging acquisitions.

5.2. System Characterization

In the current section, the scanning geometry will be introduced and a discussion regarding acquisition parameters, calibration and reconstruction routine will be done. A comparison between different acquisition routines will be discussed, followed by a section presenting the system characterization results.

5.2.1. Step by Step Mode of Operation

In optoacoustic imaging, the geometrical displacement of ultrasonic transducers affects the spatial resolution and the visibility of absorbing structures in the sample under investigation (see section 2.1.4). Moreover, additional aspects like the electrical and spatial impulse response can influence the image quality (see section 2.1.4). In order to integrate the sensitivity patterns of the linear arrays, the proposed geometry accounts for the hardware specifications and for the wave detection capabilities of these detectors, adjusting to the ability to record

optoacoustic signals from a large angle around the sample. Moreover, the geometry aims at providing the ability to reconstruct complex absorbing structures in intact samples of mesoscopic size. The optoacoustic scanning geometry described herein resembles the first generation of computed tomography x-ray imaging, where for each rotation position of the detector additional translation positions are performed, and was previously introduced in [71].
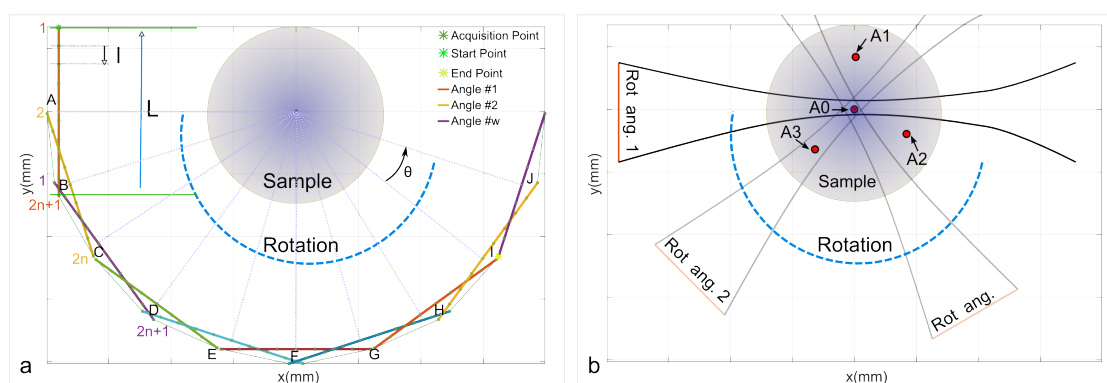
Figure 5.1.: Scanning geometry: (**a**) The translate-rotate geometry performs a series of consecutive translations for each angular position of the tomographic arrangement. (**b**) Schematic exemplification of the sensitivity field of a linear array in a rotation only setup. Legend: L - total translation range; l translation step size; θ angular coverage; $A, B...$ angular positions; $A0 - A4$ absorbers inside the scanned sample;

In the current implementation, the linear array is positioned around the sample using a translate-rotate scheme. The lateral movement of the linear array describing the translation range of the probe, defines tangent segments to a circle centered on the axis of rotation (*fig.* 5.1 - point marked origin). The linear motion describes a polygon, as can be seen in *fig.* 5.1 **a**. The size of the polygon is dependent on the diameter of the sample to be scanned. The radius (R_tomo) of the circle described by the transducer is selected to correspond to the focal distance of the array. The angular sampling is selected to be $\theta = 1.5°$ degrees, and it covers $180°$ - θ angles. While the rotation coverage was predefined, the translation range was selected depending on the imaged sample. In *fig.* 5.1 **a** the translation range (labeled L) is performed for each of the angular positions of the linear array (labeled with capital letters). The number of incremental steps (n) performed for each linear motion is defined by the physical properties of the transducer used, and the step size (l) is chosen to correspond to the full width half maximum (FWHM) of the sensitivity field at the focal spot of the array (l_0). During the acquisition routine, the linear positions were spaced by twice the

FWHM ($l = 2 * l_0$), to reduce the acquisition time. To record complementary information, alternative patterns were recorded in consecutive angular positions by shifting the translation position by half the step length (l_0) in between two adjacent translation segments: i.e. in *fig.* 5.1 **a** for angle A, a number of $n + 1$ stops were performed, while for angle B, a number of n stops were performed, respectively.

The necessity of a translation of the linear array is graphically exemplified in *fig.* 5.1 **b**, where the sensitivity field of the array is depicted as the curved black linear. The scheme shows three different angular positions of the array in a rotation only environment. It can be seen that two of the absorbers inside the tissue (A2 and A1) are not recorded inside of either one of the angular views, leading to insufficient tomographic acquisition points. The absorber termed A3, is recorded during the projection angle 2, but due to a reduced number of projections, it will not be accurately reconstructured. Compared to the three other absorbers, only absorber A0, placed in the center of rotation will have sufficient views to be accurately reconstructed. By linear translating the sensitivity area of the array along the sample, an increasing in the angular aperture along this dimension is performed, enabling a higher number of projection views over the entire surface of the sample.

The cylindrical implementation of this optoacoustic scanner is composed of three parts and is presented in *fig.* 5.2:

- The optical excitation is composed of a tunable ($690 - 900\,\mathrm{nm}$) OPO laser (see section 2.2.3) and a 4 arm fiber bundle composed of 640 fibers (Ceramoptec). The fibers were positioned $5\,\mathrm{cm}$ away from the sample to completely illuminate the object of interest. The fibers were stationary and placed on a single side.

- The ultrasonic detection was performed successively, using two linear arrays. Both transducers had 128-elements and were cylindrically focused (see section 2.3 for details). The system accommodates the use of both transducers previously introduced in section 2.3.

- The array is held by a specially designed holder, which is attached to the linear motorized stage (M-605.2DD, Physic Instrimente, Karlsruhe, Germany). The linear stage is connected to the rotation stage (M062.PD, Physik Instrumente, Karlsruhe, Germany) enabling the possibility to rotate the linear stage.

5.2.2. Image Reconstruction and Visualization

In the cylindrical configuration the reconstruction was performed as previously presented in section 2.4, with a few additional modifications, dependent on the

linear array used to record the signals. The backprojection was performed on a cuboid, centered on the measurements coordinate system. For each z-plane (height), 2D images were reconstructed using all the recorded signals. As in ultrasound imaging, a dynamic aperture implementation was used in order to maintain a fixed angle of acceptance along the z-axis of the array.

In ultrasound implementations, dynamic aperture is used to maintain a uniform width of the focus over the entire imaging field, by increasing the number of elements used to receive echoes with an increased imaging depth. In the current implementation, the dynamic aperture was implemented along the z-axis, by using an F-number in receive (ratio of depth to entire array aperture length)

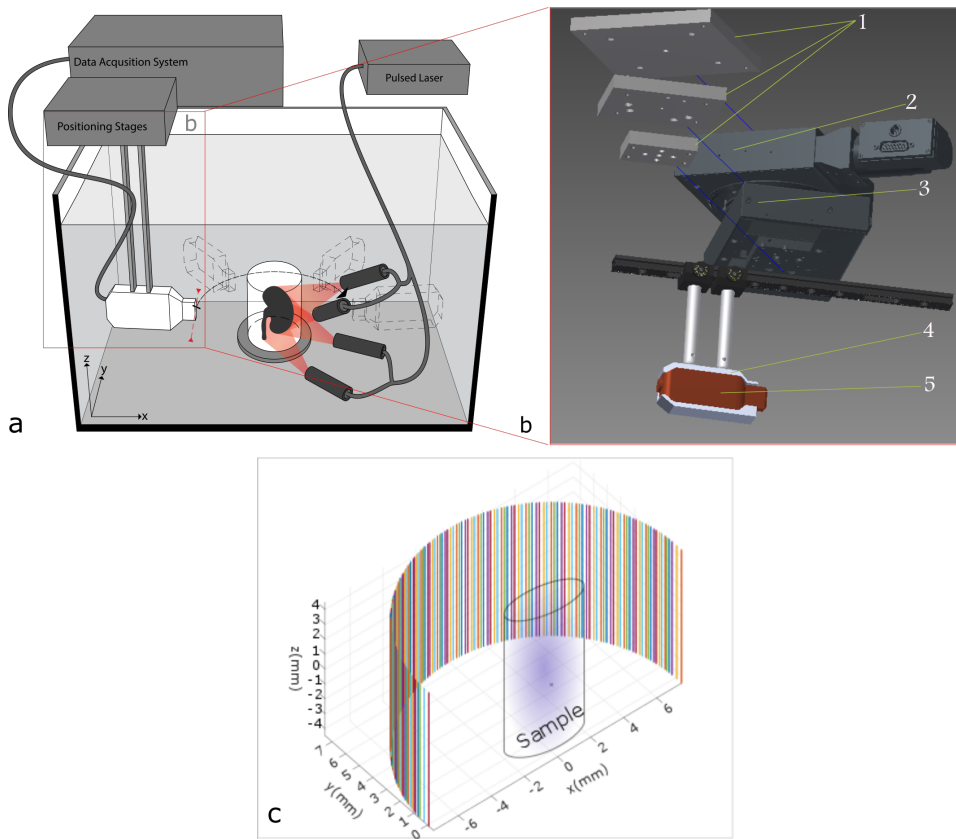**Figure 5.2.:** Cylindrical tomographic optoacoustic setup (**a**) - altered for optimal visualization; not up to scale) and building blocks (inset - (**b**) - up to scale); Legend: (1): Adapting plates; (2) Rotation Stage; (3) Translation stage; (4) Transducer Holder; (5) High Frequency Linear array; (**c**) The cylindrical enclosure of the detector displacement positions around the scanned sample.

of 0.5 for the low-frequency array (6 MHz) and 0.8 for the high-frequency probe (24 MHz). This implied that although all signals were used during the reconstruction of a 2D cross section, a constant angle of acceptance was kept along this dimension, enabling a homogeneous contribution of signals to each of the reconstructed planes.

The images reconstructed using the filtered backprojection algorithm contained negative values, which had no physical meaning. Noise and negative value removal was performed by computing the histogram of the image and removing the voxels with values below the maximum of the histogram. Moreover, for improved visualization purposes, the last $0.02\% - 0.1\%$ values were saturated.

5.2.3. Calibration and Mechanical Parameters

During the reconstruction procedure, the location of the detection points around the sample must be precisely known for accurate backprojection of the signals on the detecting grid. In order to account for the small offsets introduced by the multitude of components used to assemble the system, a calibration routine was developed. To calibrate the optoacoustic system for optimal performance, several parameters had to be taken into account, and are summarized in *fig.* 5.3: the rotation radius (R_tomo) is a measurement distance and it specifies the length of the segment described by the transducer with respect to the center of rotation (*fig.* 5.3 **a**). The second parameter is the offset with respect to the center of rotation, L_tomo, and is a distance measured in micro-metres specifying the difference between the center of the translation step and the real center position (*fig.* 5.3 **b**). The third parameter is the vertical angular offset, α_tomo, defining the angular displacement of the array with respect to the vertical axis (*fig.* 5.3 **c**). The fourth parameter is the lateral angular offset of the array(β_tomo) with respect to the vertical axis (5.3 **d**). Overall the calibration procedure optimizes the four degrees of freedom considered for the detector's position: two distances (R_tomo and L_tomo), two angular displacements (α_tomo and β_tomo), and the varying speed of sound, dependent on the sample and coupling medium **c**. Theoretically, a fifth parameter should be considered during the calibration procedure, specifically the angular rotation of the array with respect to its own axis. This angular parameter is more difficult to be assessed, as it requires the use of a model-based reconstruction algorithm, where the transducer elements are not considered point-detectors, but finite sized discretized quantities.

The two different detector arrays used throughout this work were alternated during the optoacosutic scanning procedure. The arrays were positioned in
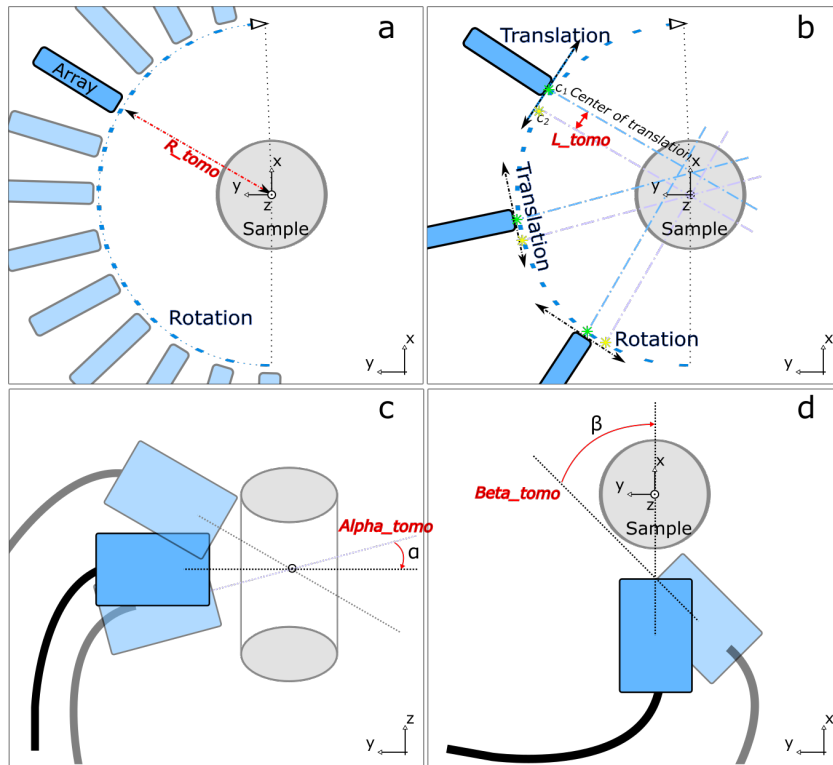
Figure 5.3.: System calibration parameters: (**a**) Rotation radius described by the sensor position R_tomo (**b**) Displacement of the rotation with respect to the absolute center of rotation: L_tomo (**c**) Vertical angular offset of the transducer α_tomo (**d**) Lateral angular offset of the transducer β_tomo

custom built holders, created using different typical laboratory posts. In addition, the mounting procedure, involved attaching the two detectors in an interchangeable position on the positioning stages. This procedure was performed several times during a typical acquisition routine. The two arrays had different apertures and different focal distances. For particularly this reason, a thorough calibration method enabling accurate detection of the sensor position had to be performed. In the following, the calibration procedure is described and the typical artifacts generated by miss-calibration of the presented hardware is described.

Initial placement of the transducer array took into consideration the focal distance of the probe which had to coincide with the centre of rotation, and the height of the probe with respect to the measured sample. This initial alignment of the system was performed using a single synthetic absorber, like a micro-

sphere, which is also used for the speed of sound calibration. After performing a rough calibration accounting for the center of rotation (in the following will be denoted by R_tomo) and the displacement of the array with respect to the absolute center (in the following will be denoted by L_tomo), a custom built absorbing phantom was used for calibration purposes. The phantom was comprised of two parallel sutures, of small diameter ($20\,\mu$m) and $1\,$cm in length, placed parallel to the long axis of the transducer (z-axis throughout this chapter). During the calibration procedure, the four parameters previously introduced were optimized by considering the following routine: a pre-defined number of horizontal planes (5-6 planes) were selected at different heights (locations along the z-axis) of the acquired volume, and the cross-sections were reconstructed. The sutures were selected as calibration absorber, as they are invariant over a large distance, so the planes selected for optimization can be picked up arbitrarily. The reconstructed image was split into two different areas, including only one vertical suture per image. This procedure, ensured that the angular offsets, specifically the lateral and the vertical offset will be optimally taken into account, by considering the entire aperture of the probe and the length of the sutures to be approximately equal ($1\,$cm). In this way, any offset of the probe, lateral or vertical, will be accounted in respect to the calibration sample. The calibration algorithm, accounted for the four parameters, by maximizing the mean intensity calculated per each of the sub-regions, corresponding to each individual absorbing thread of suture, following an optimization loop running through a range of manually adjusted parameters. The goal of the optimization algorithm was to accurately extract the four degrees of freedom considered to influence the position of the detectors, by maximizing the reconstructed signal intensity of the reconstructed parallel suture.

In the following, a study of the 4 different calibration parameters and the speed of sound influence on the quality of the final image are presented on an experimentally acquired data-set.

The first parameter considered during the calibration procedure was the radius described by the central point of the array with respect to the absolute center (termed here R_tomo). The sample was placed in the center of rotation by visual inspection. In order to obtain the best image quality, the transducer array had to be positioned such as the focal distance (19 mm for the 6 MHz probe and 7.5 mm for the 24 MHz array) coincides with the radius. The artifacts introduced by a non-accurate R_tomo parameter are presented in *fig.* 5.4. For comparison reasons, the calibrated reconstruction is displayed in sub-figure **k** as a lateral MIP view, and **j** as a 2D cross-section taken at a central plane, depicted by the orange dotted line in sub-figure **k**. The simulated offset parame-

ters are ranging from small variations: $-100\,\mu$m in **a**, $100\,\mu$m in **c** up to $500\,\mu$m in **b** and $-500\,\mu$m in **d**. It ca be seen that the effect of a not calibrated radius value, introduces artifacts manifested as circles with different radius (sub-figure **e-h**). A considerable miss-calibration will exhibit massive circular structures **f** and **h**, while smaller variations will introduce smaller errors on the reconstructed image.
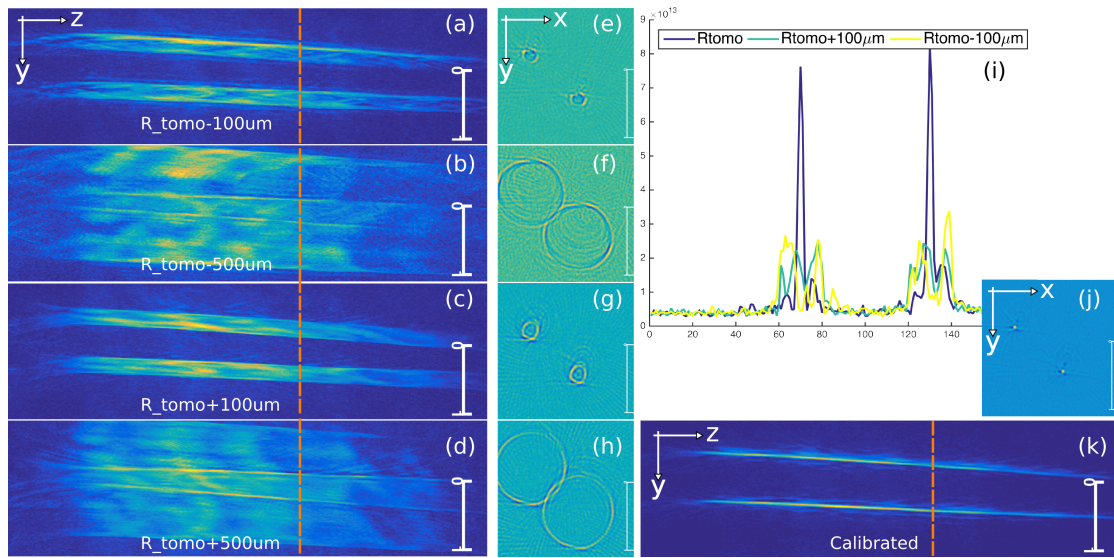
Figure 5.4.: System Calibration - R_tomo: Rotation radius described by the sensor position and influence on the image quality; Offset from the calibrated value displayed as a MIP lateral view (yz-plane) and 2D plane (xy-plane): (**a**) and (**e**) $-100\,\mu$m; (**b**) and (**f**) $-500\,\mu$m; (**c**) and (**g**) $100\,\mu$m; (**d**) and (**h**) $500\,\mu$m; (**k**) and (**j**) calibrated parameters; (**i**) Profile plot along the dotted line, showing the influence of R_tomo $\pm\,100\,\mu$m on the resulting reconstructions.

The second parameter accounted for during the calibration procedure was the offset to the center of rotation (L_tomo). As previously described in the section 5.2.1, the lateral translation of the array describes linear segments tangent to the circle centered on the axis of rotation. The center point of this translation motion is performed with respect to the middle point of the circle and should coincide with the axis of rotation. The L_tomo parameter along with the rotation radius are the two parameters which can be manually adjusted during the alignment process of the system, but need to be further refined, as it can depend on additional factors not accounted for during the initial phase. The artifacts introduced by small variations in the value of L_tomo are presented in *fig.* 5.5, where small offsets are introduced. Even though on the MIP lateral

view, the parallel sutures appear similar, it can be seen that on a cross-section level (**e-h**), the background value is different, and the blurring patches above and under the sutures in **b** and **d** are signs of a miss-calibrated system.
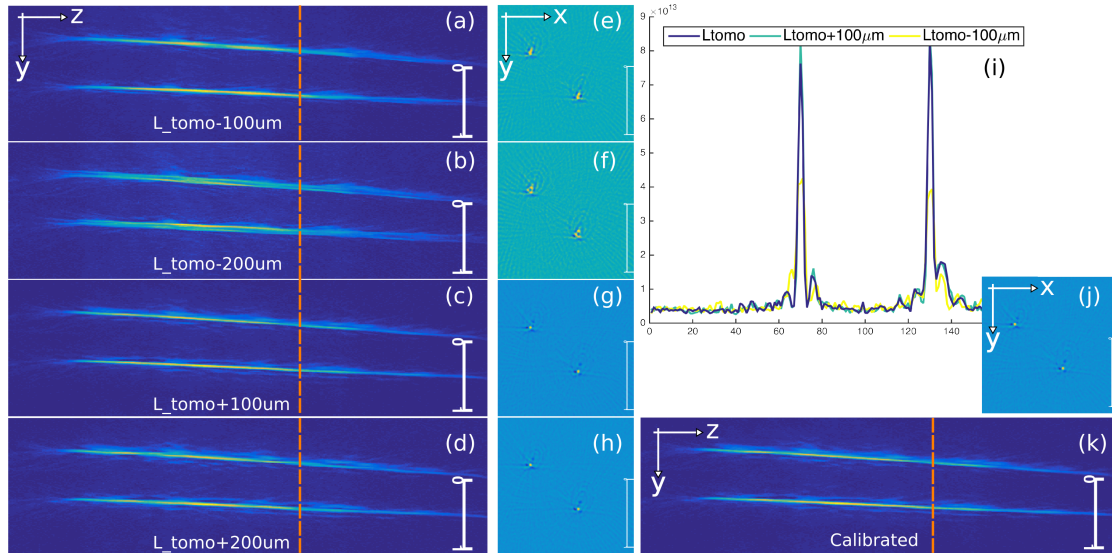
Figure 5.5.: System Calibration - L_tomo: Linear offset to the center of rotation. The effects of small variation from the calibrated value displayed as a MIP lateral view (yz-plane) and as a 2D plane (xy-plane): (**a**) and (**e**) $-100\,\mu$m; (**b**) and (**f**) $-200\,\mu$m; (**c**) and (**g**) $100\,\mu$m; (**d**) and (**h**)$200\,\mu$m; (**k**) and (**j**) calibrated parameters; (**i**) Profile plot along the dotted line, showing the influence of L_tomo $\pm\, 100\,\mu$m on the resulting reconstructions.

The third degree of freedom considered during system's calibration was the vertical angular offset with respect to the axis of rotation, or the vertical direction pointed by the transducer array (up-down direction), and is termed here α_tomo. Different building blocks attaching the transducer to the positioning stages can introduce angular displacements of the probe with respect to the absolute center of the imaging system. One of them is the angular tilting with respect to the vertical (z) axis of the sample, created in the z-plane, termed here α_tomo. *Figure* 5.6 summarizes the artifacts introduced by a possible miss-calibration of the vertical offset. It can be seen that variations of the vertical tilting can render faulty the reconstruction of the parallel sutures: a fan-beam appearance of the sutures around one of the ends. On a cross-section level (fig 5.6 **e - h**, the same circular artifacts present in while oscillating the radius offset can be seen, but this is rather due to the selected position of the cross-section plane.

The fourth parameter considered during system's calibration was the lateral

Figure 5.6.: System Calibration - α_tomo: Vertical angular offset of the transducer. The effects of small variation from the calibrated value displayed as a MIP lateral view (yz-plane) and as a 2D plane (xy-plane): (**a**) and (**e**) -1 deg; (**b**) and (**f**) -3 deg; (**c**) and (**g**) 1 deg; (**d**) and (**h**) 3 deg; (**k**) and (**j**) calibrated parameters; (**i**) Profile plot along the dotted line, showing the influence of α_tomo ± 1 deg on the resulting reconstructions.

angular offset with respect to the axis of rotation, or the lateral direction pointed by the transducer array (right-left direction), and is termed here (β_tomo). The artifacts introduced by an erroneous value of the lateral angular offset, which is the angle created by the transducer with respect to the vertical axis in the *xy*-plane, can be seen in *fig.* 5.7. Even though, apparently, small changes in the value selected for β_tomo do not influence much the quality of the reconstructed parallel sutures, in reality, the coupling between all reconstruction parameters can prove of high-importance. The experimental procedure showed the possible dependence of these degrees of freedom, meaning that optimal selection of the three parameters, limit to possible variation on the fourth parameter to only a handful of solutions.

Speed of sound selection is a topic of broad research in the optoacoustic field, and has been the central subject of several studies [112]. In the current section, we present an optimization procedure, meant to adjust the quality of the images depending on the value selected for the speed of sound. The optimization procedure consists on maximizing the amplitude of the reconstructed image for a linearly varying speed of sound value. It is important to note, that even though presented as a last parameter on the list of possible offsets and variables influ-
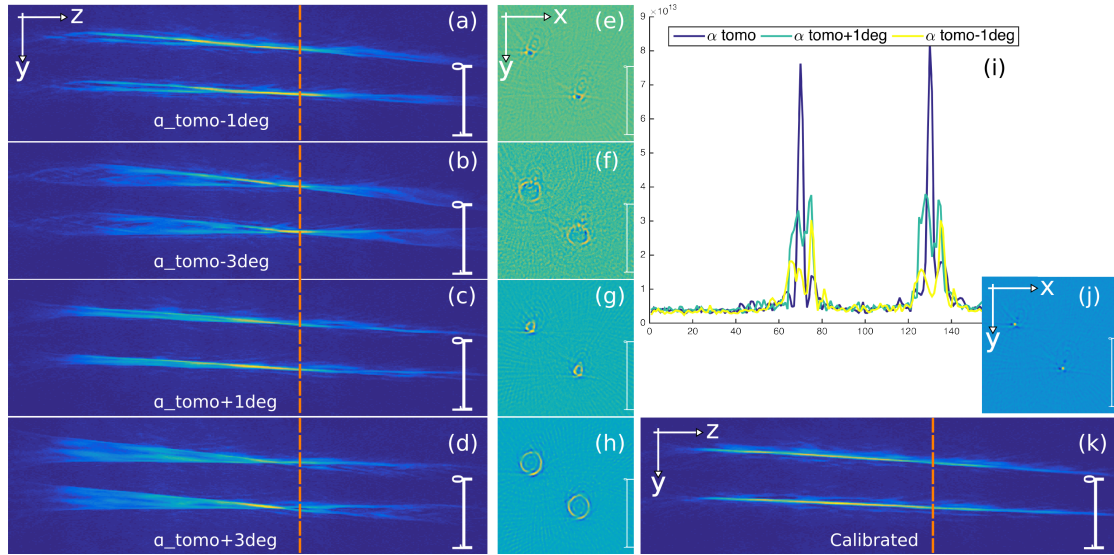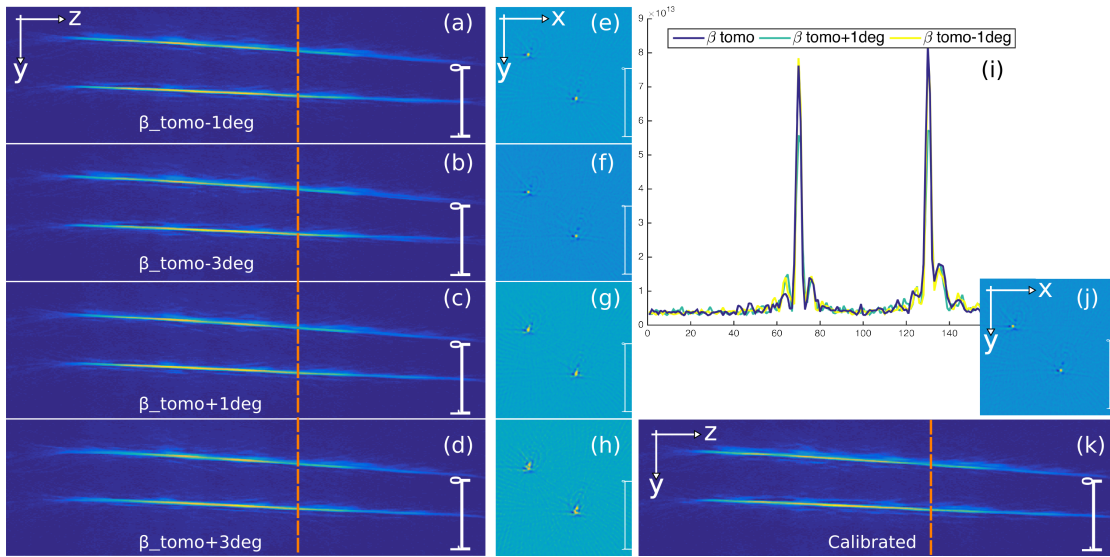
Figure 5.7.: System Calibration - β_tomo: Lateral angular offset of the transducer. The effects of small variation from the calibrated value displayed as a MIP lateral view (yz-plane) and as a 2D plane (xy-plane): (**a**) and (**e**) -1 deg; (**b**) and (**f**) -3 deg; (**c**) and (**g**) 1 deg; (**d**) and (**h**) 3 deg; (**k**) and (**j**) calibrated parameters; (**i**) Profile plot along the dotted line, showing the influence of β_tomo $\pm$ 1 deg on the resulting reconstructions.

encing the image quality, the speed of sound is the first parameter considered before the calibration step, and before each of the reconstructed data-sets. During the initial placement and assessment of the parameters, the speed of sound of a know isotropic absorber (microsphere) is predetermined. This is important, as the artifacts introduced by different angular or distance offsets, might resemble the ones introduced by variations in the speed of sound. In *fig.* 5.8, the variations on the value of the speed of sound, are analyzed: a variation as small as 5 m/s can induce strong artifacts, limiting the quality of the reconstructed image. The variation is also assessed on a cross-section level, where, as previously mentioned the dot-like structures obtained with an ideal value, turn into small circular structures.

5.2.4. System Characterization

In the current, the geometry previously described was implemented with the 24 MHz linear array introduced in the section 2.3.

System characterization in terms of 3D resolution performance with respect to isotropic absorbers was performed using one phantom comprised of $10\,\mu\text{m}$
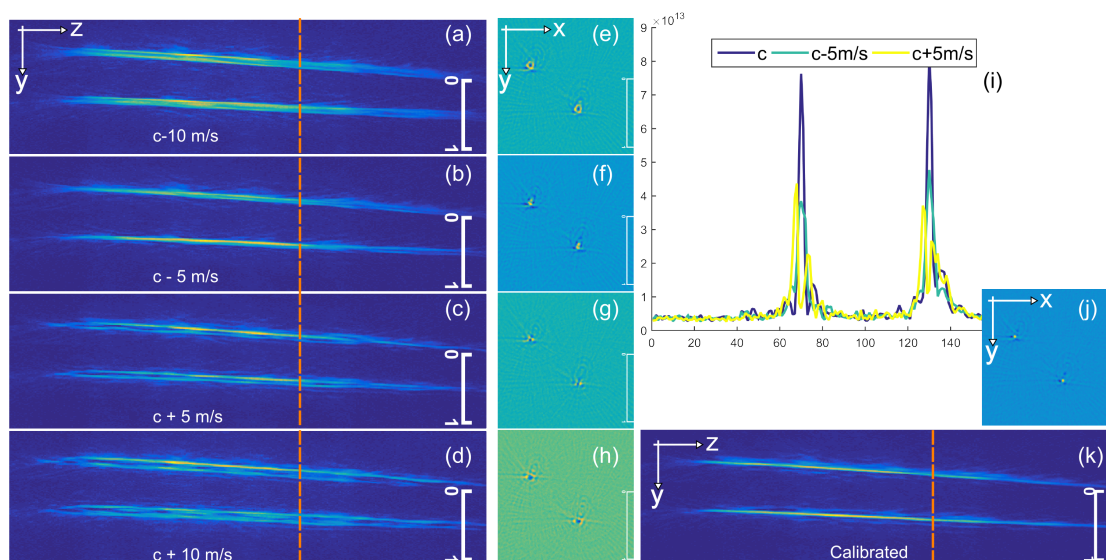
Figure 5.8.: System Calibration - speed of sound: The effects of small variation from the calibrated value displayed as a MIP lateral view (*yz*-plane) and as a 2D plane (*xy*-plane): (**a**) and (**e**) -10 m/s; (**b**) and (**f**) -5 m/s; (**c**) and (**g**) 5 m/s; (**d**) and (**h**) 10 m/s; (**k**) and (**j**) calibrated parameters; (**i**) Profile plot along the dotted line, showing the influence of $c \pm 10$ m/s on the resulting reconstructions.

diameter black polystyrene microspheres (carboxylated polystyrene microparticles, Polysciences Inc., Warrington, PA). The microspheres were randomly distributed in the agar solution and the mold was created by filling the supporting sample with the so-created solution. Based on the laser pulse duration used in this study, the microspheres should emit optoacoustic signals with a frequency content greater than the maximum frequency recorded by the detector used. The phantom was scanned using an averaged acquisition mode, with a translation range of 9 mm. *Figure* 5.9 **a** and **b** show maximum intensity projection (MIP) images of the reconstructed volume, over a 2.1 mm thick region (*z*-axis), from a top view in **a** and lateral view in **b**. Three different microspheres originating at different in-plane levels and out-of-plane depths were selected for resolution characterization studies. Each of the extracted volumes corresponding to single microspheres measured $9 * 9 * 11$ voxels and MIP views are presented in the colored rectangle view. Throughout the reconstructed volume, the microspheres were consistently looking like rice-grains, with an elongated shape along the *z*-dimension. The FWHM dimensions of the MIP profiles for the three microspheres were determined to be equal to (mean $\pm$ standard deviation) $29\pm 2\,\mu\mathrm{m}$ along the *xy* plane and $110\pm 5\,\mu\mathrm{m}$ along the *z*-plane.
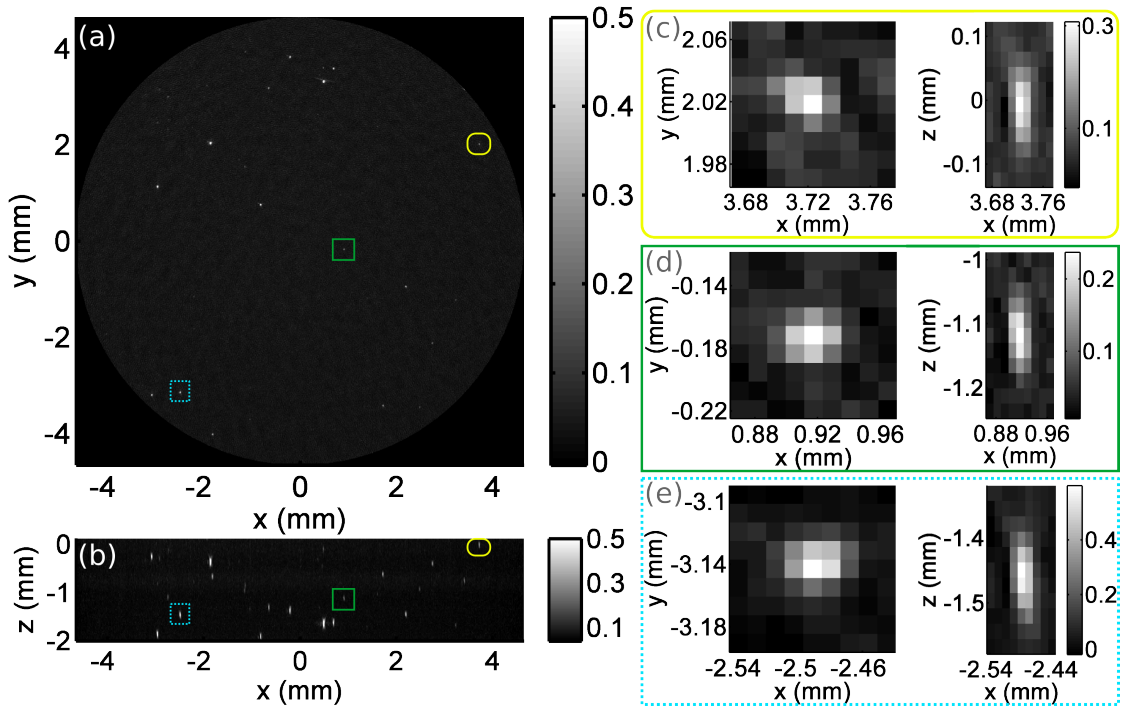
Figure 5.9.: Reconstruction of a 2.1 mm-thick volumetric slice of Phantom 3 (comprising ⊘ 10 µm microspheres randomly spread over the volume). (**a**) MIP image along the *z* axis. (**b**) MIP image along the *y* axis. The superimposed rectangles indicate the limits of three subregions of interest. (**c**), (**d**), and (**e**) MIP images of these sub-regions along the *z* axis (left) and the *y* axis (right).

To characterize the system in terms of spatial fidelity two phantoms comprised of 20 µm diameter suture (NYL02DS, 10/0, Vetsuture, Paris, France) were used. In the first phantom the black suture threads were arranged to form a cross along the length of the cylinder (Phantom 1), while in the second phantom, the sutures were arranged to create a two loop knot (Phantom 2). Both these phantoms were scanned in averaged acquisition mode, using a translation range of 5.1 mm, corresponding to the maximum in-plane radius of the volume of interest. *Figure* 5.10 shows the reconstruction of the two phantom containing the cross 20 µm diameter sutures. *Figure* 5.10 **a** and **d** show a MIP image of the reconstructed volume along the *zy*-plane, corresponding to a lateral view of the sample. The reconstructed volumes are accurately resolved over the entire height of the array (8.89 mm) with a consistent resolution for different kinds of absorber orientations (*fig.* 5.10 **d** and **e**). MIP images of the top view (*xy*-plane) are displayed in *fig.* 5.10 **b** and **e** and show the system's

performance with respect to complex absorbing samples. A 2D slice was selected from the reconstruction of Phantom 1 (*fig.* 5.10 **a** - red marker) close to the saddle point of the suture, in order to assess the resolution in terms of object separability. The image is displayed in *fig.* 5.10 **c** and the distance between the two maxima corresponds to the resolution in the sense of the Sparrow resolution criterion and was determined to be 51 μm. A 2D slice was selected from the reconstruction of Phantom 2 (*fig.* 5.10 **f** - yellow marker) and shows a cross-section depicting different orientations of the suture. The artifacts present in the image are mainly due to two factors: first, streak artifacts are observed to be generated by the objects with an elongated shape in-plane. Compared to these absorbers, the vertical structures reconstructed as absolute points in this image, generate lower artifacts due to the spatial averaging properties of the system. Secondly, the arc-shaped artifacts easily noticed on the extremities of the reconstructed 2D slice, are artifacts generated by the backprojection reconstruction, and are discusses in the next section describing the acquisition modalities.
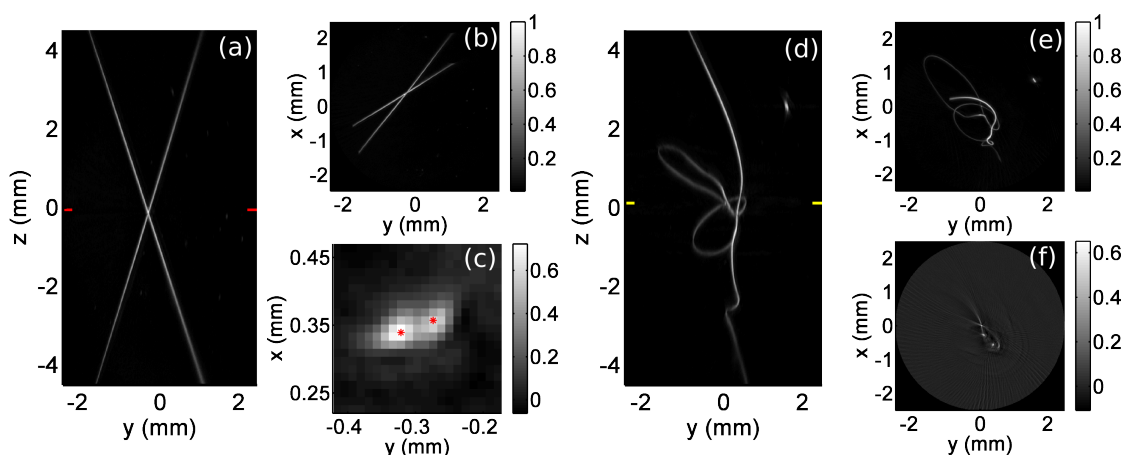
Figure 5.10.: System performance in complex synthetic absorbers. Reconstructions of Phantom 1 [(**a**) to (**c**)] and Phantom 2 [(**d**) to (**f**)], both composed of ⌀ 20 μm threads arranged respectively in a cross and a loose two-loop knot. (**a**) and (**b**) maximum intensity projection (MIP) images respectively along the *x*-axis and the *z*-axis of the first phantom. (**c**) Two-dimensional slice corresponding to the plane marked with superimposed marks on the sides of (**a**). The star markers indicate the position of the maxima corresponding to the reconstruction of each thread. The distance between the two stars is 51 μm. (**d**) and (**e**) MIP images respectively along the x axis and the z axis of the second phantom. (**f**) Slice corresponding to the plane marked with superimposed marks on the sides of (**d**).

5.2.5. Custom scanning the transducer array: scanning procedure

The scanning geometry presented in the previous section was implemented using two different routines: an averaged (termed here **AAM**) and a continuous acquisition mode (**CAM**). Both these scanning routines rely on a rotation range of approximately $180°$ degrees around the sample, combined with a translation of the array matching or even exceeding the radial extent of the sample. The translation range is modular, and it can encompass objects of different sizes, adapting the acquisition time to the application. A schematic of the sensor position during acquisition is presented in *fig.* 5.11.

During the averaged acquisition mode (*fig.* 5.11 **a**), the rotation stage was moved to a total of 120 positions, with an angular step $\theta = 1.5°$ degrees. For each of the angular positions, the array was linearly translate along the tangent to the circle (*fig.* 5.11 **a**) in steps of length equal to $l_a = 2 * l_0$, with l_0 being the width of the focal spot for the 24 MHz transducer (see section 3.3). During this scanning routine, for each of the stationary positions of the probe, a predefined number of recorded signals were averaged and stored in the computer, before moving the array to the next acquisition position. The averaging was performed in order to increase the signal-to-noise ratio and to reduce the electronic noise. For further detailed parameters of the acquisition routine, we refer the reader to Table 5.1.

Table 5.1.: Acquisition parameters - high-frequency linear array

Acquisition Mode	Averaged	Continuous					
		1	2	2.5	3	4	5
Total number of measurement positions	3600	3660	7380	9180	10980	14700	18300
Rotation range		178.5 degrees					
Mean travel of the rotation stage between successive measurement positions (mm)	1.5 deg	2.9′	87.3″	70.2″	58.6″	43.6″	35.1″
Translation range (mm)				9			
Median travel of the translation stage between successive measurement positions (um)	300	296	147	118.5	99	74	59.5
Maximum speed of the array during the acquisitions (mm.s-1)	-	3.0	1.5	1.2	1	0.8	0.6
Total acquisition time (min)	43.3	6.1	12.3	15.3	18.3	24.5	30.5

During the continuous acquisition mode (*fig.* 5.11 **b**), the array was continu-

ously rotated and translated, and for each laser pulse the signals were recorded and stored without performing any averaging. The rotation motion was performed at constant speed, in only one direction, covering the entire predefined angular coverage (black lines originating from the origin point correspond to angular positions at different time points). The translation stage was coded to perform a repetitive oscillatory motion with a predefined speed v_c over a fixed distance. The segment covered by the array in this linear motion was chosen tangent to a circle centered on the axis of rotation. The translation speed for a given range L and a pulse repetition frequency (PRF) of the laser were selected such that the distance covered by the array between two successive laser pulses, $l_c = v_c/PRF$, is a fraction of the translation step performed in the averaged acquisition mode, l_a. In the current study, the minimal fraction was selected such that the total number of positions is equal between AAM and CAM#1. On the other hand, the minimum discretization step during CAM mode was selected to correspond with the same number of laser shots used during the averaged acquisition mode. In *fig.* 5.13 a top view of the sensor positions is plotted for three different translation ranges corresponding to the translation range in the averaged scanning mode (l_a): factor 1 (a) is equivalent to $l_a/1$ and will be referred to as CAM #1, factor 2 (CAM #2) (b) equivalent to $l_a/2$ and factor 5(CAM #5) (c) equivalent to $l_a/5$. *Figure* 5.13 **a-c** shows the same angular coverage, but an increased sampling of in-plane detector positions. For further detailed parameters of the acquisition routine, we refer the reader to Table 5.1.
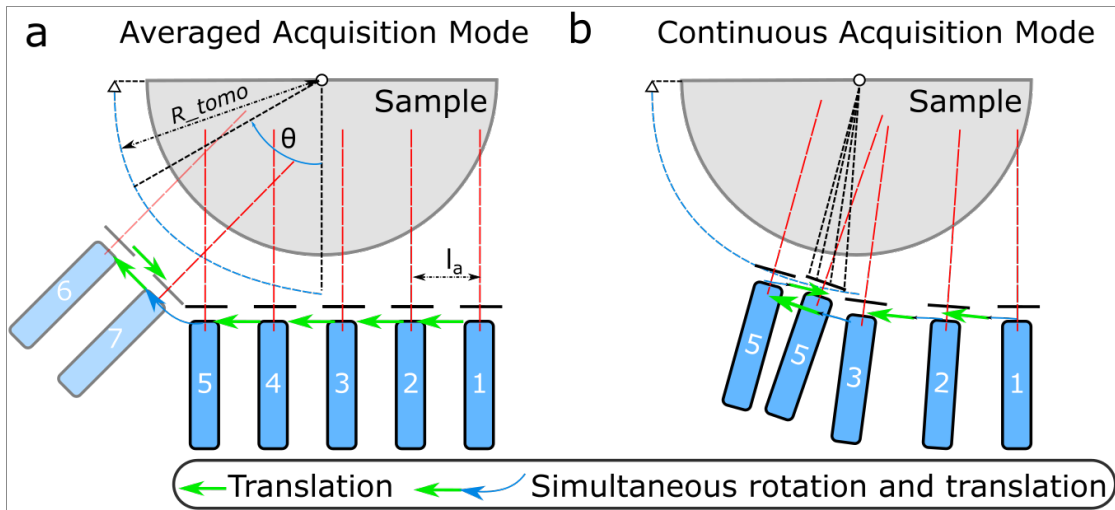

Figure 5.11.: Acquisition routine: (**a**) Averaged Acquisition mode (AAM); (**b**) Continuous Acquisition mode (CAM).

5.2.6. Discreet and continuous acquisition modalities

The performance of the two acquisition routines: averaged acquisition mode (AAM) and continuous acquisition mode (CAM) was compared using a mouse kidney. The sample was scanned first in an averaged acquisition mode and consequently in all CAM modes presented in Table 5.1. In *fig.* 5.12 two different reconstructed slices (slice #1 and slice #2) are presented in AAM mode and CAM #1, CAM #2.5 and CAM #5 mode. It can be observed that the renal artery and the renal vein in slice #1 and the medullary region with the vasa recta in slice #2 are better resolved in CAM #5 compared to the averaged mode. A visual comparison of the image quality between these modes shows that strong arc-shaped streaking artifacts are visible in the averaged mode (full yellow arrow in *fig.* 5.12). On the other hand, by analyzing the continuous mode acquisition, the presence of these artifacts is already reduced in CAM #1, and is completely mitigated in CAM #5. This effect is due to the acquired number of views of the sample: in averaged mode, even if the number of recorded positions is the same as in continuous mode, the number of views is smaller due to the discreet sampling of detector positions. Continuous acquisitions increased the number of views of the sample since the array was constantly moving while keeping the number of single-pulse acquisitions inferior or equal to the average mode.

Even if the streaking artifacts were less visible in any of the continuous modes, several structures like the interlobular vessels (empty arrows in *fig.* 5.12), clearly visible in averaged mode, were not detected by CAM #1 and were hardly resolved in CAM #2.5. To assess the possible reasons, the noise content in the reconstructed datasets was calculated. In *fig.* 5.13 **d**, a plot of the standard deviation of the background noise as a function of data acquisition mode is presented. The standard deviation was computed on $21 * 21 * 21$ voxel cuboids extracted from the volumetric dataset of a kidney recorded using several acquisition modes: CAM #1, CAM #2, CAM #2.5, CAM#4, CAM #5 and AAM. The extracted cuboid location is marked on the slices presented in *fig.* 5.12 with a blue square. In *fig.* 5.13 **c**, the horizontal line corresponds to the value in averaged data acquisition mode. The results are presented in *fig.* 5.13 **c** and show that the background noise level decreases by increasing the number of discretization steps in continuous mode. In comparison to the averaged acquisition mode, the background noise was found 65% stronger in CAM #1, 31% weaker in CAM #5, and only 5% stronger in CAM #2.5. Firstly, these results can indicate that the noise level could be a dominant factor to explain the non-appearance of some interlobular vessels in CAM #1. On the contrary though, the noise level had similar values for the averaged and CAM #2.5, even if in
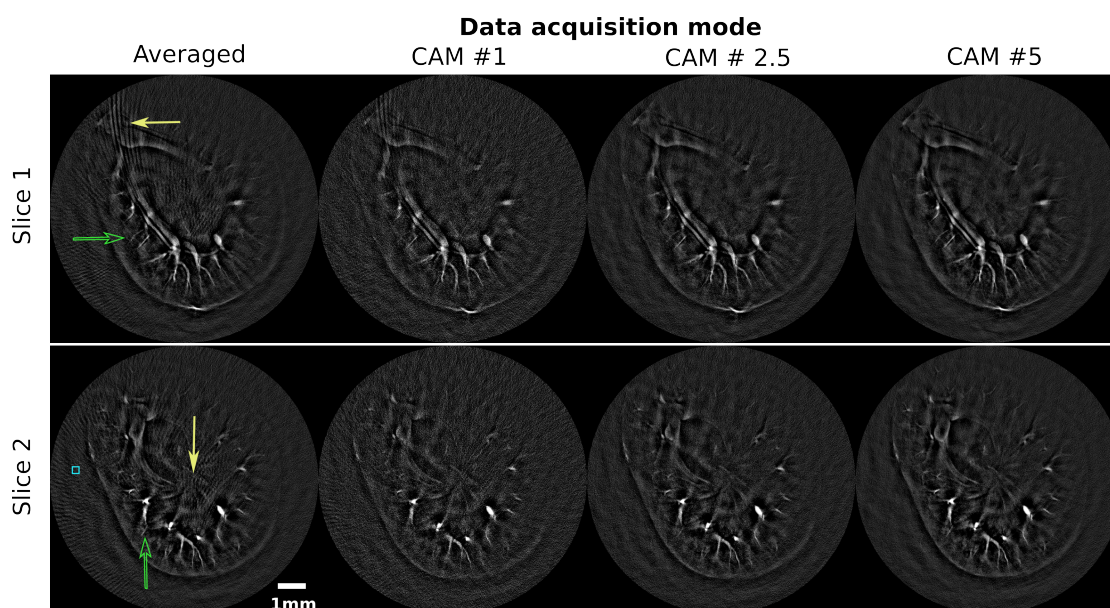
Figure 5.12.: Continuous acquisition routines on mouse kidney. Reconstructions of slices #1 (top row) and #2 (bottom row) of the mouse kidney for several acquisition modes. The full arrows indicate regions where image quality is affected by arc-shaped streaking artifacts in average acquisition mode. The empty arrow points at interlobular vessels; the visibility of these vessels depends on the acquisition mode. The superimposed square indicates the limits of the regions for which the standard deviation of the background noise was assessed.

the latter the number of laser pulses was half the one used in AAM. Based on this results, the noise origin in these datasets is more probably caused by either electronic noise in the CAM modes or the streak artifacts in AAM mode. Regardless of the noise origin, another observation must be made with respect to the contrast of interlobular vessels throughout the acquisition modes: during the CAM modes, an absorbing structure with strong directional patterns will be recorded from more views, but will not have the same contrast intensity as the one recorded by an AAM mode scan.

Overall, the continuous acquisition routines described herein had several advantages over the averaged modes. Achieving a similar level of the background noise, the continuous acquisition mode is drastically reducing the required scanning time from 43.3 minutes to only 15.3 minutes. Furthermore, due to an increased number of views around the sample, the CAM modes mitigate the streaking artifacts present in the AAM modes, and can potentially reduce the background noise at the price of increasing the acquisition time. On the other
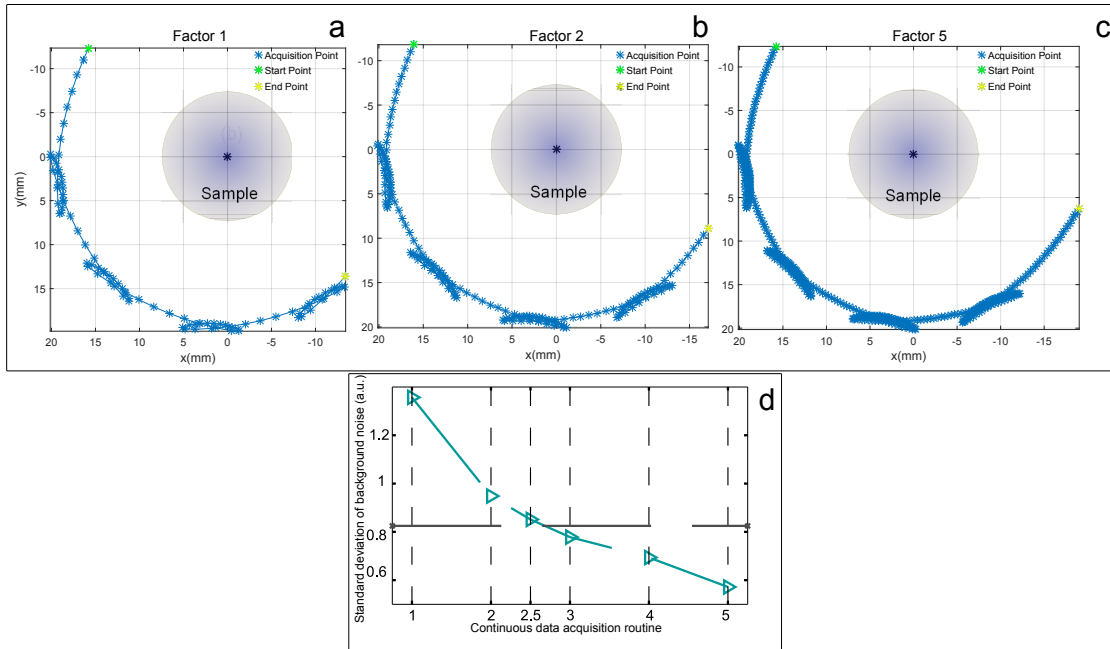
Figure 5.13.: Continuous acquisition routine and comparison of image quality with regard to the number of sampling positions; (**a**) Translation range factor 1; (**b**) Translation range factor 2; (**c**) Translation range factor 5; (**d**) Standard Deviation of the background noise as a function of the number of continuous data acquisition positions on the mouse data-set presented in *fig.* 5.12

hand, the CAM modes, due to the high number of detector positions generate large size tomographic datasets, increasing the computational demands in the reconstruction phase.

Summarizing, the current implementation of the cylindrical geometry had the following properties:

- The system was able to acquire 3D optoacoustic datasets with homogeneous in-plane resolution
- The in-plane resolution depends on the frequency of the transducer used. For the 24 MHz linear array the resolution was determined to be 30 µm micrometers in plane, and 120 µm along the vertical dimension.
- The vertical aperture of the transducer defines the maximum height of the sample that can be imaged, while the focal distance limits the rotation radius (a radius coinciding with the focal distance ensures good sensitivity), and implicitly the sample's diameter.
- The continuous acquisition mode enables reduced scanning time generating

good (noise-to-background) images.

5.3. Anatomical OA imaging in cylindrical configuration

In the current section, the proposed geometry was applied on biological samples, in order to extract anatomical information, ranging from macroscopic level (entire body small animal) to mesoscopic scale (single organ imaging). Two applications using two different linear arrays in consecutive manner are described and the implications of frequency content in the optoacoustic datasets is shortly introduced.

Based on the particular choice of hardware, optoacoustic imaging can resolve structures ranging from macroscopic to microscopic level. The macroscopic optoacoustic imaging uses ultrasound detectors with a center frequency similar to the ones used in clinical use (5 MHz) and achieves resolutions of 100 - 400 µm over several centimeters depth. The mesoscopic scale imaging is achieved by detectors with a central frequency ranging from 10-100 MHz, enabling resolutions of under 100 µm in samples smaller than 1 cm. The microscopic optoacoustic regime achieves sub-millimeter depth with sub-micrometer resolutions.

5.3.1. Low-frequency full-body OA imaging

In the context of the cylindrical implementation of the translate-rotate scanner, by using a transducer array with an adequate focal distance, the entire body of a mouse was imaged. The system used the 6 MHz center frequency array previously introduced in 2.3 and in the table 6.1. The array's aperture on the length axis measures 3.81 centimeters, and coincides with the length of the volume that can be scanned. The limitations in terms of volume that can be imaged, are imposed by the focal distance of the transducer. For the particular implementation using the 6 MHz array, the focal distance was determined to be 19 mm, so the sample that can be encompassed measured a maximum of 38 mm.

An adult female NOD/Scid mouse (Charles River Laboratories, Germany GmbH) was imaged using the 6 MHz array. The mouse was shaved and euthanized. The intact body was then positioned so that its antero-posterior axis follows the *z*-axis with the illumination on its dorsal side around the belly region. The array was translated repetitively on a translation range of 30 mm. *Figure* 5.14 **b** displays two superimposed reconstructions obtained by high-pass filtering (Butterworth filter, order 3) the signals with cutoff frequencies of 100

kHz and 500 kHz respectively. Anatomical features such as large diameter vessels and in particular the bifurcation of the vena cava into the femoral vein can be identified and correlated with published anatomy [113]. Additionally, both kidneys and the spleen could be visualized. The reconstructions also show that with the lower cutoff frequency the visibility of the highly perfused organs such as the kidneys and the spleen is enhanced, whereas smaller structures such as the vessels appear with a better contrast with the higher cutoff frequency. These results indicate that the sub-megahertz frequencies play a role in displaying the background absorption of large structures, and suggest that a composite image displaying multiple high-pass-filter reconstructions could result in a better visualization of the anatomy in optoacoustic images.

For comparison reasons, a full body scan using the optoacoustic system (MSOT 256) introduced in section 3.1 is presented in *fig.* 5.14 **a**. The transducer used in this implementation had a similar center frequency (5 MHz) compared with the L7 array used in the cylindrical implementation. A shaved female NOD/Scid mouse (Charles River Laboratories, Germany GmbH) was scanned *in-vivo*, by translating the animal in $200\,\mu\text{m}$ steps, using 760 nm wavelength optical excitation. For consistency reasons, the data was filtered between 500 kHz and 10 MHz and from 100 kHz and 10 MHz. [1]

The scanning time required by the translate-rotate geometry to acquire a complete dataset at single wavelength using the 6 MHz transducer was 4 minutes, while for the MSOT 256 system, the scanning time required was 7 minutes. In the current implementation the main difference from a biological perspective is that in the translate-rotate geometry, for convenience reasons, the animal was euthanized before acquisition. An *in-vivo* experiment would have been possible by adapting the mouse holder position and by adapting an anesthesia delivering method. In the MSOT 256 implementation, the cross-section images, due to the transducer's specifications and illumination pattern, are severely affected by out-of-plane signal. The out-of-plane signal is considered as the undesirable contribution of optoacoustic waves from adjacent planes to the plane of interest (the plane on which the transducer is focused into; see section 3.1). Moreover, the focusing capabilities of the MSOT256 array enhance the resolution and image quality only in the focal spot while in the translate-rotate geometry, the in-plane resolution is homogeneous throughout the imaging plane (*xy*).

This implementation of the translate-rotate geometry provides several benefits with respect to small animal imaging systems: due to a reduced acquisition time, the volumetric reconstruction of the mouse can encode information about the dynamics of intrinsic or extrinsic contrast agent distribution, without hav-

---

[1]Experimental acquisition performed by Dr. Andreas Bühler

ing to acquire several cross-sections of the animal.
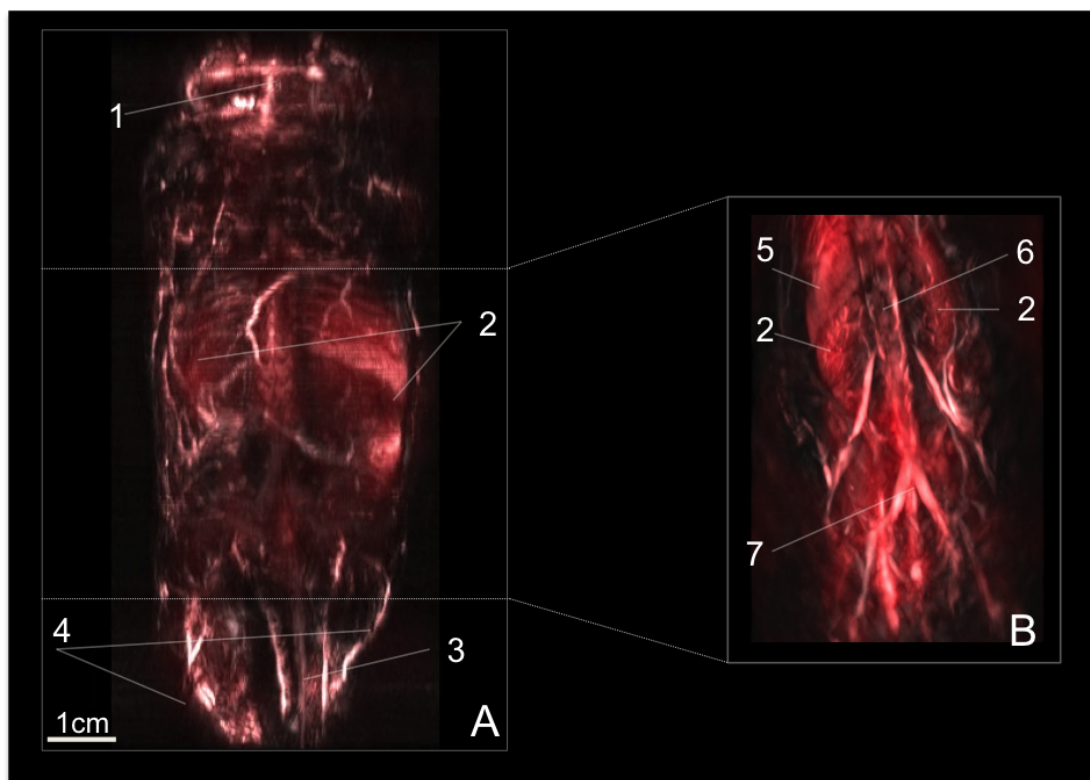
Figure 5.14.: Low-frequency full-body animal imaging; (**a**) Composite frontal maximum intensity projection view of a full body animal imaging scan acquired using an MSOT 256 system with 200 μm scanning step size; overlay of two separate frequency bands: white 500 kHz - 10 MHz and red 100 kHz - 10 MHz ; (**b**) Composite frontal maximum intensity projection (MIP) image from the reconstructions of a tomographic dataset (mouse 1) acquired with the 6 MHz array in the MSOM system, considering high-pass cutoff frequencies of 100 kHz (red) and 500 kHz (white). Legend: 1. Sagittal Sinus 2. Kidneys, 3. Tail, 4. Legs 5. Spleen. 6. Spinal cord region, 7. Bifurcation of the vena cava into femoral veins.

5.3.2. High-frequency OA Imaging of the brain

The mesoscopic scale optoacoustic imaging was enabled by using the 24 MHz linear array, previously introduced in section 2.3 and in the table 6.1, and characterized in the context of the translate-rotate geometry in section 5.2.4. To summarize, we relied on the volumetric capabilities of the system, good xy (30 μm)

and z (120 µm) resolution.

To assess the biological capabilities of mesoscopic imaging in intact sample, a CD1 adult mouse (Charles River Laboratories, Research Models and Services, Germany GmbH) was euthanized, and the brain was excised for imaging. The brain was embedded in turbid agar gel and placed in the imaging system 20 minutes after the animal has been euthanized. The mouse brain was chosen in this study as a biological sample because of the volumetric and complex morphology of the vasculature. Due to the transducer aperture size, a maximum of 1 cm long sample was used.

In *fig.* 5.15 **a**, a photograph of the excised brain before embedding was taken. *Figure* 5.15 **b** depicts a MIP along the *xy*-plane of the reconstructed optoaocustic data-set. Several structures like the cortex, the third ventricle and the cerebellum can be resolved. For validation purposes, a 9.4 Tesla MRI dataset (without contrast agent) of a different animal was used, attaining a theoretical resolution of 60 µm, and the data is presented in *fig.* 5.15 **d** and **e** [2] [3]. In *fig.* 5.15 **e**, a corresponding MIP view of the MRI dataset is presented, and shows good anatomical co-registration between the optoacoustic and MRI image. A 2D cross-section orthogonal to the height axis of the brain was selected (blue dotted line in *fig.* 5.15 a) and the image is presented in *fig.* 5.15 **c**. For anatomical validation, an approximate cross-section from the MRI data-set is displayed in *fig.* 5.15 **f**. In addition to the MRI data-set, two H&E slices are presented in *fig.* 5.15 **f** and **g**, for validation purposes (reproduced from [114]).

Summarizing, the translate-rotate geometry implemented using the 24 MHz linear array shows good performance and comparable results with a 9.4T MRI system, on anatomical and vascular structure identification in the mouse brain. The optoacoustic data-set was recorded on an excised brain in approximately 15 minutes, while the MRI data-set required 65 minutes for the in-vivo scan of the mouse.

---

[2] MRI data acquisition performed by Yuanyuan Jiang
[3] MRI data processing performed by Panagiotis Symvoulidis
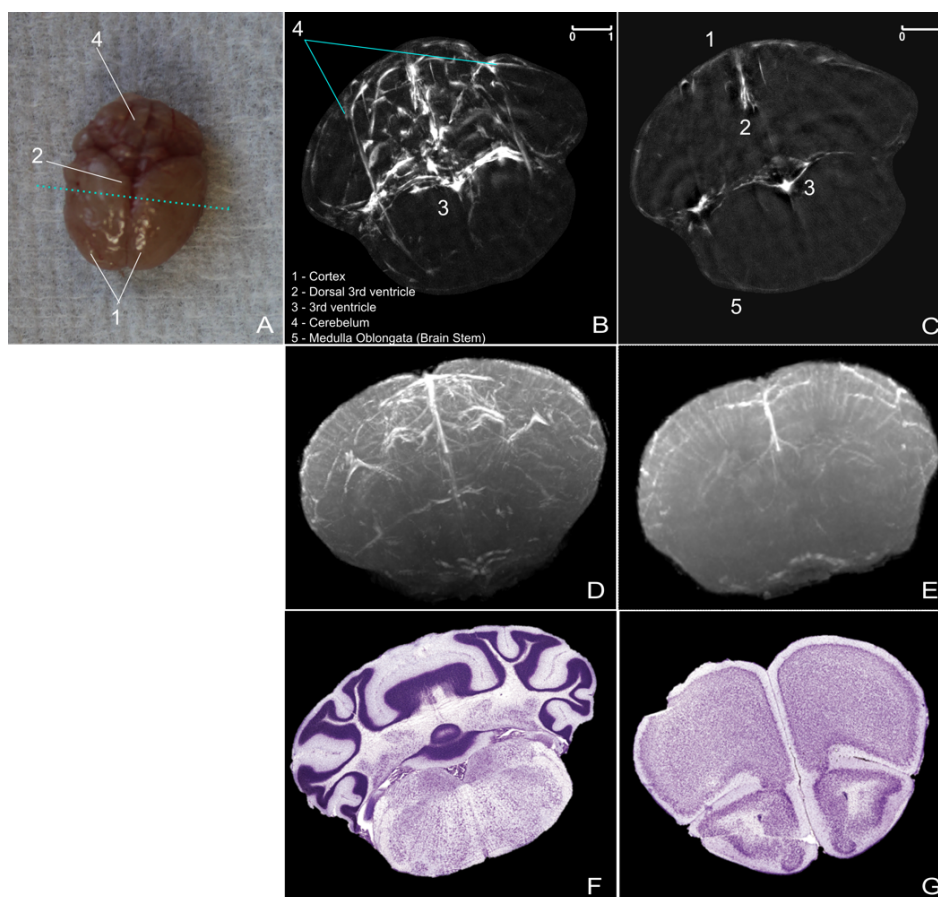
Figure 5.15.: High-frequency optoacoustic imaging of biological sample - Brain; (**a**) Photograph of the scanned sample; (**b**) maximum intensity projection (MIP) of the Optoacoustic data acquired using the high-frequency (24MHz linear array); (**c**) Section plane approximatively corresponding to the 2D plane marked by the blue dotted line in A; (**d**) MIP Image of MRI dataset brain; (**e**) 2D MRI Plane corresponding to the 2D Optoacoustic slice presented in (**c**); (**f**) and (**g**) H&E Histological Images for anatomical validation Legend: 1 - Cortex; 2 - Dorsal 3rd ventricle; 3 - 3rd ventricle; 4 - Cerebelum area; 5 - Medula Oblongata;

5.4. Conclusion

In the current chapter, the translate-rotate geometry was presented, and the implementation of this geometry in a cylindrical manner was demonstrated.

Overall, a cylindrical tomographic implementation in a translate-rotate geometry, provided a large solid angle of detection. The system was used to

record optoacoustic information captured around the sample, and fulfilled the full-view criterion of detection in plane (along the *xy*-plane). By translating the focal spot of the detector for each of the rotation positions, homogeneous in-plane resolution was achieved.

Compared to cross-section geometries, the cylindrical tomographic implementation presented herein reduces the artifacts generated by out-of-plane signals, by recording the acoustic waves using the adjacent elements of the detector. The geometry allows genuine volumetric recording of the pressure waves.

The versatility of the implementation allows using different transducer arrays depending on the application. In the current chapter, the geometry has been implemented with one low-frequency linear array, and full body imaging of small animals had been achieved. Mesoscopic scale imaging has been demonstrated by taking advantage of the high-frequency linear array (24 MHz) to image a samples sized <1 cm with under $30\,\mu m$ resolution.

Intrinsic contrast detection and good vascular network extraction, combined with the continuous acquisition routine opens up the possibility to perform multispectral acquisitions at mesoscopic scale, allowing for molecular activity investigations in small samples at resolutions comparable to MRI.

Chapter 6.

Broadband 3D Optoacoustic imaging at mesoscopic scale: a technical and application study

In the current chapter, the cylindrical detection geometry (see *fig.* 2.3 **b** for clarification) previously presented in chapter 5, is investigated in the context of broadband mesoscopic optoacoustic imaging, using two linear ultrasonic arrays with different center frequency and detection bandwidth. Initial consideration regarding frequency content in OA signals are presented, followed by two particular studies validating assumptions regarding the importance of adequate frequency content recording in mesoscopic scale OA imaging.

Some of the results presented in this chapter are also presented (at places with minimal or no changes) in the publications entitled:

- *"Ultra-wideband three-dimensional optoacoustic tomography"* by Jérôme Gateau, Andrei Chekkoury and Vasilis Ntziachristos, published in Optics Letters, Vol. 38, No. 22, (November 2013)[115]

- *"Optical mesoscopy without the scatter: broadband multispectral optoacoustic mesoscopy"* by Andrei Chekkoury, Jérôme Gateau, Wouter Driessen, Panagiotis Symvoulidis, Nicolas Bèziére, Annette Feuchtinger, Axel Walch, and Vasilis Ntziachristos, published in Biomedical Optics Express, Vol. 6, Issue 9, (July 2015) [15].

6.1. Frequency implications in OA Imaging

In comparison to ultrasound image generation, where a pressure wave is used to generated the acoustic response, in optoacoustic imaging, short laser pulses are directed at the sample, and the absorbed energy causes a local heating, followed by thermoelastic expansion and generation of broadband pressure

waves. The generated pressure waves are therefore broadband, spanning a range from a few kilohertz, up to tens of megahertz. In optoacoustic imaging, different structure sizes and orientations of the absorbing samples will resonate to different frequencies, so the hardware and the detection geometry must be adapted to the sample under observation. From a detection perspective, the centre frequency and bandwidth of a particular detector, will define the range of structures it is able to resolve. As previously described in section 2.3, the ultrasonic transducers have a sensitivity band corresponding to their central frequency, and consequently they act as band-pass filters. In the following section we will address the frequency decomposition from two perspectives: initially, the topic of broadband recorded signals will be regarded from a completely algorithmic perspective, where the possible implications and information extraction will be done on single detector acquired signals. We will address the decomposition of the broad-band signal into separate bandwidths using two different methods, and we will discuss the problem of sound attenuation compensation for OA imaging. In the second part of this chapter, the broadband detection will be described from a hardware perspective, where the proposed solution uses two different transducers to record complementary information generated by the same absorbing structure. After proving the ability of the system on anatomical information extraction, the capabilities of the broad-band hardware implementation will be applied to the molecular imaging problem of detecting exogeneously injected contrast agents in biological samples. A discussion on the capabilities of hardware and software separation of the frequency components will conclude the chapter.

6.1.1. Multiple band frequency separation in OA Imaging

Optoacoustic signals are broadband, and the range of frequencies recorded by the ultrasonic transducer is dependent on the center frequency of the employed hardware and the recording bandwidth specifications of each particular detector. By default, the reconstructed data-sets include the entire information recorded by the detector. Several considerations must be made when reconstructing optoacoustic signals: on one hand, the transducer is much more sensitive in the region around the center frequency. This is of particular importance for coupling the detection geometry with appropriate sample sizes. On the other hand, higher frequencies are much more attenuated compared to low-frequencies (i.e. in biological tissue, a frequency of 25 MHz will be 10 times more attenuated than 1 MHz frequencies [44]). Enhanced attenuation for higher frequencies and reduced amplitude signals generated by small structures will

result in reduced SNR in the reconstructed image. These two main reasons drive
the requirements for optimal selection of detection bandwidth, accurate recon-
struction and separation of the reconstructed signals for optimal representation
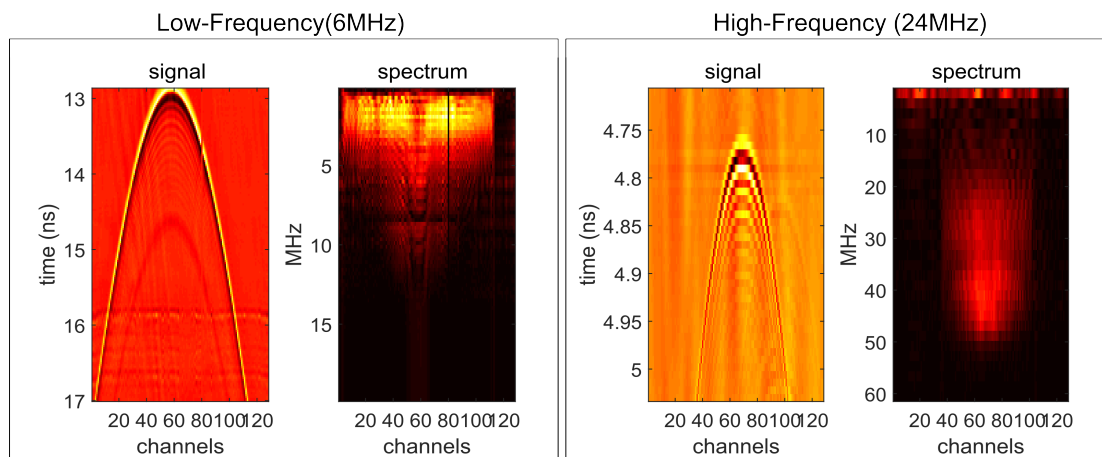of the structures of interest.

Figure 6.1.: Frequency spectrum of optoacoustic signals: The left panel shows an op-
toacoustic signal recorded by the low-frequency array (6 MHz) generated by a $200\,\mu m$
microsphere, and it's corresponding frequency spectrum (right). The right panel shows
the signal recorded by the high-frequency linear array, generated by a $10\,\mu m$ micro-
sphere and the corresponding frequency spectrum.

In *fig.* 6.1 the spectrum of frequencies generated by an absorber with a peak
frequency higher than the maximum detectable frequency [116] of the detectors
are recorded. The left panel of *fig.* 6.1 shows the signal recorded by all the el-
ements of the low-frequency transducer, generated by a $200\,\mu m$ microsphere,
and the corresponding spectrum of frequencies. It can be observed that the
detector can record signals up to 14 MHz, while most of the detection range
is in the lower frequencies (under 6 MHz). On the right panel of *fig.* 6.1, the
same characterization was performed and the signal generated by a $10\,\mu m$ mi-
crosphere is displayed, together with the frequency spectrum, ranging this time
from 10 MHz up to 50 MHz. The presented frequency spectrum of the two
transducers shows that the two transducers record a broadband spectrum of
frequencies. During the reconstruction phase of OA signals, the entire spec-
trum of frequencies is reconstructed at once. Since smaller structures, resonat-
ing at higher frequencies are more attenuated than bigger structures generating
low-frequencies, such a reconstruction modality might probably enhance only a
certain range of structures, hindering the visibility of smaller details. In order to

analyze the content of this frequency spectrum, and the information provided in each of the spectral bands, in the following section two different methods to extract a particular range of the frequency content are presented. The two modalities can be regarded as methods for performing a visual enhancement and optimal extraction of structures of interest: an initial approach will present a separation of the frequency band spectrum in bands containing an approximate equal relative bandwidth, while the other solution will explore the possibility to decompose the signals using a wavelet transform with a variable number of levels. For both suggested methods, the protocol of image generation was the following:

- The acquired signal is corrected for DAQ variations and inversions;
- Depending on the method:

  1. Band-pass filtering of the signals using different low and high cut-off frequencies;

  2. Wavelet decomposition using *db2* wavelets, with 2 or 3 levels of decomposition.

- For each of the bands or wavelet representation of the signals, individual signal reconstruction is performed.

In order to maintain an equal relative bandwidth, in the current a frequency separation is performed based on maintaining a 75% relative bandwidth. This would imply that the different bands of information would translate to a constant resolution increase in the image domain. For the two detectors presented in this work, the broadband spectrum ranging from $2 - 40$ MHz (high-frequency 24 MHz central frequency) and from $0.1 - 12$ MHz (low-frequency 6 MHz central frequency), will be separated in 2 MHz - 8 MHz, 8 MHz - 18 MHz, and 18 MHz- 40 MHz and in 100 kHz - 2 MHz, 2 MHz - 5 MHz, 5 MHz - 12 MHz bands, respectively.

$$B_\% = \frac{f_h - f_l}{f_c} \tag{6.1}$$

where f_h is the high cut-off frequency, f_l is the low cut-off frequency and f_c corresponds to the central frequency of the considered band.

Figure 6.2 shows the maximum intensity projection along the lateral view of a full-body mouse scan performed with the low frequency linear array covering a bandwidth spanning from 0.1 MHz - 12 MHz. This sample was selected for the initial description of the concept, as it includes a broad range of frequencies: from entire organs like the kidneys or the spleen, up to big vasculature like the main artery parallel to the spinal cord, or even smaller vasculature present on

the kidney level. Sub-figures **a** - **c** show the separation according to our concept of constant bandwidth separation. In the 100 kHz - 2 MHz bandwidth, the major vasculature and general shape of bigger structures can be resolved. On the second band, covering the range of 2-5 MHz, only the vascular network is present, without recording any information regarding the major absorbers in the tissue.
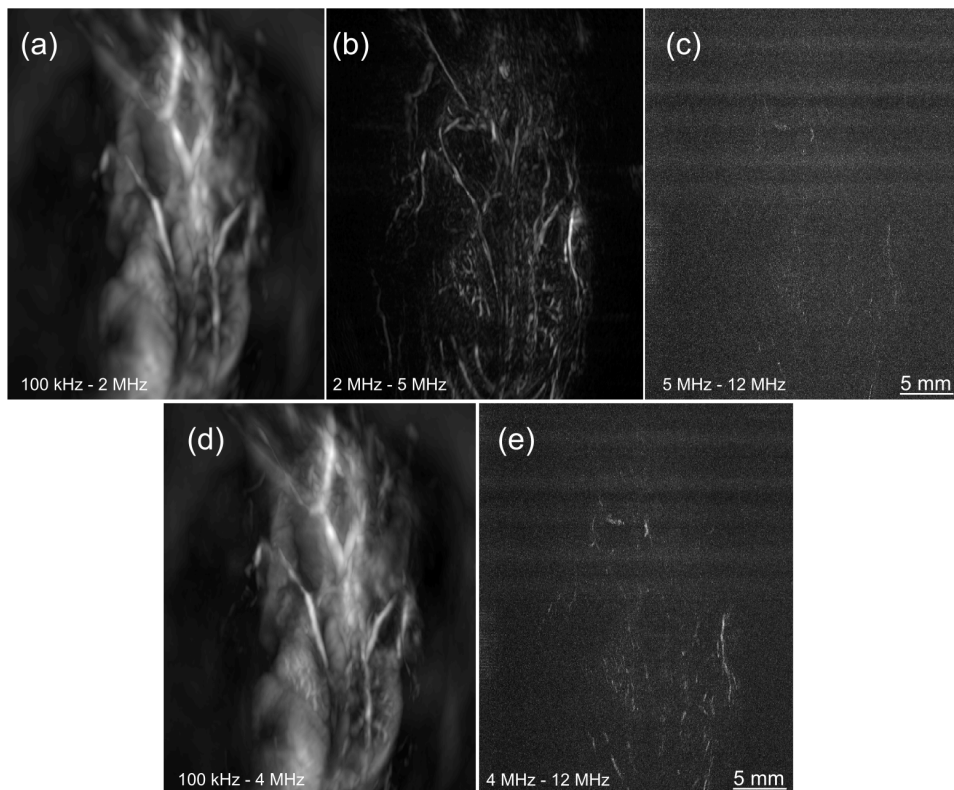
Figure 6.2.: Frequency decomposition in full-body low-frequency optoacoustic images: Maximum amplitude projection (MIP) lateral view of a full body mouse, filtered in between three bands spanning: (**a**) 100 kHz - 2 MHz,(**b**) 2 MHz - 5 MHz, (**c**) 5 MHz - 12 MHz. The same data-set is presented with two different high and low pass filter values: (**d**) 100 kHz - 4 MHz and **e** 4 MHz - 12 MHz.

On the last bandwidth, only very small structures could theoretically be resolved, but due to increased attenuation and reduced sensitivity to high-frequencies, the SNR in the image is considerably reduced compared to the other bands. For comparison purposes, in *fig.* 6.2 **d**, the bandwidth range displayed in sub-figure **a** is extended by an additional 2 MHz, covering from 100 kHz to 4 MHz. The

image shows a higher accuracy in resolving smaller details, and smaller vasculature can be recorded. Sub-figure **d** and **e**, show that by splitting the frequency band in only two different bandwidths: 100 kHz - 4 MHz and 4 MHz - 12 MHz, the overall gain in information provided by this separation is rather poor. Although apparently the conclusion would indicate the fact that the higher frequencies bandwidths are just empty, we consider it more of a problem of sensitivity combined with an attenuation of the signals in the latter bandwidths.

The second method used to separate the frequency content of the recorded signal, involved the use of a wavelet transform. During the wavelet transform, a series of detail and approximation coefficients are calculated, in order to represent the original signal with respect to a mother wavelet. The computation can be performed on further levels, depending on the level of detail required by the application, by performing additional separations of the approximation coefficients found in the first iteration. In the current work, the wavelet decomposition relied on *db2* Daubechies wavelets, implementation provided by Matlab (*wfilters* function in Mathworks 2014).

Figure 6.3 shows the effects of bandwidth separation using the two proposed methods, in a small sample, specifically the mouse kidney. The sample was selected for the increased level of vascularization and particularly for having different sizes of vessels. *Figure* 6.3 top level, shows the separation of three different wavelet levels, while the lower level shows the separation performed on the frequency level. The wavelet decomposition, provides good separation of structures between level 2 and level 3, but does not provide additional information on the first level, while the frequency decomposition separates the outline of the sample (band 1), big vasculature (band 2) and small vasculature (band 3). Overall, the wavelet decomposition shows the most promising approach to separate the different structures in the mouse kidney.

The same sample was scanned using a high-frequency transducer, and the recorded signals underwent the same processing procedure as previously presented. In *fig.* 6.4, the top level shows the wavelet decomposition along the three different levels, while the bottom level shows the frequency band separation. The results indicate that the wavelet decomposition provides information on all levels of decomposition: level 1 outlines the major vasculature and the organ shape, while level 2 and 3 increase the ability of resolving smaller structures. At a frequency decomposition level, the first band (2 - 8 MHz) provides the major description of anatomical structures present in the organ, while the second band (8 - 18 MHz) allows vascular identification. The third bandwidth, 18 - 40 MHz, contains a reduced amount of information, and increased levels of noise.
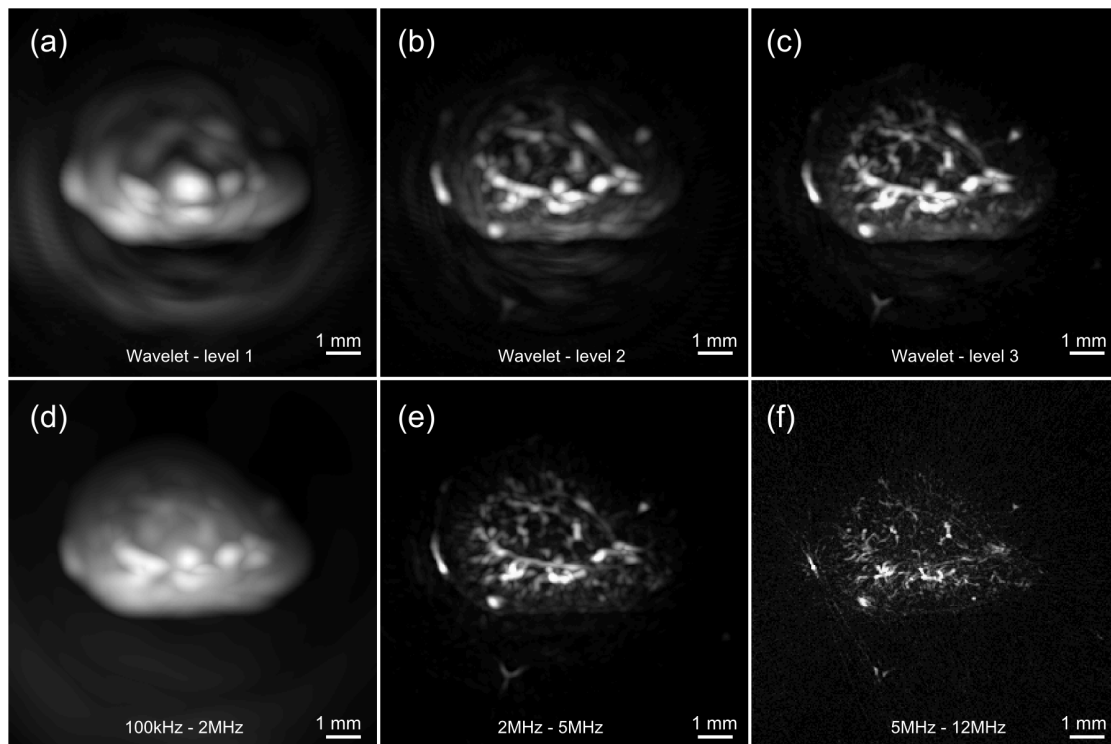
Figure 6.3.: Frequency decomposition at organ level in low-frequency optoacoustic images: Top level (**a**) - (**c**) shows decomposition of the dataset using a db2 wavelet decomposition at three different levels of detail. Lower-level: (**d**)-(**f**) frequency band separation of the signals.

In order to analyze the effects of noise and artifacts introduced by the sharp separation of the frequency bands, in *fig.* 6.5 three different frequency bands are presented: **a** 2 - 8 MHz, **b** 4 - 8 MHz and **c** 8 - 18 MHz. In the second and third bandwidth several structures are observed to be split in smaller repetitive absorbers, in particular the regions presented in **d** and **e** selected for magnification. The same vascular structure present in sub-figure **a** is present and decomposed in sub-figure **b** and **c**, resembling parallel repetitive structures. This effect can be related to sharp variations in signal intensity, which originates from the separation of frequencies in the frequency domain, or from the response of the detector in the time domain. In order to obtain the bands of frequency as previously described, the signals are band-pass filtered in the frequency domain, and can generate the so called Gibbs ringing effect. This effect can be observed in *fig.* 6.5 **b** and **c**, where several structures appear to be repetitive. By analyzing the effects of frequency decomposition at such a small scale ($< 1cm^3$), and
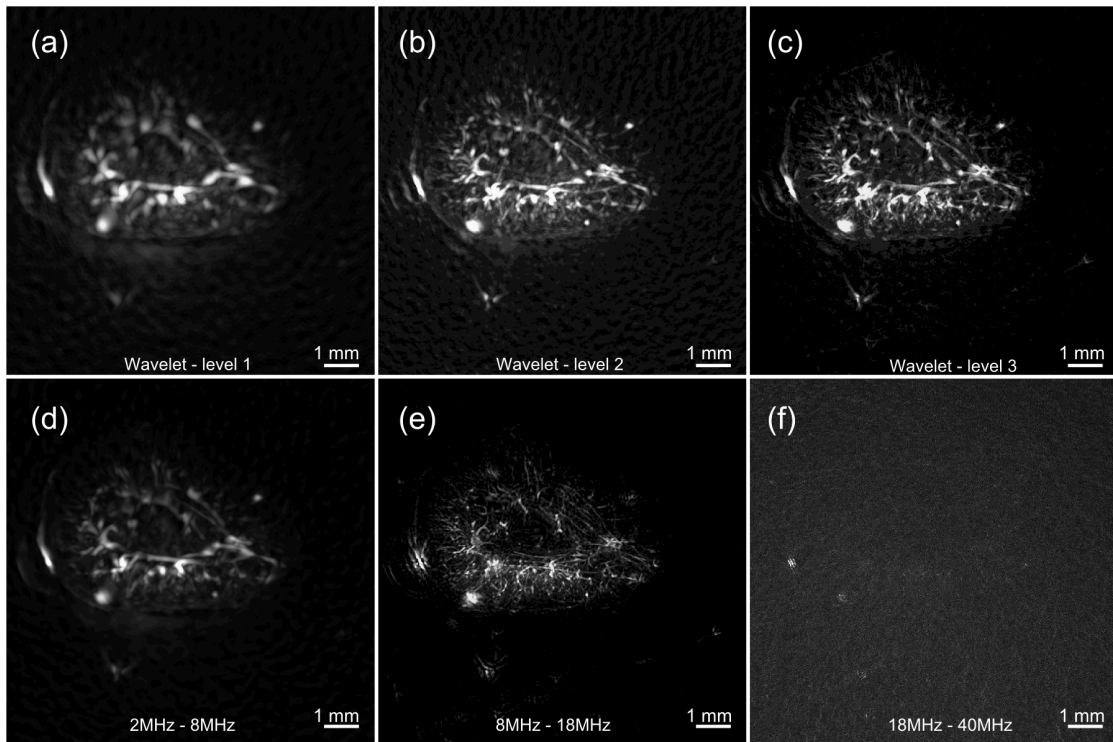
Figure 6.4.: Frequency decomposition at organ level in high-frequency optoacoustic images: top level (**a**) - (**c**) shows decomposition of the dataset using a db2 wavelet decomposition at three different levels of detail. Lower-level: (**d**)-(**f**) frequency band separation of the signals.

this particular detection bandwidth (2 MHz - 40 MHz), we consider appropriate to perform the frequency band decomposition by using either a wavelet transform, or by implementing a complementary detection geometry using different detectors arrays (see section 6.2).

Visualization of information in optoacoustic imaging can prove extremely useful in delineating and highlighting different structures of interest. In *fig. 6.6*, the frequency band decomposition has been performed on a different approach: the high-pass frequency defining the filter was once selected to be 100 kHz and once 500 kHz. By performing this separation, the entire reconstructed bandwidth will be doubled for frequencies above 500 kHz (500 kHz - 12 MHz). Two different colormaps were applied to the so-reconstructed signals, and the resulting outline is displayed in *fig. 6.6* **c**, where the dataset containing higher frequencies is displayed in white, while the background image, the one containing lower frequencies is depicted in red. The same overlaying scheme was
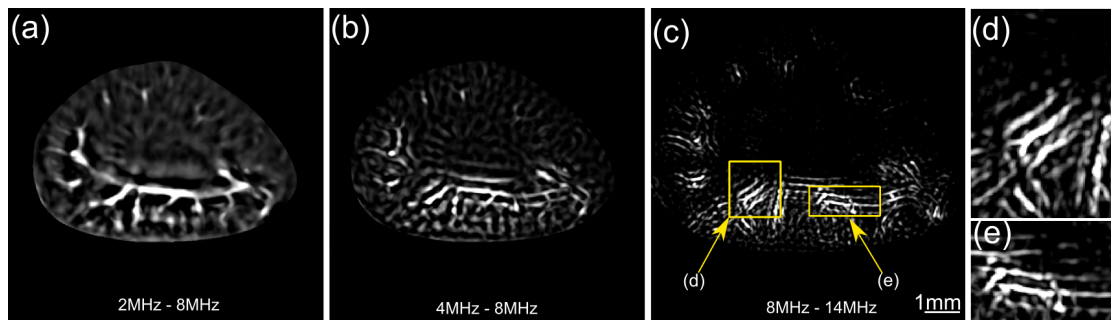
Figure 6.5.: Considerents for effective frequency-band decomposition: Three different frequency band separation of the high-frequency data-set: (**a**) 2 - 8 MHz (**b**) 4 - 8 MHz and (c) 8 - 14 MHz. Artifacts generated by frequency separation are presented in (**d**) and (**e**) for the frequency band spanning 8 - 14 MHz.

applied for a decomposition of the same dataset onto two levels of wavelets (**d** and **e**). The two modalities show similar results on separating and highlighting the vasculature. The frequency decomposition has a more homogeneous aspects, and a less obvious separation effect. On the other hand, the wavelet approach, without requiring the apriori knowledge on the frequency information contained by the signals, separates the dataset into the big-anatomical picture (**d**) and the vascular network (**e**).

The results presented in this section show that indeed, the frequency content recorded by the detectors should be separated in smaller bands, as most usually, high-frequencies are shadowed by low-frequency content. From a methodology point of view, the wavelet decomposition, using a number of $2 - 3$ levels proved to separate and provide more noise-free results. It is important to note, that visualization plays a very important role, and in the current approach a modality applying a low-pass filter with two different bounds, proved to enable much better visualizations of the vascular content, combined with the overall low-frequency information encoding big anatomical structures. Even though the bandwidth separation of optoacoustic signals can be performed by complex algorithms, software implementations can not overcome the limitations imposed by the hardware detection.

6.1.2. Sound attenuation correction in high-frequency OA data

The spatial resolution in optoacoustic imaging is defined as the ability to resolve small structures placed close together. As small structures correspond to short wavelengths and implicitly to high frequencies, ideal detection schemes
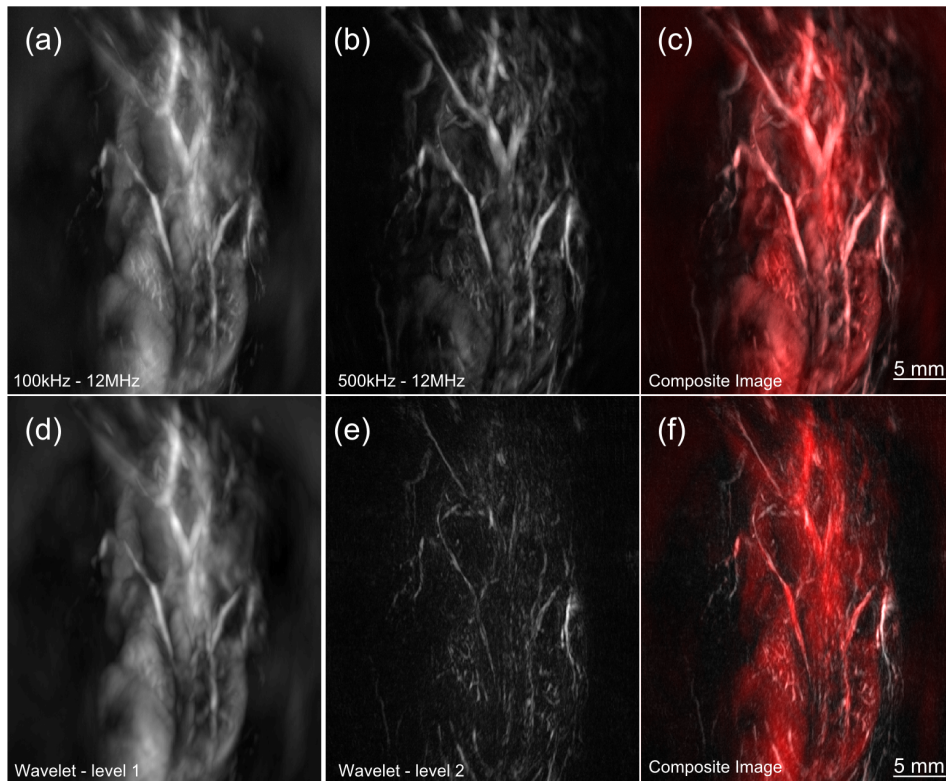
Figure 6.6.: Visualization of frequency band decomposition: Separation performed on a frequency level (**a-c**) and using a wavelet decomposition (**d-f**). (**a**) Frequency band from 100 kHz - 12 MHz (**b**) from 500 kHz - 12 MHz (**c**) Composite image of (**a**) in white and (**b**) in red. Decomposition level 1 (**d**) and level 2 (**e**) and composite image in (**f**).

with increased sensitivity to higher frequencies are required to capture these features. In reality though, the acoustic pressure wave generated after optical excitation is broadband, ranging from a few kilohertz, up to hundreds of megahertz. The ultrasonic detection on the other hand is limited by the acoustic bandwidth of the detector, with increased sensitivity around the center frequency. Overall, recording higher frequencies will be impeded due to increased attenuation and reduced sensitivity of the detectors. This particular characteristic is usually not taken into consideration during the post-processing of the recorded signals, where the entire bandwidth of the signals is considered, without additional care for the high-frequency content of the spectrum.

The effects of acoustic attenuation in optoacoustic imaging were the topic of investigation for previous studies, and have concluded that acoustic attenuation at higher frequencies plays an important role in image quality. It has

been reported, that the acoustic attenuation respects a power law dependence on the frequency [117], and it is more prominent at frequencies above $25 - 30$ MHz. Acoustic attenuation introduces two different alterations in the signal domain: an initial reduction of the wave amplitude recorded by the detector, and a broadening of the acoustic wave, as a result of the different dependence of the frequency on attenuation [44].

So far, several attenuation compensation techniques have been proposed for optoacoustic imaging. In [118] and in [44] the attenuation correction is performed on each of the recorded time signals by using a filter on a fixed distance, without considering the frequency component nor the time information. The filter corrects for features placed at a known distance from the recording positions, which implies that for structures that are before the considered region of interest the signals will be over enhanced, while deeper structures will be under compensated. In [119], a different approach requires solving an integral equation in order to retrieve the un-corrupted signal from the measured attenuated signal.

In the current, we investigate an implementation of the algorithm presented in [43], in order to compensate for sound attenuation in the datasets acquired using the high-frequency linear array. The method relies on creating a time-variant filter, correcting for acoustic attenuation and dispersion of the signals that follow a frequency power law. The resulting filter is applied directly to the time domain signals, and the regularization is achieved using a time-variant window, where the cut-off frequency is based on the local time-frequency distribution of the signals. This implies that the filter is continuously adapting to the frequency content of the recorded signals, reducing the cases where amplification of noise may occur.

Figure 6.7 shows the effects of correcting the recorded datasets using the time-variant filter: in **a**, a maximum intensity profile along the top view of a 3D dataset without any correction is presented. It can be observed the the upper-right quadrant has a different SNR level compared to the lower-left one. *Figure* 6.7 **b** shows the same MIP view of the sample, reconstructed after correcting the time signal for sound attenuation. The results show a clear improvement of the reconstructed volume, particularly in the upper-left quadrant of the image. A zoomed in region of these two quadrants before **c** and after **d** correction are presented. The effects of acoustic attenuation compensation on the OA signals, shows that several small vessels (marked with white arrows) could not be resolved before applying the filter. The blue arrows indicate structures which might be of interest from a biological perspective, representing branchings and separations of the vasculature, which could have not been resolved without the
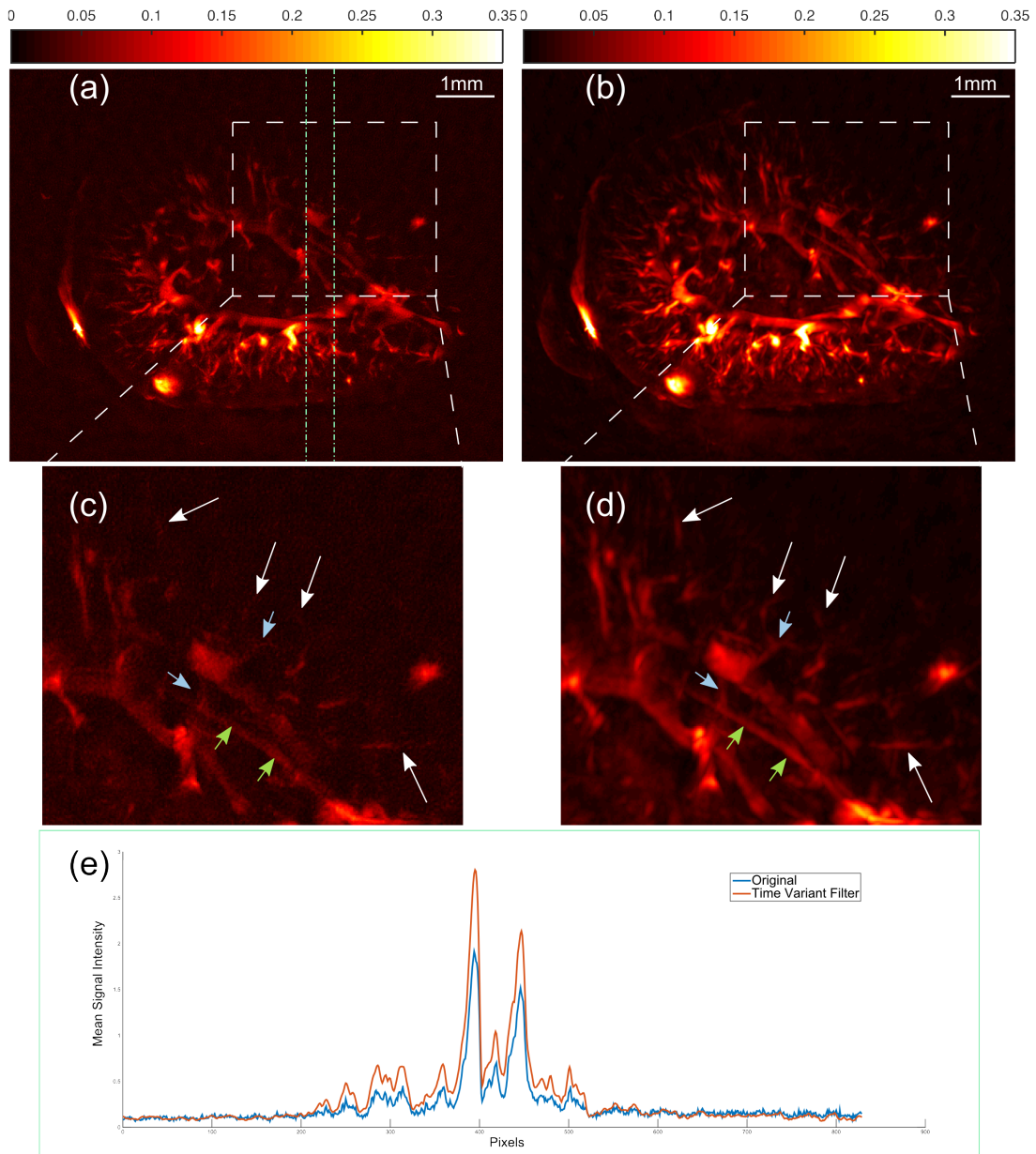
Figure 6.7.: Sound attenuation correction on biological sample; (**a**) MIP view of the mouse kidney without sound attenuation (**b**) MIP view with time-variant filtering. (**c**) and (**d**) zoomed-in panels of the squares marked in (**a**) and (**b**). White arrows indicate structures which are not visible in the non-adjusted data-set. Blue arrows indicate junctions and bifurcations not visible in the original reconstructed volume. Green arrows point at increased contrast post-filtering.(**e**) Mean signal intensity plot along the region highlighted in (**a**) by the green dotted lines: The mean signal intensity in the time-variant data-set (red) is enhanced for structures further away from the transducer (first half of the plot), while the last samples (containing noise) are not amplified.

enhancement of structures provided by the time-variant filter. The third observation regarding the enhancements, relates to a better contrast and continuity of structures: the vessel marked with green arrows appears discontinue and blurred without the proper correction. In order to assess the effects of the time-variant filter, the mean intensity in a region of interest (green dotted lines in **a**) is plotted in fig. 6.7 **e**. The red profile corresponds to the signal intensity in the filtered data-set, while the blue signal corresponds to the un-filtered MIP values.

Overall, the time-variant filtering technique provides a beneficial improvement to the acquired datasets. It can be clearly observed that the method enhances smaller vasculature, corresponding to high-frequency data content, complying to the initial requirements. The reconstructed data-sets appear better-defined, with a more homogeneous distribution of the SNR. For these reasons, the results presented in chapter 7 include a systematic usage of the time-variant filter presented in this section (unless otherwise stated). We note that the data presented in this chapter, was not corrected for acoustic attenuation, and the results show raw reconstructions of the acquired signals.

6.2. Broadband frequency recording in OA imaging - Intrinsic Contrast

In the current section, a hardware implementation recording a broadband spectrum of ultrasonic frequencies is described. The system was implemented using the low-frequency (6 MHz) and the high-frequency (24 MHz) linear arrays in a consecutive manner. The physical characteristics of the arrays were introduced in section 2.3 and the characterization of the system using these two arrays is available in section 5.2.4.

In the current, we investigate the performance of the broadband scanner using the two 128-element arrays. The bandwidths of the two detectors covered from 100 kHz to 12 MHz for the low-frequency array and from 2 MHz to 40 MHz for the high-frequency probe. These specifications resulted in imaging using an ultra-large bandwidth, covering frequencies ranging from 100 kHz to 40 MHz. Through a combination of detector translation and rotation across and around the sample (*fig.* 6.8 **a** and **b**), the scanning geometry implemented herein offers a solid angle of detection fulfilling the in-plane solid angle criterion, being limited in detection aperture by the finite aperture of the arrays in only one dimension. Cylindrical volumes of one centimeter width and height can be accommodated in this scanning geometry with both linear arrays. The acquisition parameters

used in this study are summarized in table 6.1.

Table 6.1.: Acquisition parameters - broadband optoacoustic mesoscopy

	Low-frequency	High-frequency
Center frequency of the transducer	6 MHz	24 MHz
Focal Distance	19 mm	7.5 mm
Translation step	1.5 mm	$300\,\mu m$
Translation Range	10.5 mm	9 mm
Rotation coverage	178.5 degrees	
Rotation step	1.5	
DAQ Specifications	40MS/s	125MS/s

In the current configuration, the two transducer arrays achieved $30\,\mu m$ in plane and $120\,\mu m$ along the vertical axis for the high-frequency probe (section 2.3), and $120\,\mu m$ in plane and $300\,\mu m$ along the vertical axis for the low frequency transducer [71] respectively. The acquisition was performed in averaged acquisition mode (section 5.2.6) using 5 laser shots to record an averaged signal. The required acquisition time for the low frequency scan was 13 minutes and 29 minutes for the high frequency transducer.

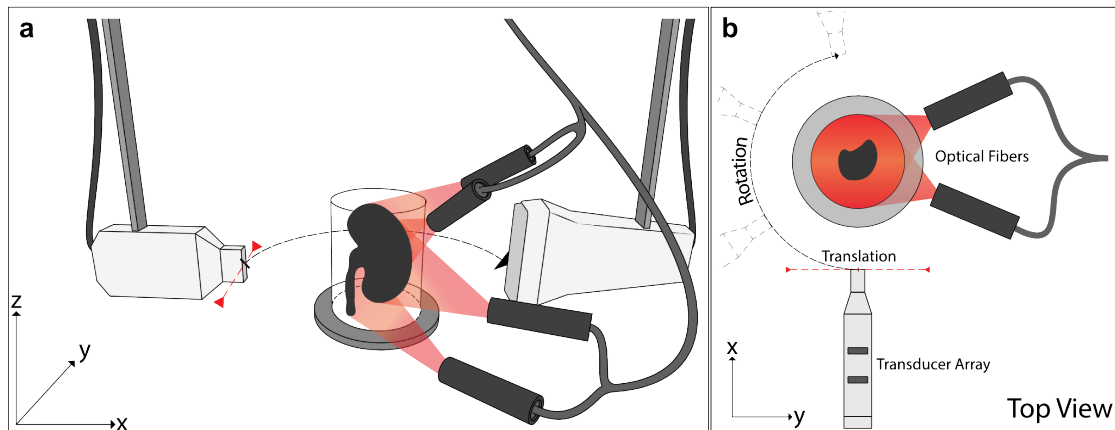**Figure 6.8.:** Experimental set-up; (**a**), Perspective view: The linear transducer array is mounted on the translation stage, which is attached to a rotation stage. The optical fibers are mounted on a supporting holder and the laser beam is directed towards the sample to obtain a homogeneous illumination. For acoustic coupling the sample and ultrasonic transducer were immersed in water; (**b**) Top view of the experimental setup;

The broadband implementation of the translate-rotate tomographic geometry was used to image a mouse kidney, a representative sample containing a broad variety of vessel diameters and orientations, generating a broad range of ultrasonic frequencies.

The excised mouse kidney was embedded in a supporting medium, as described in the section 2.5. The sample was embedded and imaged after animal euthanasia without clearing or perfusing the sample. The illumination was one-sided and the fibers were placed approximately $5\,cm$ from the sample to offer a homogeneous surface illumination. The illumination was fixed and identical during the two scans. For validation purposes, after the tomographic measurements, the sample was frozen, and sliced with a biological microtome cryostat (Leica CM1950, Leica Biosystems Nussloch GmbH, Nussloch, Germany). A red filtered image (630 nm +/- 30 nm) of the sectioned organ was taken after each removal of $45\,\mu m$ thick slices. The colored filter enhances the contrast between blood vessels and surrounding tissues.

The reconstructed datasets are presented in *fig.* 6.9, where two different cross-section slices were selected to show the complementarity of structures that can be recorded by using different detectors. The first slice (*fig.* 6.9 **a-d**) was chosen around the middle plane of the kidney, corresponding to the renal hilum, and is marked with a yellow arrow in *fig.* 6.10 **b** and **c**. *Figure* 6.9 **a-c** show optoacoustic images obtained at low-frequency **a**, high-frequency **b**, and by super-imposing the two images on a composite color channel image **c**. *Figure* 6.9 **d** shows a corresponding photograph of an approximately similar plane taken during the validation procedure. The optoacoustic dataset reveals vascular structures present in the renal cortex (full arrows) which are not visible in the cryoslice image. The empty renal pelvis (marked with an empty arrow) is non absorbing, and no optoacoustic signal is detected in that region. Homogeneous absorption is present in the low-frequency image (*fig.* 6.9 **a**) in the renal cortex, while in the high frequency image this feature is resolved to be the origin of small microvascular structures that can not be resolved by the low-frequency array. The large vasculature like the segmental veins can be resolved by both transducers, but the larger structures, emitting lower frequencies (the renal pelvis and the renal cortex), are not recorded by the high-frequency array. The optoacustic scan reveals several features not visible in the photograph of the sample (*fig.* 6.9 **d**): the interlobular or arcuate vessels or the surface of the cortex, and can potentially reveal new insights on the anatomical structure of the renal circulatory system. By merging the two slices presented in *fig.* 6.9 **a** and **b**, in *fig.* 6.9 **c**, the low-frequency component is depicted on a red colomap, while the white component represents high-frequency structures. The registration process was
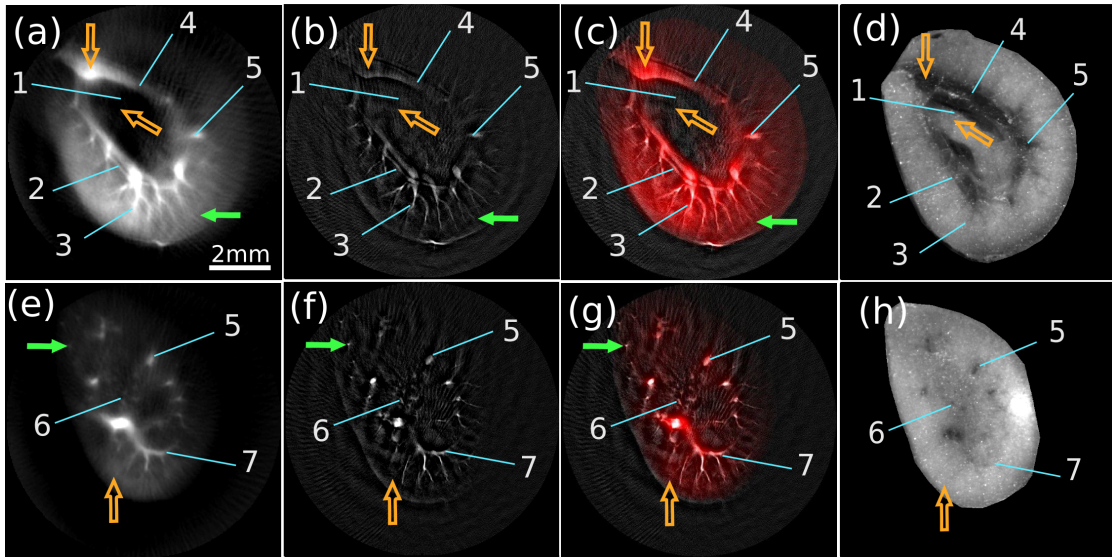
Figure 6.9.: 2D Broadband optoacoustic imaging of the mouse kidney: slice 1 (**a** - **d**) and slice 2 (**e** - **h**). The slices correspond to the yellow markers presented in 6.10 (**b**) and 6.10 (**c**). The slices are presented in increasing z-depth. Reconstructions acquired with the 6 MHz transducer (**a**) and (**e**), and with the 24 MHz transducer (**c**) and (**g**). (**b**) and (**f**) color composite images of (**a**) and (**c**) or (**e**) and (**e**), respectively. (**a**) and (**e**) are displayed in red color scale and (**c**) and (**g**) in gray color scale. (**d**) and (**h**) corresponding re-filtered photographs of the frozen and sectioned kidney. The empty arrows indicate areas specifically visible in images obtained with the 6 MHz array, such as the renal vein, the renal pelvis and the renal cortex. Coverseley, the full arrows indicate microvasculature relvealed in images obtained with the 24 MHz array. Legened: 1. Renal Pelvis; 2. Segmental artery; 3. Interlobular vessels; 4. Segmental vein; 5. Interlobular or arcuate vessels; 6. Medullary pyramid with the vasa recta; 7. Arcuate vessel.

based on the vertical offset of the transducer's apertures and on visual inspection. *Figure* 6.9 **b** enables a visual discrimination between the renal pelvis and the rest of the kidney (empty arrow) and to visualize microvessels in the renal cortex (full arrow) and larger vessels (empty arrow) with similar contrast.

The second slice (*fig.* 6.9 **e** - **h**) was selected in the upper part of the kidney, in the region corresponding to the intersection with the medullary pyramid (yellow line - *fig.* 6.10 **b** and **c**). As with the first slice presented in the top part of the figure, the second slice exhibits a background absorption in the renal cortex visible in *fig.* 6.9 **e** - empty arrow, which is resolved in high-resolution by the high-frequency array as micro-vasculature (*fig.* 6.9 **f**). Moreover, the arcuate and the interlobular vessels are clearly resolved with the 24 MHz array (full

arrow). The vesculature from the vasa recta renis formed of a series of straight capillaries parallel to the height axis of the kidney can be seen in *fig.* 6.9 **e** and **f**. The *fig.* 6.9 **g**, presents the color composite image combining the information content generated by the low-frequency image (red) and the high-frequency image (white). The image shows that the low-content information is responsible to the overall shape of the sample, and the big structures. The high-frequency image records small micro-vasculature present throughout the kidney, complementing the information provided by the low-frequency transducer.
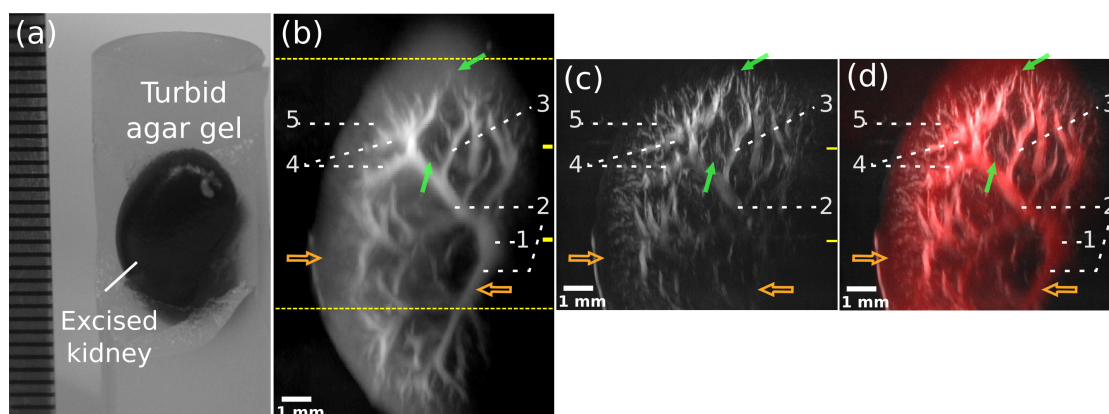

Figure 6.10.: 3D Broadband optoacoustic imaging of the mouse kidney (**a**) Annotated picture of the excited kidney in a turbid agar gel. The upper part of the agar gel was removed to reveal the kidney. A metric steel ruler was placed on the side for size reference. (**b**)-(**d**) MIP images along the x axis from the reconstructions of tomographic datasets acquired with (**b**) the 6 MHz array, (**c**) the 24 MHz array. (**d**) Color composite image of (**b**) in red and (**c**) in gray color scales. The dashed lines on (**b**) indicate the vertical limits of (**c**) and (**d**). The empty arrows indicate regions specifically visible in the image obtained with the 6 MHz array, such as the renal cortex and a segmental vessel. Conversely, the full arrows point out at areas where microvasculature is revealed in the images obtained with the 24 MHz array. The superimposed marks on the side of (**b**) and (**c**) indicate two slices displayed in *fig.* 6.9. Legend: 1. Renal vein; 2. Segmental vessels; 3. Interlobar vessel; 4. Arcuate vessels; 5. Interlobular vessels.

Figure 6.10 **b - d** depict a maximum intensity projection along the lateral view of the kidney. *Figure* 6.10 **b** and **c** illustrate the MIP images along the x-axis corresponding to the acquisition with the 6 MHz array and the 24 MHz array, respectively. In *fig.* 6.10 **b**, the low-frequency acquisition resolves the entire kidney and the slow varying background optical absorption in renal cortex are visible. The branching vessels from the renal vein to the interlobular vessels can be visualized, but only a small amount of vasculature in the renal cortex

could be distinguish in comparison with the published anatomy [17] or with the image obtained using the 24 MHz array (*fig.* 6.10 **c**). A smaller field of view of the same sample is depicted in *fig.* 6.10 **c**, where the 24 MHz linear array was used for acquisition. The height of the field of view is reduced due to the reduced aperture of the array along the z-dimension. *Figure* 6.10 **d** is a merged ultra-wideband image of the low-frequency and of the high-frequency image, showing in good contrast information obtained in both low (empty arrows) and high (full arrows) frequency bands.

To summarize, in the current study we showed that by using different transducers with a sensitivity range dependent on their central frequency, and by registering the obtained results in a visually representative manner, the information content recorded by optoacoustic imaging is increased, and a better understanding of the anatomical structure can be extracted. We highlight that in the present study, the optical excitation was performed at single wavelength, so the main optoacoustic expected contrast was the one generated by vasculature. Moreover, the study did not use the continuous acquisition routine presented in section 5.2.5 as time resolution was not a priority. We also emphasize on the aspect that the murine kidney used in this study was not fixed, cleared or perfused before acquisition. The results presented herein are recorded on the entire sample, in a timely fashion, not allowing tissue degradation. *Figure* 6.9 **c** and **g** demonstrates that combining on individual slices the information on optical absorption gathered in a ultra-wide frequency band enables localization and identification of anatomical features of an intact excised kidney from the renal pelvis and cortex to vessels in a wide range of sizes, and improve the simultaneous visualization of features within a large spatial frequency spectrum. A secondary remark must be made regarding visualization of these optoacoustic datasets: in the MIP views, the bright structures are enhanced at the expense of disregarding the results generated by structures with a lower amplitude. Other effects like the inhomogeneity of light distribution, the partial enclosure of the sample in the current geometry or the frequency dependent sensitivity patterns of the detectors might result in omitting valuable information in the MIP views. For this reason, in the current study and throughout the rest of the thesis, the MIP images will be complemented by cross-section images of the samples, offering a better understanding of the sample's content.

6.3. Broadband frequency recording in multispectral OA imaging - Extrinsic Contrast

In the previous section, results obtained with a translate-rotate geometry implemented in a cylindrical configuration demonstrated the ability to extract anatomical information based on intrinsic optoacoustic signal. The previous optoacoustic method showed to be able to resolve the vascular system of the sample imaged in great detail (i.e. high frequency components). In the current section, we investigated weather this technique is appropriate for retrieving more elaborate patterns of tissues or extrinsic agents in mesoscopic samples.

We present herein broad-band (2B) multispectral optoacoustic mesoscopy (MSOM) based on the tomographic optoacoustic mesoscopy (TOM) principle. 2B-MSOM is an imaging modality that offers the ability to collect three types of frequencies: spatial, optical (spectrum) and ultrasonic. The system operates on the principle of the previously introduced modality: two ultrasonic linear arrays collect spatial frequencies at multiple projections around the sample, leading to accurate three-dimensional imaging. The recorded optoacoustic datasets are rich in ultrasonic frequencies enabled by the use of the dual detectors, covering two overlapping frequency bands at 500 kHz - 12 MHz and 2 MHz - 40 MHz. The third kind of frequencies implemented in the current section is optical. The system used fast-wavelength scanning laser sources to enable tomographic MSOM to resolve specific endogenous and exogenous contrast from tissues, just like fluorescence employed in OPT or SPIM imaging.

6.3.1. Motivation

The goal of this development was to investigate whether the combination of spatial-optical-ultrasound frequency content collected could lead to a modality that in analogy to optical mesoscopy could resolve optical labels in highly opaque media but without the need to chemically clear the specimen imaged. It was expected that the availability of wide-angle tomographic projections could lead to high quality and isotropic in-plane resolution imaging. However the relative imaging characteristics of MSOM versus SPIM were now known, in particular as they relate to resolving not only fluorochromes but also photo-absorbing nanoparticles and the underlying tissue anatomy using label-free, intrinsic contrast. It was hypothesized that the availability of broadband ultrasound frequency could improve upon the limitations of narrow band optoacoustic mesoscopy and reveal not only the vascular pattern common to optoa-

coustic methods but also more generally the lower frequency anatomical appearance of organs and structures that are not typically seen by the state of the art optoacoustic methods. We further hypothesized that such performance would be necessary for identifying elaborate distribution patterns and quantifying the amounts of dyes and particles in tissues.

6.3.2. Contrast agents

In this study, we imaged the biodistribution of two different contrast agents: one organic dye and one type of gold nanoparticles. The first fluorochrome was IRDye 800CW carboxylate (Li-Cor), a near-infrared dye, water soluble, and according to previous studies, rapidly excreted by the kidneys [120]. The second agent used was a formulation of methylated gold nanorod - AuNR (Nanopartz Inc., CO) - a contrast agent proven to stay in the blood flow for long periods of time before being hepatically excreted [9]

Both agents had a peak optical absorption in the near-infrared wavelength range (*fig.* 6.11) and previous studies have proven their suitability for optoacoustic imaging [91][121]. The absorbance spectrum of dyes was recorded using a spectrometer (VIS-NIR; Ocean Optics, Dunedin, FL) prior to injection. Because the contrast agents were expected in structures with various sizes within the kidney, all the samples were systematically scanned using both ultrasound transducers. Optical excitation at different wavelengths (*fig.* 6.11) was used to enable multispectral decomposition. Based on the measured spectra and on previous studies [121] using these contrast agents for optoacoustic imaging, a series of wavelengths on both sides of the peak absorption wavelength were selected in the following sequence for AuNR: 715nm, 740nm, 765nm, 790nm, 815nm and 725nm, 750nm, 774nm, 800nm, 825nm, respectively for IRDye.

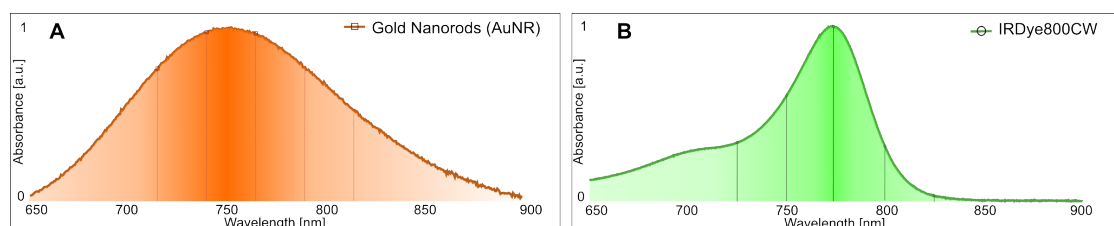**Figure 6.11.:** (**a**) Absorption spectra of the gold nano-particles and (**b**) of the IRDyeCW800; The vertical lines indicate the wavelengths used for optical excitation during optoacoustic acquisition. The spectra were normalized by their maximum value.

6.3.3. Acquisition routine

In the present study, the optoacoustic implementation is similar to the one used
in the previous section, with two different observations: the acquisition routine
used was performed in continuous mode, as described in section 5.2.5. This ac-
quisition routine was preferred based on the performance results presented in
the aforementioned section: good signal to noise ratio, reduced acquisition time,
reducing streaking artifacts. The second difference is the optical excitation: in
the current study, multispectral excitation was performed using an OPO laser
(section 2.2.3) allowing tuning in the near-infrared (NIR) region: $690 - 900$ nm.
Exciting the sample under investigation with different wavelength frequency
enables multispectral decomposition of the spectral signature of intrinsic or ex-
trinsic absorbers.

In the present, due to the capabilities of the hardware employed, multispec-
tral excitation was performed in a consecutive manner: first the laser was tuned
at a particular wavelength and the scan was initiated. Following this procedure,
the next wavelength was selected and the scan repeated. Given the 2B imple-
mentation of this modality, initially a low-frequency (6 MHz) tomographic ac-
quisition was made and repeated for several optical wavelengths after which
the transducer array was replaced by the higher frequency probe (24 MHz) and
the tomographic acquisitions repeated.

The scanner allowed imaging biological samples with resolutions in the order
of hundreds of microns ($130\,\mu$m in plane - i.e. perpendicularly to the z axis- and
$330\,\mu$m in elevation - i.e. along the z axis) using the low-frequency transducer
and higher ($30\,\mu$m in plane and $110\,\mu$m in elevation) by using the high-frequency
ultrasonic probe.

The spatial sampling, the total number of tomographic measurements, and
several other parameters defining the encompassed surface are summarized in
Table 6.2, and grouped according to the center frequency of the array used.

Table 6.2.: Acquisition parameters - broadband multispectral optoacoustic mesoscopy

	6 MHz	24 MHz
Center frequency of the array	6 MHz	24 MHz
Total number of measurement positions	2700	9060
Rotation range (degrees)	178.5	
Translation range (mm)	11	9
Translation speed of the linear stage (mm/s)	4.95	1.18
Rotation speed of the rotation stage (degrees/s)	0.66	0.19
Acquisition time per wavelength (min)	4.5	15.1

6.3.4. Un-mixing algorithms

Spectral un-mixing is the process of detecting, from a series of images obtained at different optical excitation wavelengths, the pixels responsible for generating optoacoustic signal corresponding to a particular absorber. The field of spectral un-mixing is broad, and intense efforts are made to optimize the algorithms in order to include all the physical effects observed in real-life experiments, but a detailed overview is outside the scope of this thesis. We re-direct the interested reader to the following resources describing in detail the available algorithms. In the following, the method of choice for un-mixing the optoacoustic sources from the multispectral data was linear spectral un-mixing, a method assuming known absorption spectra for the compound to be detected.

To summarize the algorithm works as follows: for each pixel from a multispectral data-set the algorithm, the resulting spectrum is fitted to a known given spectrum of an absorber expected to be in the tissue. The spectral components are usually including the exogenous contrast agent, the oxy and deoxy-hemoglobin, and a flat spectrum, accounting for a constant absorber, the background or experimental offsets. The linear fitting is performed using a least squares method applied on the set of linear equations resulting from the multispectral acquisitions (1 equation/wavelength). The initial pressure distribution in optoacoustic images is proportional to local light fluence and to the absorption properties of the tissue.

$$p_0 \propto \phi \mu_a \,, \tag{6.2}$$

where p_p is the initial pressure distribution, ϕ is the fluence and μ_a is the absorption coefficient. For each pixel of an image, the equations used for spectral un-mixing are the following:

$$\phi\mu_a(\lambda_i) = \phi\sum_{j=1}^{N}\epsilon_j(\lambda_i)c_j\,, \qquad\qquad (6.3)$$

where i is the wavelength, $\phi\mu_a(\lambda_i)$ is the optoacoustic response for the pixel, ϵ_j is the absorption coefficient for the absorber j, and c_j is the concentration of the absorber. The least squares method solves the unknowns θc_j, where $j = 1 : N$.

Given $M \in R^{m*n}$ the multispectral measurements matrix, with m the number of single-wavelength images acquired and n the number of image pixels and the absorption spectra of the expected sources, $A \in R^{m*l}$, with l being the number of sources, the problem of linear spectral un-mixing relies on solving the system $M = A * C$ for obtaining the concentration matrix, $C \in R^{l*n}$. In order to avoid generation of non-physical negative concentration values the inversion problem is solved by adding a non-negativity constraint (lsqnonneg - MATLAB R2011b, The MathWorks Inc., Natick, MA, 2011).

6.3.5. Case study 1: Gold Nanoparticles (AuNR)

The kidney corresponding to the mouse injected with the nanoparticle formulation was scanned in the cylindrical configuration following the previously described methodology. *Figure* 6.12 summarizes the results obtained during the 2B-MSOM acquisition. The optoacoustic results are displayed on a gray colormap corresponding to anatomical contrast generated at single wavelength excitation, with a yellow colormap overlay corresponding to the resulting un-mixed agent distribution. *Figure* 6.12 **a** and **b** show maximum intensity projection images along the *xy*-plane of the recorded volume. The yellow overlay corresponds to signals emitted specifically from the gold nanoparticles and reveals an elaborate bio-distribution pattern throughout the images. Both the low frequency and high-frequency images depict a broad distribution of the nanoparticles through the vascular network of the kidney. The low-frequency image shows primarily signals in the thicker vessels, while the higher resolution image - *fig.* 6.12 **a** - confirms the presence of gold nanoparticles in smaller micro-vessels sized down to $30\,\mu$m. A corresponding ultramicroscopy MIP image (*fig.* 6.12 **c**) shows good correspondence of the anatomical information seen on *fig.*6.12 **a** and **b** from approximately the same kidney area as the one shown on *fig.*6.12 **a** and **b**. The network of thin micro-vessels forming the renal cortex can be clearly registered between the three MIP images. The impact of frequency content on the resolved anatomical structures can be seen on *fig.* 6.12 panel 3 and panel 4, where a selected area of the MIP images is presented. The

high-frequency image provides a detailed view of the network of vessels and micro-vessels, resolving smaller structures not present on the low frequency data-set.

Figure 6.12 **d** displays a cross-sectional plane around the medial plane of the kidney generated using the high-frequency transducer. Enhanced resolution and structure delineation reveal several anatomical structures like the medullary pyramid or the microvasculature forming the renal cortex, which are not resolved by the low-frequency transducer (*fig.* 6.12 **e**). In the low-frequency image (*fig.* 6.12 **e**), agent detection in the renal cortex is highlighted in yellow due to the dense microvasculature in this area. The presence of gold nanoparticles in vessels larger than capillaries, such as interlobular and arcuate vessels, is visible in the high-frequency image, where these specific structures are resolved. *Figure* 6.12 **f**, shows an ultramicroscopy planar view of a cross section of the kidney, corresponding to the closest visually selected corresponding plane. The image validates the anatomical information obtained using the broadband detection system used during the optoacoustic acquisition, but does not contain any functional information regarding the nanoparticle distribution, implying an MSOM contrast superiority. *Figure* 6.12 panel 2 shows the result of a dark field microscopy scan performed on the region of interest marked by box 2 shown on *fig.* 6.12 **d**, confirming the presence of the nanoparticles in the vascular network. Moreover, *fig.* 6.12 panels 5 and 6 present CD31 and H&E stained slices obtained from a region of interest in a 2D slice, showing the kidney morphology and microvascular pattern.

Figure 6.12 **g** shows the result of a secondary cross-section through the kidney, where the high-frequency optoacoustic scan reveals several anatomical structures, i.e. the segmental vessel, the microvasculature forming the renal pyramids and the empty renal pelvis. The anatomical image is complemented by the molecular information, depicted in the superimposed yellow colormap, showing a different pattern of nano-particle distribution compared to *fig.* 6.12 **d**. The corresponding low-frequency result of the same cross-section as in *fig.* 6.12 **g** is presented in *fig.* 6.12 **h**. *Figure* 6.12 - panel 1 is a dark-field microscopy image that validates the presence of gold nanoparticle on a region of the renal cortex indicated on *fig.* 6.12 **g** by box 1. This result confirms the distribution of gold nanorods in the fine structures of the renal cortex. *Figure* 6.12 **i** the corresponding ultra-microscopy image confirms the MSOM results. Interestingly, the anatomical structures revealed by ultramicroscopy are better captured by the low-resolution (low frequency band) MSOM image in *fig.* 6.12 **h**.
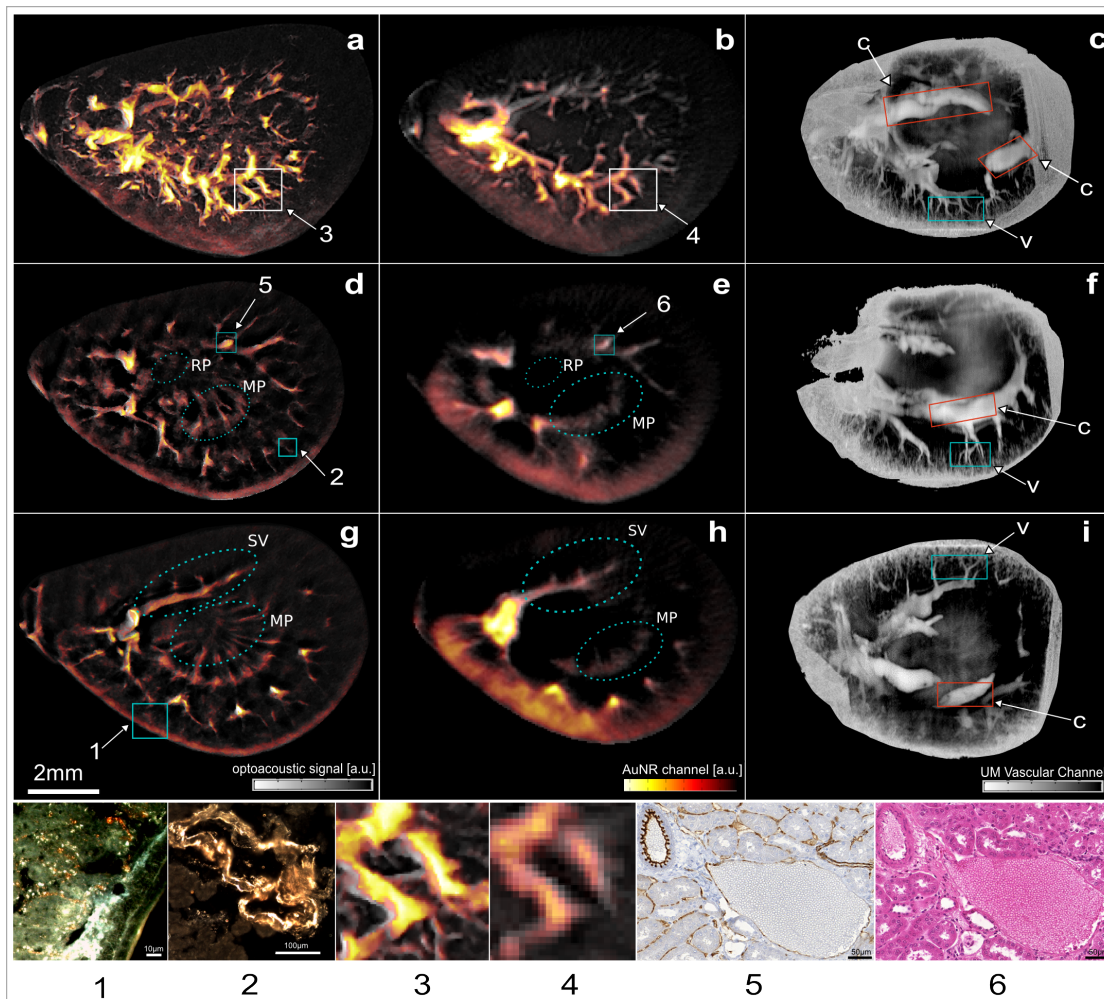
Figure 6.12.: Ultra-wideband Multispectral Optoacoustic Mesoscopy of Gold Nanorod detection in murine kidney - mouse #1. Spectral un-mixed images for the gold nanorods are overlaid in yellow on a single wavelength image acquired at 765 nm (gray). Maximum amplitude projection (MIP) optoacoustic images along the z-axis respectively for (**a**), the 24-MHz array and (**b**), the 6 MHz array. (**c**) MIP ultramicroscopy image of the optically cleared sample; (**d**) and (**e**), optoacoustic images corresponding to the in-plane slice at z = 0.7 mm respectively for the 24 MHz array and the 6 MHz array; (**f**) Ultramicroscopy slice corresponding to a similar plane; (**g**) and (**h**), optoacoustic images corresponding to the in-plane slice at z = 1.4 mm and (**i**) Ultramicroscopy approximately corresponding plane; (1) Dark-field Microscopy images corresponding to a region in the renal cortex and to a blood vessel (2); (3) Magnified view of an optoacoustic image region at high-frequency and at (4) low-frequency; (5) DAB and CD31 staining of an artery and a vein, and (6) H&E Staining of the same region. RP - Renal Pelvis; SV - Segmental Vessel; MP - Medullary Pyramid; c - calyx; v - vessel.

6.3.6. Case study 2: IRDye CW800

In the current section, to investigate whether a different expected distribution patter could be detected by the 2B-MSOM, we have injected a fluorescent dye - IRDye 800CW, before excising and imaging the mouse kidney. The IRDye 800CW is a common type of fluorochrome frequently used in optoacoustic imaging, SPIM or OPT.

Three dimensional tomographic datasets were recorded, and the broadband imaging results are shown in *fig.* 6.13. The IRDye 800CW is known to clear through the kidney within minutes after injection, by accumulating in the renal pelvis before excretion [9]. *Figure* 6.13 **a** depicts a high-frequency 2D cross sectional optoacoustic image at single optical wavelength (774 nm). The green overlay on *fig.* 6.13 **a** indicates the result of un-mixing the absorption spectrum of the organic dye based on the lower frequency contributions. Due to the larger size of the fluorescence lesion, there are no significant high-frequency components generated. In other words, the high-frequency images could not capture any fluorescence bio-distribution, since the fluorescence area established in the kidney emits only low frequency ultrasound signals (in the 500 kHz - 2 MHz region) not captured by the high-frequency detector. Correspondingly no high-frequency unmixed signals are shown herein. This combination of broadband MSOM spectral data validates our original hypothesis that accurate imaging requires 2B-MSOM. *Figure* 6.13 **b** is a corresponding cryoslice image. The color image is a photograph of a kidney cross-section, obtained by physically slicing though the kidney and placing it under a camera. The green signal shown on *fig.* 6.13 **b** is the superposition of fluorescence as seen through a fluorescence filter, showcasing the presence of the fluorescence dye solely in the renal pelvis of the kidney. *Figure* 6.13 **b** is an invasive image that validates the finding in *fig.* 6.13 **a** and confirms that it is only through broadband detection that a complete picture of the underlying bio-distribution is possible by MSOM. This result strengthens the hypothesis that multi-scale detection is crucial for accurate bio-distribution analysis, especially if target-sizes change over time, a common scenario for many injected agents.

Figure 6.13 **c** shows MIP optoacoustic images, relying on contrast generated by absorbing hemoglobin obtained at an excitation wavelength of 774 nm. The image depicts a lateral view of the kidney, where a clear visualization of vascular networks is possible. *Figure* 6.13 **d** shows a side view MIP optoacoustic image of the volumetric reconstruction obtained using the low-frequency transducer. Several anatomical structures can be localized in the low and high frequency MIP images, but a more detailed visualization of endogenous contrast

is possible in the higher resolution image. For anatomical validation purposes a supplementary fresh sample was sliced in thin slices (20 μm), and the MIP image of the reconstructed volume is presented in *fig.* 6.13 **e**. The difference between the exact shapes on the optoacoustic and cryosection MIP images can be attributed to the different orientation of the kidney. Due to the difference in aperture size of the two transducers shown, the field of view of the high-frequency transducer is smaller, as indicated by the dotted yellow line in *fig.* 6.13 **d** and **e**.
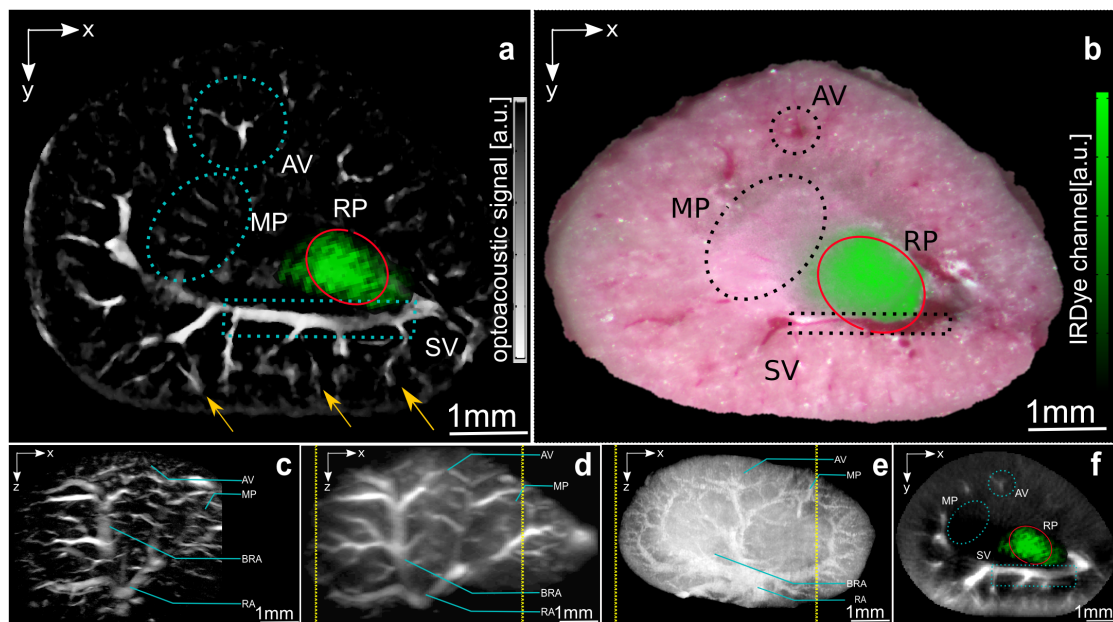

Figure 6.13.: Ultra-wideband Multispectral Optoacoustic Mesoscopy of Organic Dye in murine kidney - mouse #2. The optoacoustic images correspond to the peak absorption wavelength of the injected dye (774 nm), and are displayed in a gray scale colormap. (**a**) IRDye 800CW detection (green) overlay on a high-frequency 2D plane; the agent detection was based on the scan performed using the low-frequency transducer. (**b**) Corresponding cryosection photographs and fluorescence signal detection of the agent (green); (**c**) High-frequency, (**d**) low frequency and (**e**) Cryosection MIP image along y-axis f, 2D low-frequency plane corresponding to the plane presented in **a**; AV - Arcuate vein; MP - Medullary Pyramid; BRA - Branching of Renal Artery; RA - Renal Artery.

6.3.7. Frequency dependent compartmental study of agent distribution

The elaborate patterns revealed by MSOM allow the understanding of distribution patterns in different sub-structures of the kidney. This is an important determinant of the characteristics of different agent studies. One elaborate feature of the MSOM signal is that different substructures generate different frequencies depending on their size. We therefore undertook a study where we looked in a frequency dependent manner on the relative contributions of the agents examined.
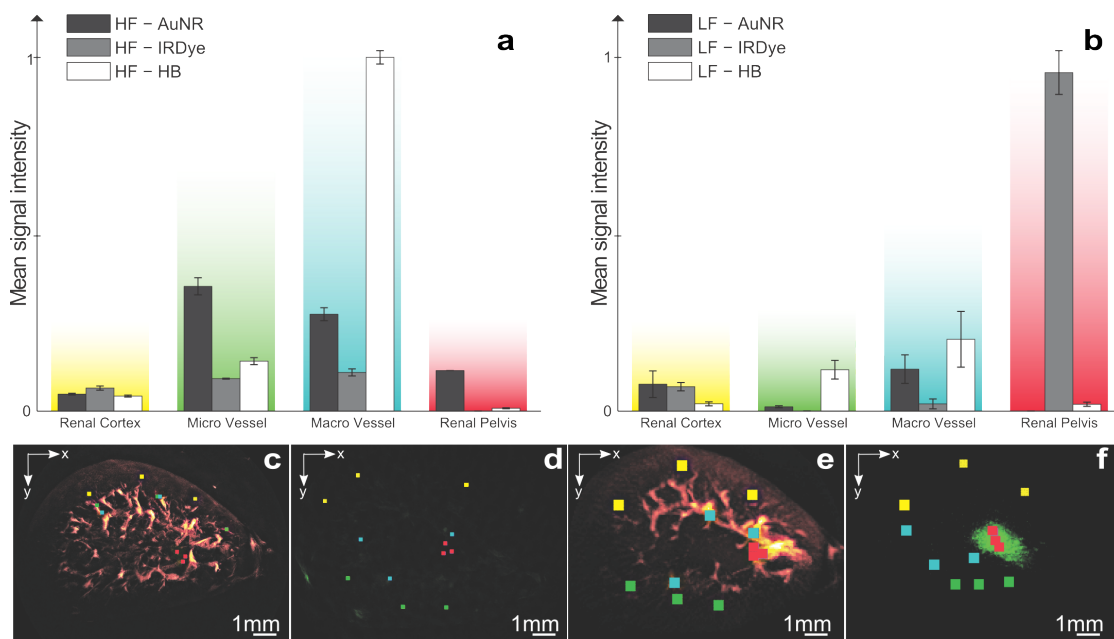

Figure 6.14.: Compartmental study of agent distribution for different frequency bands. Mean signal amplitude for 4 regions of interest selected in high frequency (**a**), and low-frequency (**b**), data-sets; (**c**) and (**d**), Regions of interest selected for the high frequency analysis; (**e**) and (**f**), Regions selected for the low frequency analysis. Seed points for region selection overlaid on the color images: red - Renal Pelvis; yellow - renal cortex; blue - macro-vasculature; green - micro-vasculature

To achieve this we defined $3 * 3 * 3$ voxel sub-volumes selected within different anatomical regions in the reconstructed kidneys. *Figure* 6.14 summarizes the analysis and relative contributions for the AuNR and the IRDye 800CW fluorescent dye in the four selected compartments, i.e. the renal cortex, the renal pelvis, in macrovessels and in microvessels. *Figure* 6.14 **a** depicts the results of the anal-

ysis for the high-frequency component (2 - 40 MHz). Signal generated by AuNR is majorly detected in the macro and microvasculature, with higher preference for smaller vessels. The nanoparticles do not exhibit significant contributions from the renal cortex, or the renal pelvis. Correspondingly, a small fraction of the IRDye is found in the vasculature. Finally, *fig.* 6.14 **a** also shows the compartmental contributions of the total hemoglobin, representing the blood component in the volume of interest, and shows good agreement with physiological expectations of blood pool presence in the renal vasculature. *Figure* 6.14 **b** correspondingly shows the analysis for low frequency components (500 kHz - 12 MHz). In this view, AuNR presence in the renal cortex as well as in both macro- and microscopic blood vessels is shown. The analysis also shows the lack of AuNR retention in the renal pelvis. Conversely a strong contribution from the IRDye is observed in the renal pelvis. Hemoglobin is similarly confirmed in the vasculature. *Figure* 6.14 **c**, **d** show the regions of interest selected in the high-frequency analysis and *fig.* 6.14 **e** - **f** show the regions of interest selected in the low-frequency analysis. The results herein clearly show that the implementation frequency of an MSOM system will affect the quantification of the technique; assigning different values to different compartments. This conclusion further justifies the selection of ultra-wideband MSOM for accurate quantification of different distribution patterns.

6.3.8. Discussion

2B-MSOM was shown also capable of retrieving elaborate tissue anatomy. High-frequency 2B-MSOM images resolved small blood vessels such as the arcuate and interlobular vessels (*fig.* 6.13 **a** - yellow arrows), which are not visible in lower frequencies *fig.* 6.13 **f**. Although the ability of optoacoustic imaging to resolve blood vessels has been well demonstrated , the results presented in the current study show that the information contained in the lower frequency part of the 2B-MSOM data set provided insights to larger anatomical structures that would have been missed by a narrower band implementation. For example, larger structures such as large vessels, the kidney wall or distributed pools of fluorescence accumulation can only be seen in the lower-frequency band as seen in *fig.* 6.12 **e** or *fig.* 6.13 **a**.

Compared to SPIM or OPT, 2B-MSOM could enable imaging of opaque specimen and/or large specimen (in the $1 - 5$ mm range) without the need for chemical treatment. To understand the relevance to SPIM, 2B-MSOM results were contrasted herein to ultramicroscopy images, effectively implementing SPIM of cleared specimen. The comparison between optoacoustic images on

untreated specimen and SPIM images of chemically cleared specimen showcased a congruence of anatomical (absorption) intrinsic tissue contrast. Moreover, 2B-MSOM could resolve not only fluorochromes but also nanoparticles. In addition, although *ex-vivo* imaging has shown so far possible, a next step would be to enable the 2B-MSOM system for *in-vivo* imaging, further improving the application field of this method. Regardless, basic features of the 2B-MSOM ability demonstrated herein, herald a potent outlook. Compared to previous optoacoustic mesoscopy implementations, 2B-MSOM demonstrated significant imaging improvements. Single detector implementation at 15 MHz [27] only captured an approximately 7 MHz spectral band (11 - 18 MHz) at a significantly lower spatial-frequency range. The overall imaging ability of this original 15 MHz implementation suffered from insufficient aperture along the coronal dimension, lower resolution than the 2B-MSOM system and formed only single - plane two-dimensional images. It was the particular implementation of an extended frequency range (0.5 - 40 MHz) and the use of a high-spatial-frequency pattern employing 128-detectors in parallel, which enabled true three-dimensional operation, yielding accurate imaging performance. The use of multiple ultrasonic transducers to record a broadband spectrum has been previously considered in single-element scan investigations aimed at comparing the contrast and resolution improvements at single-wavelength optical excitation [122]. Therefore, the relation between bandwidth and dye bio-distribution could not be established in these studies. Moreover, it was not possible to relate bandwidth to high-spatial sampling, three-dimensional tomographic images. Other detection technologies using optical intereferometry [63] benefit from a large detection bandwidth [123]. These implementations are limited to planar raster-scan geometries possibly introducing limited view artifacts. Compared to previously reported raster scan approaches [67, 124], 2B-MSOM demonstrated high and homogeneous in-plane resolution, three-dimensional imaging capacity, the ability to resolve contrast beyond blood vessels and high-frequency structures and the ability to resolve nanoparticle and fluorescence bio-distribution at resolutions better than 30 microns through at least 3 mm of tissues. No optoacoustic method has achieved such performance so far. The investigation herein considered imaging of agents of varying molecular weight, i.e. low molecular weight organic compounds and gold nanoparticles exhibiting markedly different bio-distribution patterns but near-infrared absorption, to enable low light attenuation in tissue. Specific detection of the injected particles was achieved using spectral un-mixing [125], which identified the injected agents based on their absorption spectrum; revealing functional information, which was then superimposed on anatomical/vascular features of the kidney.

The un-mixing method accurately resolved the different patterns of the photo-absorbing agents used. High-spatial-resolution patterns were revealed for the gold particles, corresponding to high ultrasound frequencies and low spatial resolution (larger area) patterns for fluorochrome accumulation, corresponding to lower ultrasound frequency. An important factor in biomarker detection is the number of wavelengths used for optical excitation. Based on the absorption spectra of the injected dye, we choose a selection of 5 wavelengths for each of the injected probes: for AuNR - 715nm, 740nm, 765nm, 790nm, 815nm; and for IRDye - 725nm, 750nm, 774nm, 800nm, 825nm; this selection can discriminate in an optimal and stable manner the three components that we have assumed to account for the optoacoustic signal: the blood component (composed of oxygenated and deoxygenated hemoglobin) and the injected agent. A larger variety of wavelengths could be selected for allowing un-mixing of multiple agents.

Another important factor accounting for image quality and for the detection of the injected agent especially in small and directive structures as blood vessels is the number of projections used during the acquisition. Typical acquisition scans acquired 9060 laser shots*128 elements = 1.159.680 projections over 180 degrees and 9 mm translation range for the 24 MHz scan and 2700 laser shots*128 elements = 345.600 projections for the 6 MHz. The high spatial frequency sampling herein was necessary to offer high-quality images of structural, functional and molecular information. Reducing the number of projections could reduce the acquisition time but also increase image noise and artifacts. One approach to improve imaging performance at limited spatial sampling scenarios is to utilize improved reconstruction schemes that model the spatio-temporal response of the detector and of the geometry implemented and in particular account for the acoustic lens of the detector. Such reconstruction schemes have been shown to provide better image quality with less projections [126]. A limitation of the current study was imposed by the low repetition rate (10 Hz) of the pulsed laser employed for optical excitation, which yielded acquisition times of aprox. 15 minutes per wavelength for the high-frequency transducer and aprox. 5 minutes for the low-frequency transducer. Using 100 Hz lasers instead could accelerate acquisition to less than two minutes of imaging time; plus the time required for specimen or system rotation and translation.

In the context of kidney imaging, several studies concerning renal vasculature, filtration and glomeruli count have revealed a relation between kidney pathology and diseases of the cardiovascular system [127]. Kidney imaging has been analyzed for an accurate assessment of the arrangement of intra-renal veins with regard to the collecting system [18]. Furthermore, imaging of the urological system can be used for disease progression in renal carcinoma, fi-

brosis or nephrocalcinosis, making kidney imaging a tool for prevention and diagnosis. Even though the presented approach demonstrated kidney features *ex-vivo*, renal structures can be visualized at high resolution in a fraction of the time that would be required for histological approaches. Moreover, both label-free and dye/nanoparticle contrast was demonstrated and differentiated. In this manner, the need for extensive tissue-preparation is eliminated, allowing the study of freshly excised specimens. The need of using complex reconstruction algorithms to compensate for frequent defects present in histological slices, e.g. holes, folds and tears, is also avoided [128].

6.4. Conclusion

The current chapter focused on studying the broadband spectrum of frequencies generated after light excitation of tissue. Initially two different approaches separating the spectrum of frequencies recorded using only a single detector were presented: a direct modality band-pass filtering the signals, and a more advanced wavelet decomposition. Both these modalities were investigated on real datasets acquired with two different transducers. Following the algorithmic approach, a hardware implementation offering the possibility of combining two detector arrays to record a broadband spectrum of frequencies was investigated. In this first implementation of 2B-MSOM, using multi-angle projection data, exhibited imaging resolution of better than 30 microns through at least 8 mm of opaque specimen. In this approach, two different recording bandwidths of 0.5 MHz - 12 MHz spectrum, and 2 MHz - 40 MHz were used in the cylindrical implementation scanner. Initial results showed the possibility to extract vascular structures with different sizes, and overall to complement the resulting images. Following the first study, where only anatomical information was recorded from a freshley excised organ, a more complex experiment was designed, showing the necessity of ultra-wide-band frequency recording for molecular and anatomical information recording. The results presented show that the use of a rich, five-dimensional data set is essential for accurate MSOM implementation. 2B-MSOM was found capable of retrieving fluorochromes and photo-absorbing particles over a wide range of structural complexity through a thick and opaque biological sample. 2B-MSOM resolved both anatomical information generated by the absorption of hemoglobin present in tissues as well as physiological information, like information on kidney clearance patterns and the result of injected agents. Although 2B-MSOM is in a much earlier development stage than SPIM, the resolution that 2B-MSOM achieves is possibly at a

better analogy to the resolution achieved in SPIM. SPIM can offer resolution of the order of 6 microns but requires specimen no larger than $200 - 300$ microns, assuming untreated specimen to ensure transparency, i.e. a depth/resolution ratio of 50 ($300 : 6$). Correspondingly, 2B-MSOM showed a depth/resolution ratio of 100 ($3000 : 30$). While these numbers are understandably approximate and largely depend on the specific samples imaged, they indicate that 2B-MSOM has an equal or better scaling capacity than SPIM. They also show that SPIM and 2B-MSOM could be complementary, in particular when considering in-vivo applications of specimen of varying sizes. With the current configuration, in-vivo optoacoustic imaging of endogenous contrast in other specimen such as small animals, fish, or rodent extremities could be envisioned in order to provide anatomical information. Moreover, detection of extrinsic contrast or the expression of reporter genes could reveal physiological or cellular and molecular parameters.

Chapter 7.

Towards *in-vivo* imaging: Conical Scanning Geometry for OA Imaging

In the current chapter, a third detection geometry was developed for optoacoustic wave detection in the context of *in-vivo* imaging of cancerous tumors implanted on laboratory mice. We term this configuration conical detection geometry, as it relies on the displacement of ultrasonic detectors on a conical grid. The scanning methodology involved herein is based on the translate-rotate geometry presented in section 5.2.5, adapted for *in-vivo* experiments.

In the current section we present volumetric imaging at mesoscopic scale in different tumors: mammalian implanted and subcutaneous implanted models. After initial studies using a lower frequency array, with bigger elements and longer focal distance allowing a better understanding of the requirements in building such a system, the system was altered to include a higher frequency transducer, providing increased resolution. The developed multispectral optoacoustic mesoscopic (MSOM) system allowed *in-vivo* visualization of the entire tumor mass with high resolution ($<70\,\mu\mathrm{m}$) and good penetration depth (up to $8-10$ mm). Tumor vasculature and surrounding vessels were successfully identified, and metrics of their dimensions (up to 70-80 $\mu\mathrm{m}$ diameter size) and branching order (up to order 5) were calculated. By multispectral optical excitation we show the possibility to non-invasively record molecular and anatomical information through entire tumor non-invasively, offering the possibility to extract features of endogenous reporter probes and exogenous optical agent distribution.

Some of the results presented in this chapter are also presented (at places with minimal or no changes) in the material in preparation entitled:

- *"High Resolution Multispectral Optoacoustic Tomography of the Vascular System and Constitutive Hypoxemia of Cancerous Tumors"* by Andrei Chekkoury[*], Antonio Nunes[*], Jérôme Gateau, Panagiotis Symvoulidis, Annette Feuchtinger,

Nicolas Bèziére, Saak Ovsepian, Axel Walch and Vasilis Ntziachristos.

7.1. Motivation

Angiogenesis is a key marker for cancer biology research and monitor of tumor therapy. The vascular network within the tumor microenvironment plays an important role in tumor detection, treatment and further development [129]. The development of tumor vascular network is known to be tightly linked to angiogenesis, one of the most important hallmarks of cancer [130]. In normal angiogenesis, there is equilibrium between pro-angiogenic and anti-angiogenic growth factors, allowing the newly formed vessels to mature and become organized and stable. However, during tumor-derived angiogenesis, there is a loss of balance between the pro- and anti-angiogenic signals, causing continuous growth of new tumor blood vessels. This continuous growth supports the fast cell proliferation and consequently expansion of the tumor mass. During this pathological process the newly formed vessels become irregular and with tortuous shape, and together with an abundant presence of shunts causes an overall inefficient and abnormal blood perfusion [130, 131]. *In-vivo* imaging of tumor vasculature is therefore a key tool used to offer information regarding malignant features of the tissue, and provide a better understanding of vascular structure, function and angiogenesis [132]. Particularly relevant for tumor biology research, imaging of tumor vasculature can assess the efficacy of anti-tumor and anti-angiogenesis drugs, increasing the accuracy of prediction and monitoring tumor therapy response.

Currently, the gold standard for measuring the increase in vascularization with altered vascular features is by histological estimation of microvessel density (MVD), which quantifies and averages the number of microvessels in a particular region [133]. Measurement of MVD provides an index of minimal intercapillary distance, constituting a significant prognostic indication in many cancers, albeit not reliable in all tumors. Although immunochemical staining of specific markers can potentially improve vascular network detection, this modality requires tissue biopsy that is not only susceptible to sampling errors but is not feasible for serial monitoring of tumors [132]. Moreover, as histological technique is intrinsically a bi-dimensional imaging modality, and only after applying complex algorithms and intensive post-processing modalities three-dimensional ($3D$) structures can be extracted. These limitations expose the need for validation and standardization of new non-invasive monitoring techniques

---

* equal contribution

for imaging tumor vascularization. X-ray computed tomography (CT) has been used as a tool to image tumor vasculature mainly due to its good spatial resolution [134, 135]. However, CT is often associated with poor signal-to-noise ratio and its radiation exposure remains a potential drawback. Other methodologies, such magnetic resonance imaging (MRI), have successfully been employed in tumor imaging, achieving high spatial resolution. Dynamic contrast enhanced-MRI (DCE-MRI) exhibits excellent soft tissue resolution, however the assessment of tumor vascularization relies on the use of external paramagnetic contrast agent, mostly Gadolinium-based, usually associated with risks of adverse effects. Importantly, quantification of tumor vascularity using DCE-MRI is technically challenging, in particular for larger vessels due to the lack of a direct relation between MRI signal intensity and contrast agent concentration [136]. DCE-MRI is also associated to low sensitivity for small vessels, as the visualization relies on the bulk effect of the enhancement on the signal by the local accumulation of contrast agent.

Intravital microscopic techniques (confocal and multi-photon microscopy) can also be used for molecular and functional neovasculature imaging, showing at microscopic level and with minimally invasive tissue damage biological activity *in-situ* [137]. Due to a small field of view, and relative shallow penetration depth ($<500\,\mu m$) entire tumor imaging is not possible. On the other hand, deep tissue optical imaging was enabled by means of optical based techniques, such as FMT [3] and Ultramicroscopy [74]. FMT provides tomographic imaging of entire small animals, revealing the distribution of vascular features at the cost of extrinsic contrast agent and relatively low resolution. Higher resolution could be achieved by means of ultramicroscopy, performed typically in small organisms and excised organs. Recently, multispectral fluorescence ultramicroscopy, a $3D$ optical sectioning imaging modality, has been used for imaging the vascular networks in murine tumor models attaining very high in-plane resolution ($6\,\mu m$) [74]. However, due to light scattering in tissue, a chemical procedure clearing the tissue before imaging must be performed, therefore, its *in-vivo* use is restricted.

On the other hand, optoacoustic imaging as a hybrid modality, has the potential to investigate the typical hallmarks of cancer, in particular angiogenesis, by providing contrast specific to optical imaging modalities, good molecular specificity at ultrasonic resolution. Using single wavelength optical excitation combined with single element piezoelectric (PZT) detectors, optoacoustic implementations have been used to monitor angiogenesis during early tumor growth and over longer periods of time [138, 139, 140]. Optical interferometry modalities combined with single wavelength excitation, have also shown

the possibility to visualize tumor growth and treatment response during longitudinal acquisitions [24]. Overall, these implementations raster scan a single element detector over the area of interest. To date, the hardware limitations imposed by the existing technology and the high demands on the resolution performance, restricted optical excitation used on these implementations to single wavelength lasers. Contrary, multispectral modalities can enable spectral differentiation of endogenous and exogenous reporters, contributing to a better understanding of the anatomical, functional and molecular aspects of cancer. The recent advances in optoacoustic implementations, image reconstruction and spectral un-mixing techniques, open up the possibility of using a broad variety of nanoparticles and/or near-infrared (NIR)-dyes [141], that could potentially enhance multispectral optoacoustic mesoscopy (MSOM) tissue contrast, ideally suited for sensing optical contrast of cancer hallmarks in three dimensions.

Previous results based on the previously presented linear and cylindrical geometries, demonstrated the unique ability to generate volumetric datasets at mesoscopic scale in excised intact samples using a translate-rotate optoacoustic scanner employing linear transducer arrays. Based on these findings, the additional possibility of detecting extrinsic contrast agents in small biological samples with good time (approximately 1 hour) and spatial (approximately $30\,\mu\text{m}$) resolution [15] was explored and discussed in section 5.2.5. In the current section we describe the experimental procedure and the necessary steps performed in order to adjust the translate-rotate geometry to a cylindrical implementation allowing optimal recording of *in-vivo* optoacoustic signals.

7.2. Experimental System Development and Characterization

In the current section, the system modifications required by translating the previous cylindrical geometry to *in-vivo* applications are discussed. The conical geometry will be introduced and a discussion regarding the acquisition procedure will be presented, together with advantages and limitations of the current application.

7.2.1. Preliminary considerations

Considering the nature of the samples to be investigated, the cylindrical configuration had to be modified to account for two aspects: on one hand, the tumors
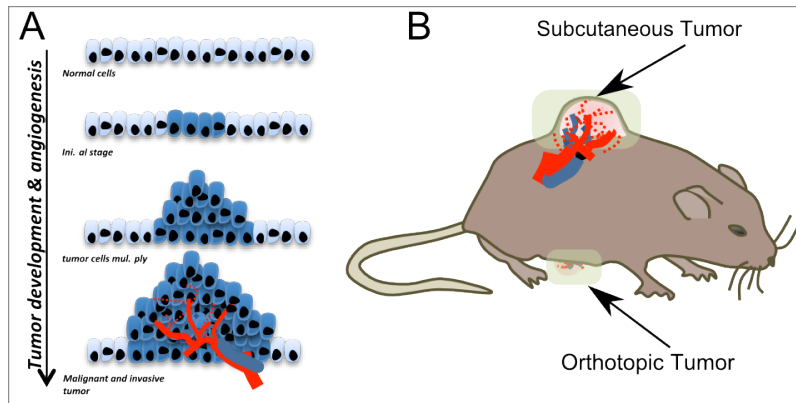
Figure 7.1.: Schematic: tumor growth stages and experimental animal models. (**a**) Different stages of tumor development and angiogenesis, growing from normal cells passing through the initial stage, multiplication resulting in malignant and invasive tumors. (**b**) Two animal models used throughout this work: subcutaneous (implanted under the animal's skin) and orthotopic (mammalian cells implanted on the mammalian pads) tumor models.

could have only been placed on the ventral or dorsal side of the animals. This means that in order to be able to attain enough views of the sample, the tumoral mass had to be oriented towards the detecting geometry. Including the focusing characteristics and aperture of the array, one possible way was to include an additional tilting of the array, such that the transducer is pointing towards the tumor. The second aspect to be considered was the *in-vivo* aspect of the experiment, requirement imposing the sample to be placed over the surface of the coupling medium (in this case water). Considering both these aspects, the solution proposed in the current work, introduces a tilting of the array with respect to the vertical axis, allowing access of the transducer to the sample, while the mouse body is placed horizontally, on it's dorsal or ventral side (depending on the spot of the tumoral injection) above the water surface. In order to asses the optimal angular tilting used by the conical geometry implemented in the present chapter, two aspects had to be taken into consideration: on one hand the angular tilting of the array's aperture will reduce the height of the volume that can be scanned, by reducing the vertical aperture. On the other hand, the tilt will affect the $3D$ resolution compared to the cylindrical implementation: along the z-axis an improvement was expected due to a broader angle of acceptance along this axis, while along the xy-plane a degradation of the resolution was expected most probably due to a break of symmetry along the detector positions.

Figure 7.2 shows four plots corresponding to four different angular tilting positions of the array at 0, 30, 45 and 60 degrees. These results are based on simulations and the angular positions were selected based on possible experimental implementations. The left columns of *fig.* 7.2 show the first (red) and the last (blue) detector positions on a simulated 180 degree scanning configuration. The black line at coordinates $x = 0$ corresponds to the simulated absorber, mimicking a vertical suture. It can be seen that angular tilting of the array will reduce the height of the volume "seen" by the array. Moreover, by analyzing the reconstructed MIP images along the *xz*-plane, the effects of tilting the array are more obvious. In *fig.* 7.2 **a**, the right column depicts a reconstruction of the suture along the entire aperture of the array ($-2 - 4$ mm along the *z*-axis). By looking at the right columns of *fig.* 7.2 the reduction in height of the reconstructed volume is clear for angular positions expanding past $30 - 45$ degrees.

To calculate the entire volume that could be spanned in the cylindrical configuration for different angular positions, a simulation has been performed using a more dense discretization of the angular positions (every 1 degree), and the results are presented in *fig.* 7.3 by the blue curve. The height of the volume that can be scanned with an angular tilting at 45 degrees corresponds to $6.34\,\mathrm{mm}$. This value corresponds to an implementation performed using the high-frequency linear array presented in section 3.3. Similar considerations must be taken into account when using a different array with a different focal distance and aperture along the *z*-axis (like the low-frequency array, used in preliminary studies), which will enable a bigger vertical aperture.

The second aspect taken into consideration during the assessment of the angular position was resolution performance. A simulation study considering the cylindrical scanning geometry implemented using different angular positions was performed. The simulated absorber was considered a homogeneous microsphere, sized $10\,\mu\mathrm{m}$, placed in the focal point of the array, corresponding to the center of rotation for the scanning geometry. The simulation was performed by using parameters similar to experimental capabilities: a rotation range of 180 degrees, with a 1.5 degree angular step, with a translation range spanning $1\,\mathrm{mm}$ and a translation step of $150\,\mu\mathrm{m}$. The reconstructed results corresponding to the four angular positions are presented in *fig.* 7.3 **b-e**. The left column shows a lateral view (*xz*-plane) of the microsphere, while the right column shows a top view MIP of the *xy*-plane. It can be seen that in the lateral view, for the 0 degrees tilting (cylindrical configuration) the microsphere appears to look like a rice-grain, while for other angles, the height of the microsphere reduces. On the other hand, a degradation of the resolution along the *xy*-plane can be observed in *fig.* 7.3 right column, and might be due to the incoherent summation of the
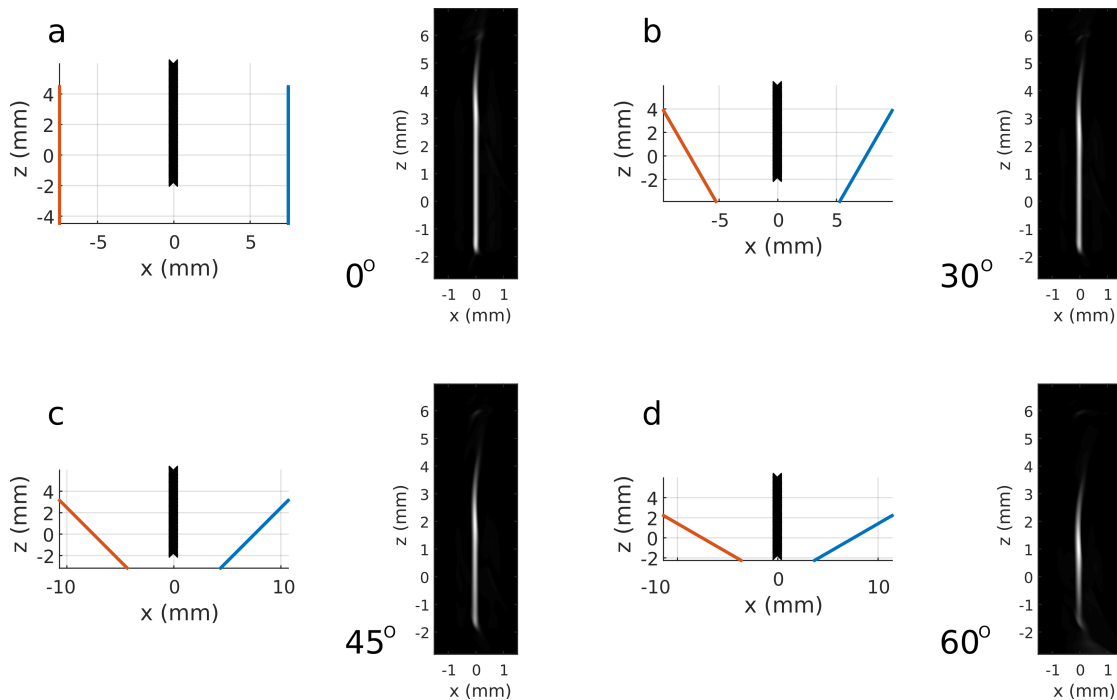
Figure 7.2.: Influence of angular tilting with respect to height of the volume and field-of-view. Left columns represent the first(red) and last(blue) detector position in a tomographic scan. Right column is an MIP image along the *xz*-plane depicting the reconstructed absorber. (**a**) 0 degrees inclination angle - corresponding to the cylindrical configuration; (**b**) 30 degrees tilting; (**c**) 45 degree tilting and (**d**) 60 degree tilting of the array.

sound waves and particularly the side detected lobes, at opposed positions of the transducer array.

For the required applications, namely the *in-vivo* imaging of biological sample, the optimal desired specifications with respect to resolution, were a small discrepancy between the three values of the resolution. In order to assess the $3D$ resolution for different angular tilting positions of the array, a FWHM profile along the three dimensions was performed for each angular inclination of the array. In *fig.* 7.3 **a**, the standard deviation of the resolution along the three dimensions computed on the $10\,\mu m$ sphere is presented. A small standard deviation of the three values along the x, y and z axis corresponds to homogeneous value. It can be seen that for 45 degrees the standard deviation is minimal, meaning the resolution is almost homogeneous, and it was calculated to be approx. $70\,\mu m$.

Summarizing, the simulated results conclude that for the high-frequency array, and for an angular tilting of 45 degrees, the height of the volume that can be encompassed in the conical configuration corresponds to 6.34 mm with an almost homogeneous resolution of under 100 µm. The *in-vivo* samples that were investigated using the current implementation were mouse tumors, implanted either subcutaneously or orthotopically, no bigger than 7 mm in height (*z*-plane) and 1 cm³ along the *xy*-plane.
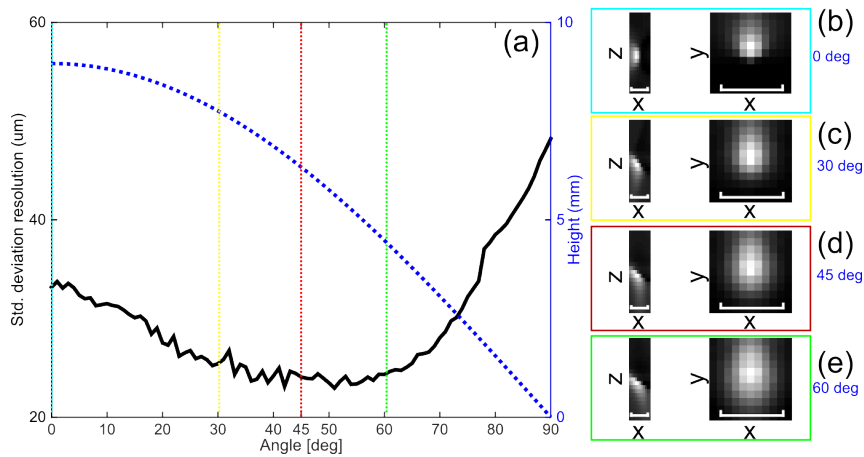

Figure 7.3.: Influence of angular tilting with respect to resolution. (**a**) Plot of the height of the encopassed volume with respect to angular tilting of the array (blue curve). Black curve represents the standard deviation of the 3D Resolution computed on 10 µm microspheres. *xz* and *xy* profiles of the microsphere for (**c**) 0 (**d**) 30 (**e**) 45 (**f**) 60 degrees angular tilting of the array

7.2.2. Experimental Optoacoustic Scanner

Based on the previously presented results of the simulations, a 45 degree angular tilting of the transducer was implemented, and the system was adapted to operate in a conical configuration. A custom made 45 degree component was built and attached to the bottom part of the translation stage (see *fig.* 5.2 **b** and 7.5 **b**), in order to support an adapting rail holding the transducer at a 45 degree inclination angle and the schematic of the holder is presented in *fig.* 7.4 **c** and **d**. To adapt the possibility of *in-vivo* imaging a custom made solution was found to support the animal above the water level, providing the anesthesia and the necessary weight of the body, while the tumor had to lie under the water surface, for good acoustic coupling. The sample holder was custom made and built out of PMMA material to support the sample and the illumination fibers

and is presented in *fig.* 7.4 **a** and **b**. The sample holder had a protrusion measuring 12 mm in diameter, equivalent to the maximum opening of the agarose mold cylinder (for phantoms) during the scanning procedure, and to the maximum planar footprint of the murine tumors. The illumination was provided to the sample using the four arm fiber bundles and was fixed, maintained single-sided throughout the scanning procedure. The excitation light was guided by a fiber bundle consisting of 640 fibers partitioned in 4 arms (*fig.* 7.5 **a**). The fiber arms are positioned on an arc 1 cm away from the sample, oriented towards the sample, allowing optical excitation in a volume of $1\,\mathrm{cm}^3$, optimal for tumor imaging.
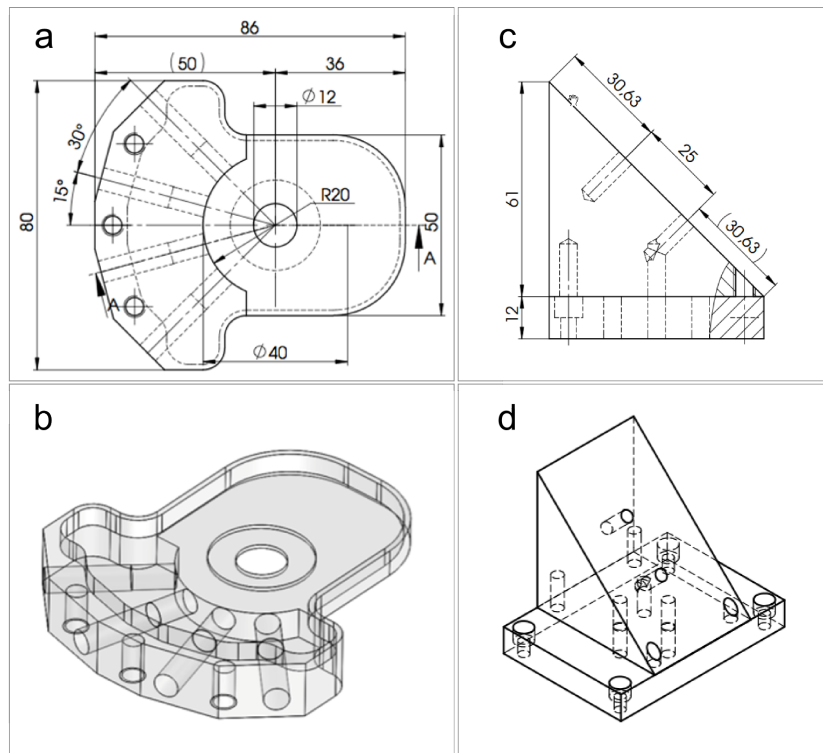
Figure 7.4.: Conical tomographic implementation - Building blocks: (**a**) and (**c**) The mouse holder used for the *in-vivo* experiments, accommodating the sample and the four arm illumination fiber bundles; (**b**) and (**d**) 45 degree plate used to introduce the angular tilting.

The ultrasonic detection was performed using a high-frequency 128-element linear array (Vermon, Tour, France) with a 24 MHz central frequency and an average -6 dB two-way bandwidth of 60%, previously presented in section 2.3.

The linear array is mounted on the custom made holder previously described. This angular tilt ensures access of the transducer to the sample under investigation given the possibility to detect waves generated by a multitude of absorbers having different orientations, situation describing the disordered tumor environment. Near-infrared excitation light was provided by a tunable optical parametric oscillator (OPO) laser (OPOTEK, Carlsbad, CA, USA) yielding nanosecond-long pulses with a 10 Hz repetition rate.
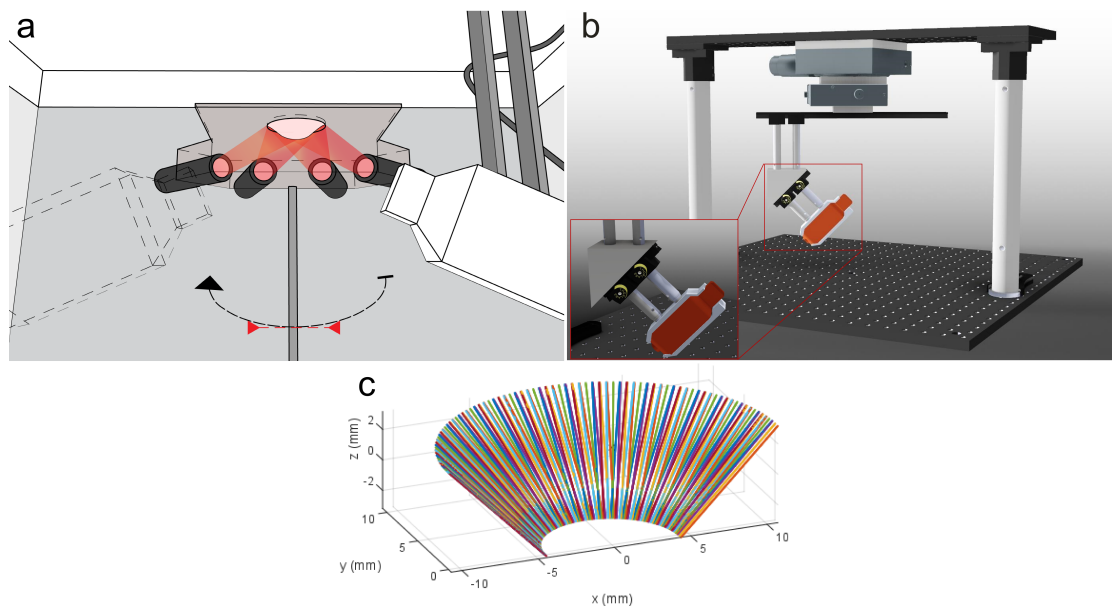

Figure 7.5.: Conical tomographic optoacoustic mesoscopy - Experimental set-up: (**a**) Sample holder including the fiber holders for delivering illumination and transducer array angled to allow access to the sample (**b**) System implementation: the transducer is mounted on a specially designed holder, mounted on a custom made triangular component having 45 degrees angular tilt; (**c**) The conical enclosure of the detector displacement positions around the scanned sample.

The scanning routine used by the optoacoustic imaging system implemented herein, is based on the translate-rotate continuous implementation, presented described in section 5.2.5. This scanning implementation was selected for providing homogeneous in-plane resolution and good sensitivity to all orientation absorbers. The linear array was continuously rotated and translated with a predefined speed selected based on the repetition rate of the pulsed laser. For each laser shot, the single shot recordings were transferred to the DAQ and digitized. For the current experiments, the transducer was rotated 172 degrees around the

sample, and the array described a linear motion measuring 9 mm. The radius described by the transducer's middle element (64) was determined to be 6.3 mm, and it corresponded with the middle plane of the sample under investigation. For the experiments with tumor bearing mice, the animals were placed on the bed holder, exposing the tumor mass region through the hole of the holder to enable direct contact with pre-heated water, acting as acoustic coupling medium.

7.2.3. System characterization: Field of view and resolution

In order to validate the concept of *in-vivo* imaging using a linear array scanned in a conical configuration, initial measurements were performed using the low-frequency linear array introduced in section 2.3. The lower frequency (6 MHz), longer focal distance and increased element size, enabled preliminary insights into the limitations and advantages of using such a detection geometry in a translate-rotate scanning modality, with increased tolerance to miss-calibrations and displacements during the development phase of the system.

The array was mounted on the 45 degree holder presented in *fig.* 7.4 **c** and **d**, and the samples were placed on a custom made holder built by shaving off the upper top side and drilling a circular hole with a 1 cm diameter in a 50 mL laboratory falcon. Optical excitation was delivered using the 4-arm fiber bundles, placed at $3 - 4$ centimeters from the sample.

After initial system calibration (section 5.2.3), in order to assess the system's capabilities in terms of field of view and $3D$ capabilities, two different absorbers with known patterns were used. The first phantom used a 300 μm suture thread embedded vertically in the supporting medium to create a double knotted structure. A photograph of the suture is presented in the inset of *fig.* 7.6 **a** next to the MIP lateral view of the reconstructed optoacoustic volume. It can be seen that the height of the volume recorded using the low-frequency array measured 10 mm in height, corresponding to the diameter of the holding syringe presented in the inset. It can be observed that except the lower-right corner of the MIP reconstruction, the sample is recorded with good accuracy throughout the entire volume, although the sample contains a complex structure, with a suture thread emitting acoustic waves along a broad range of directions. We consider the lower corner artifacts as being generated by a certain orientation of the suture thread, not emitting any acoustic waves intersecting with the detection geometry (see section 2.1.4).

Figure 7.6 **b** shows a MIP along the *xy*-plane, depicting the second phantom used for system characterization. The 9 absorbers measure 200 μm in diameter,
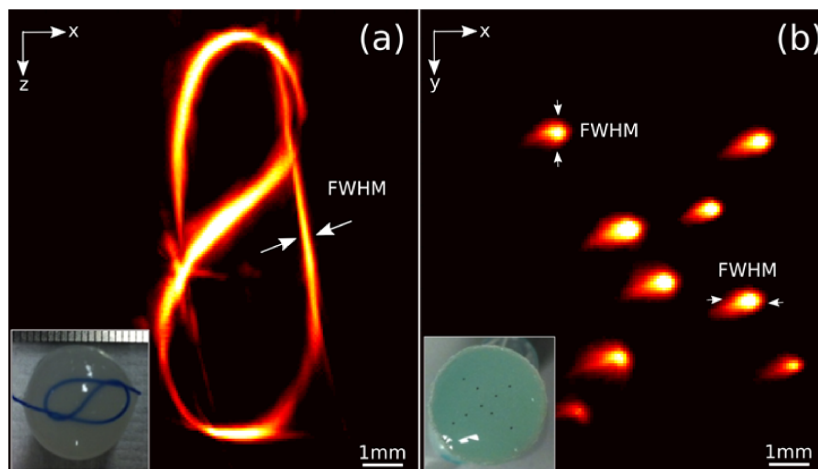
Figure 7.6.: System characterization: Low-frequency phantom experiments: (**a**) MIP
lateral-view of the vertically placed $300\,\mu m$ suture formed in a knotted loop. Photo-
graph of the sample before embedding in the final agar phantom in the inset. (**b**) MIP
top-view of the 9 microspheres ($200\,\mu m$ in diameter), distributed over the entire surface
of the supporting phantom. Photograph of the sample is presented in the inset bottom
left.

and were displaced over the entire surface of the holding syringe (5 ml syringe,
9 mm in diameter) as can be seen on the inset of *fig.* 7.6 **b**. The microspheres ap-
pear to have a homogeneous resolution along xy-planes, but a tilting along the
yz-plane is observed, which might be due to limited view artifacts. Moreover,
as previously presented in the section describing the limitations of the current
implementation, the entire plane of microspheres is placed in the region inside
of the conical structure, resulting in a homogeneous resolution.

A similar experimental procedure was performed using the high-frequency
array. The system was further altered to include modifications allowing the
high-frequency linear array to be used in such a configuration. The sample
holder was the one presented in *fig.* 7.4 **a** and **b**. The volumetric capabilities
of the system to image multiple orientations were characterized using Phan-
tom 3, and the results are presented in *fig.* 7.7 **a** - **c**. The phantom comprised
of a single suture with $30\,\mu m$ diameter, arranged in a single-looped knot. The
complex shape of the knot was reconstructed over the entire volume of interest,
measuring 9 mm in height and $10 * 10$ mm along the xy-plane, and is presented
in *fig.* 7.7 **a**. An intensity profile along one side of the suture (yellow line in *fig.*
7.7 **a**) was computed and the full-width-half-maximum profile was determined
to be $35\,\mu m$ - *fig* 7.7 **c**. The top view maximum amplitude projection of the re-

constructed volume is presented in *fig.* 7.7 **b** and shows the circular pattern of the single-looped knot. *Figure* 7.7 **a-c** shows that the reconstructed volume does not present any elongation along any directions, implying a homogeneous resolution in the field of view.
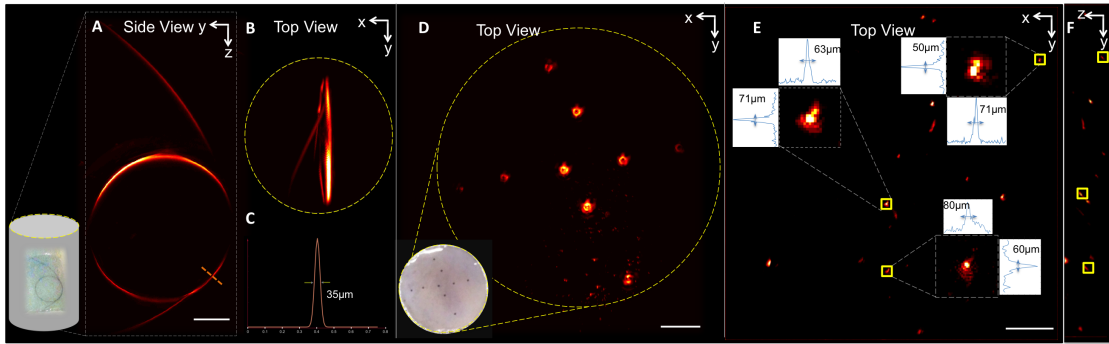

Figure 7.7.: Experimental system characterization: (**a-c**) Phantom containing a $30\,\mu m$ diameter suture in a loop shape; (D) Phantom containing 9 microspheres with $200\,\mu m$ diameter, spread on the entire surface of the sample; (**e-f**); Phantom containing $10\,\mu m$ diameter microspheres randomly distributed in the sample.

In order to characterize the field-of-view of the experimental setup using the high-frequency array, a phantom comprised of 9 microspheres with $200\,\mu m$ diameter was scanned. The microspheres were arranged to form a "plus" sign along the entire surface of the supporting syringe (inset of fig. 7.7 **d**), measuring $10\,mm$ in diameter. The reconstructed maximum amplitude projection image along the plane of interest - *xy* - is presented in fig. 7.7 **d**. The microspheres can be clearly resolved along the entire diameter of the sample, and dust particles on the side of the phantom can be observed on the lower part of the reconstructed volume.

The fifth phantom, comprised of microspheres of $10\,\mu m$ diameter randomly spread in the content of the agar phantom was imaged in order to determine the resolution of the system with respect to isotropic objects. Three different microspheres, situated at different depths and random in-plane positions were selected, and the FWHM resolution was computed based on their intensity profile. The resolution was determined to be (mean $\pm$ standard deviation): approx. $70\,\mu m$ along all dimensions. Compared to the optoacoustic implementation using the same transducer in a cylindrical configuration, the tilting of the transducer results in a degradation of the resolution along the *xy*-plane, but an improved elevation resolution due to smaller inter-element spacing. Overall we note that the system achieved a homogeneous resolution along the *x, y, z* -

dimensions, ideal for biological applications.

7.2.4. Limitations

From a limitation point of view, other than the previously exemplified field of
view and resolution capabilities, an important aspect to be discussed relates to
any limited view and directionality aspects in the context of the conical scanner.
These aspects have been previously introduced in section 2.1.4. In the conical
implementation presented herein, the current limitations imposed by the detec-
tion geometry are discussed.

It is important to note, that in the conical implementation, the entire recorded
area considered to be the full-view area, is not consistent to the cylindrical im-
plementation presented in chapter 5. In *fig.* 7.8 **a** the case of a vertical structure
scanned in a cylindrical configuration is presented. It can be seen that if the ver-
tical suture is recorded from different positions around the sample, the vertical
recording capabilities of the system correspond to the height of the array. In
this case, the entire vertical field of view will correspond to the height of the red
square. Implicitly, the full view area will correspond to the same height of a 2D
image (the B-mode equivalent in ultrasound imaging). In the case of the conical
implementation, by rotating the transducer around the investigated sample, the
length of the full view area will be reduced. By tilting the transducer by a given
angle, the B-mode image, depicted by the blue square in *fig.* 7.8 **b** will have a 45
degree orientation, with respect to a vertical suture (red dotted line). The con-
sequences of this angular tilting are two fold: on one hand, the B-mode image
used to validate the positioning of the sample will resolve the vertical structure,
but on the other hand, in the final scan, the height of the suture will differ, as
the 3D visualization will only sum-up coherently enough views from a smaller
area (the striped region in *fig.* 7.8 **b**). This results in a reduced height of the
full-view area, and must be accounted for during the calibration and scanning
procedure, by carefully considering the positioning of the sample with regard
to the transducer position.

In addition to considerents regarding the 3D visualization of vertical struc-
tures, additional constraints are currently imposed on the detection geometry.
The scanning of the array in the 45 degree tilting configuration introduces se-
vere limitations in terms of spatial distribution of hardware components. Using
the holder presented in *fig.* 7.4 **a** and **c**, the four arm illumination bundle spans
a broad angular coverage, in order to deliver homogeneous illumination to the
sample. This limits the detection geometry to single sided access. A reduction in
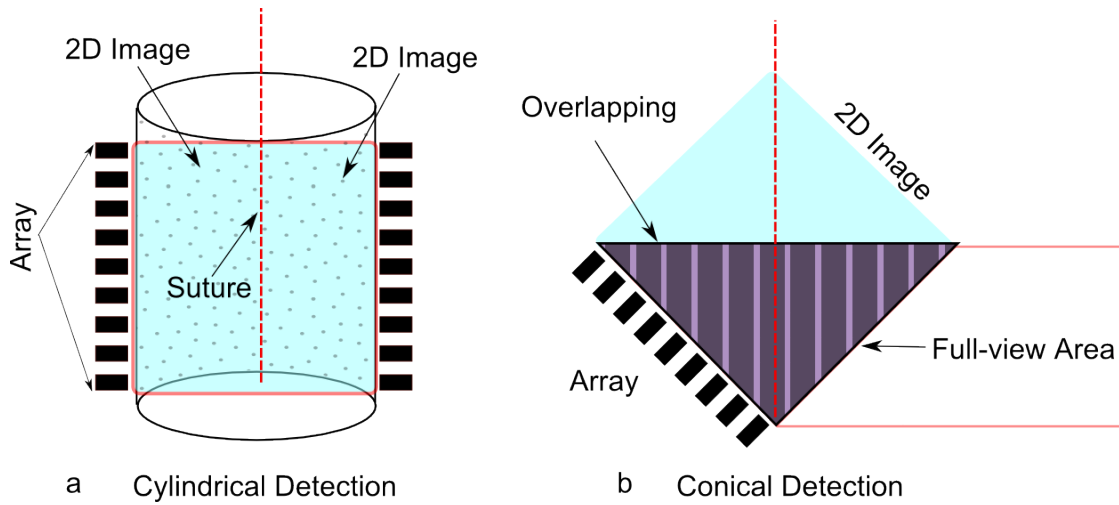angular arrangement of the illumination fibers, would enable additional space

Figure 7.8.: Considerents for limited-view artifacts in conical scanner: (**a**) Cylindrical considerents for wave recording generated by a vertical structure; (**b**) Conical representation of the limited field of view in visualization of a vertical suture.

for increased angular coverage.

7.3. Application: Conical geometry in *in-vivo* cancer imaging

The *in-vivo* capabilities of the system were tested with several tumor mouse models, implanted subcutaneously on the dorsal side of the animal, or orthotopically in the mammary fat pad. In the present, the results obtained from two different tumor models implanted in different sites of the mouse are presented. The following section is divided into two sub-sections summarizing the experimental results based on intrinsic optoacoustic contrast, and following endogenous contrast administration. We note that several other experiments have been performed including longitudinal tumor growth monitoring, the effects of extrinsically administered drugs, as well as targeted fluorescent agents, but we consider them outside of the scope of this thesis and for brevity reasons will not be included.
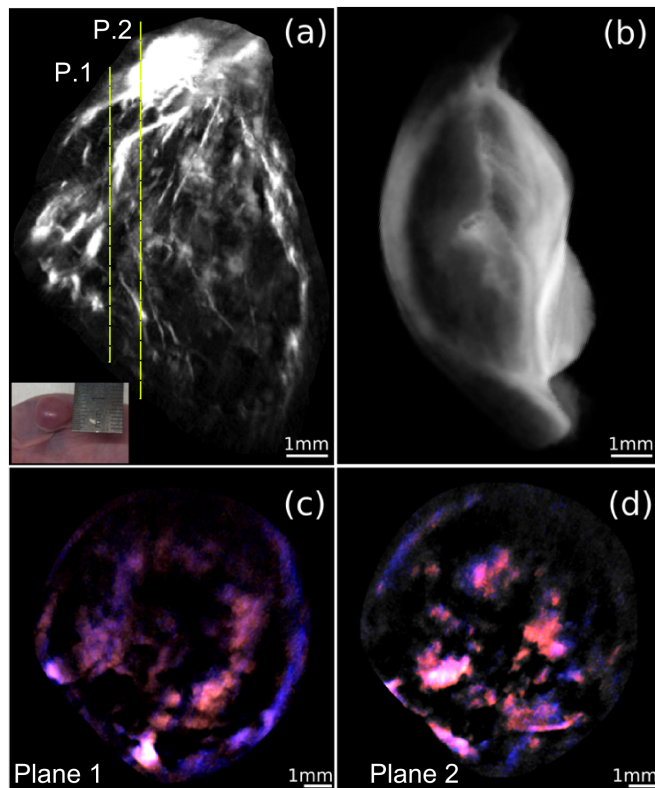
Figure 7.9.: *In-vivo* conical imaging using a low-frequency array for functional imaging
of a 4T1 subcutaneously implanted tumor (photograph presented in the inset). (**a**) MIP
lateral-view of the reconstructed volume, (**b**) MIP of the cryo-sectioned sample post
experiment, (**c**) and (**d**) 2D Cross-sections acquired at different heights, marked with
the yellow dotted lines in (**a**). The anatomical image in gray is overlaid with red (oxy-
HB) and blue (deoxy-HB).

7.3.1. Low-frequency conical scanner for *in-vivo* imaging

An *in-vivo* experiment was performed by using a nude mouse, 15 days post
subcutaneous implantation of a 4T1 tumor (1.5 million tumor cells). The exper-
iment was performed by placing the mouse in the special designed holder, with
the dorsal side oriented towards the detection geometry. Only the tumor was
submersed in the water tank, while the mouse was anesthetized using Isoflu-
rane. The scanning routine involved detecting optoacoustic signals from 180
degrees around the mouse, by moving the array to 120 angular positions, and
using a 14 mm translation range. During the scanning routine, multispectral
acquisition was performed by following the procedure previously described in

section 2.2.2. The selected excitation wavelengths were 700, 760, 800 and 850 nm, spanning the absorption spectrum of hemoglobin (see *fig.* 2.5 for absorption spectrum of hemoglobin in the near infrared). The four wavelengths were selected in order to enable differentiation of the two compounds present in blood: oxygenated and deoxygenated hemoglobin, by means of post-processing spectral un-mixing methods. For un-mixing purposes, the same linear un-mixing procedure presented in section 6.3.4 was used, considering two spectral components, namely oxy and deoxy-blood. *Figure* 7.9 a shows a MIP lateral view of the reconstructed tumor, corresponding to an optical excitation of 760 nm. The figure captures the entire tumor mass, measuring $1cm^3$. The reconstruction presents the network of vessels present in the tumor mass, as well as other absorbing structures. On the top of the MIP view, a strong saturated signal depicts an area which is severely affected by necrosis (death of the tissue visible as a black point in the color photograph presented in the inset). In *fig.* 7.9 **c** and **d**, two cross-section images, with a thickness of 75 μm, are presented. The base colormap depicts the anatomical image, corresponding to an excitation wavelength of 760 nm. The overlay color images correspond to oxy-hemoglobin (in red) and deoxy-hemoglobin (in blue), respectively. It can be seen that in the cross-section images, the absorbing structures present in the tumors range from smaller vasculature to blob-like continuous structures. For validation reasons, after the experimental procedure, the tumor was excised and embedded in a supporting medium, frozen and sectioned in thin slices using a micro-tome (see section 2.6). A similar view, corresponding to the MIP view presented in *fig.* 7.9 **a** is shown in *fig.* 7.9 **b**. Although the general shape of the tumor is consistent with the results presented using the optoacoustic system, the small absorbing structures, as well as bigger blob-like structures, are sized below the resolution capabilities of the system, and therefore not visible. This result further strengthens our hypothesis of needing a volumetric optoacoustic approach in studying tumor vasculature, development and treatment efficiency.

Based on the previous results, the system was further modified to include the high-frequency linear array, allowing a higher resolution and better visualization capabilities in *in-vivo* tumor imaging compared to the low-frequency 6 MHz array.

7.3.2. High-frequency conical scanner for *in-vivo* cancer imaging

An *in-vivo* subcutaneous tumor model was selected to be imaged on day 10 post-inoculation (1.5 million tumor cells). A schematic of the animal together

with a photograph are presented in *fig.* 7.11 **a** and **b**.The tumor was located on
the dorsal side of the animal - mouse #1, around the renal system, and measured
to be approximately $1\,\mathrm{cm}^3$ - *fig.* 7.11 **c**. The subcutaneous 4T1 tumor model was
imaged *in-vivo* in order to investigate the tumor vasculature distribution inside
the entire tumor mass. *Figure* 7.10 **a** shows a volume-rendered 3D image of the
reconstructed optoacoustic data-set, acquired at 760 nm excitation wavelength.
The images presented herein are color-coded to reveal different structural sizes
obtained with the same linear array. In section 6.1.1, the post-processing modal-
ity used to obtain these images is described. Briefly reiterated, the method uses
a wavelet decomposition of the signals, in order to extract two levels of de-
tails. In this case, the method is using a db2 level of wavelet decomposition,
in order to extract small and larger sizes structures, corresponding to vascular
and anatomical features present in the tumor. The size dependent color-coded
image presents tumor vasculature with diameters ranging from $70\,\mathrm{\mu m}$ up to
$250\,\mathrm{\mu m}$, present in the entire tumor mass. The image depicts small diameter ves-
sels existing on the superior side of the tumor, as well as deep inside the tumor
mass. *Figure* 7.10 **b** shows a MIP view along the *xy*-plane, presenting the tumor
from a top-bottom view. The figure shows that superficial vasculature can be re-
solved, as well as smaller blood vessels branching into additional vasculature.
For preliminary validation purposes, the result is correlated and presented in
fig. 7.11 **b** and **d**. *Figure* 7.10 **c** shows a side view of the tumor, where the vertical
dimension represents the depth-axis. It is discernible that the system records
vasculature along the entire vertical tumor mass, potentially allowing detec-
tion of vessels originating from mouse body as well as on the surface of the
tumor. *Figure* 7.10 **e-g** present three $2D$ top view projections at different vertical
(z) positions are shown, displaying the tumor vasculature and the surround-
ing vessels of the tumor at different depths. The three planes were selected in
order to visualize vascular development at different depths from the tip of the
tumor, as represented in schematic on *fig.* 7.10 **d**. Here, different structures are
distinguishable based on their dimensions. Larger vessels (green/yellow color)
can be identified specially on the periphery of tumor mass, whereas smaller
vessels/microvasculature (red color) are more present in inner locations within
tumor mass. We note that throughout the reconstruction of the current datasets,
a sound attenuation correction (see section 6.1.2) was performed in addition to
the wavelet decomposition, in order to correct for attenuation of higher frequen-
cies recorded by the detection.

In cancer imaging, vascular diameter and the degree to which the vascula-
ture in a tumoral mass is branching can provide valuable information regarding
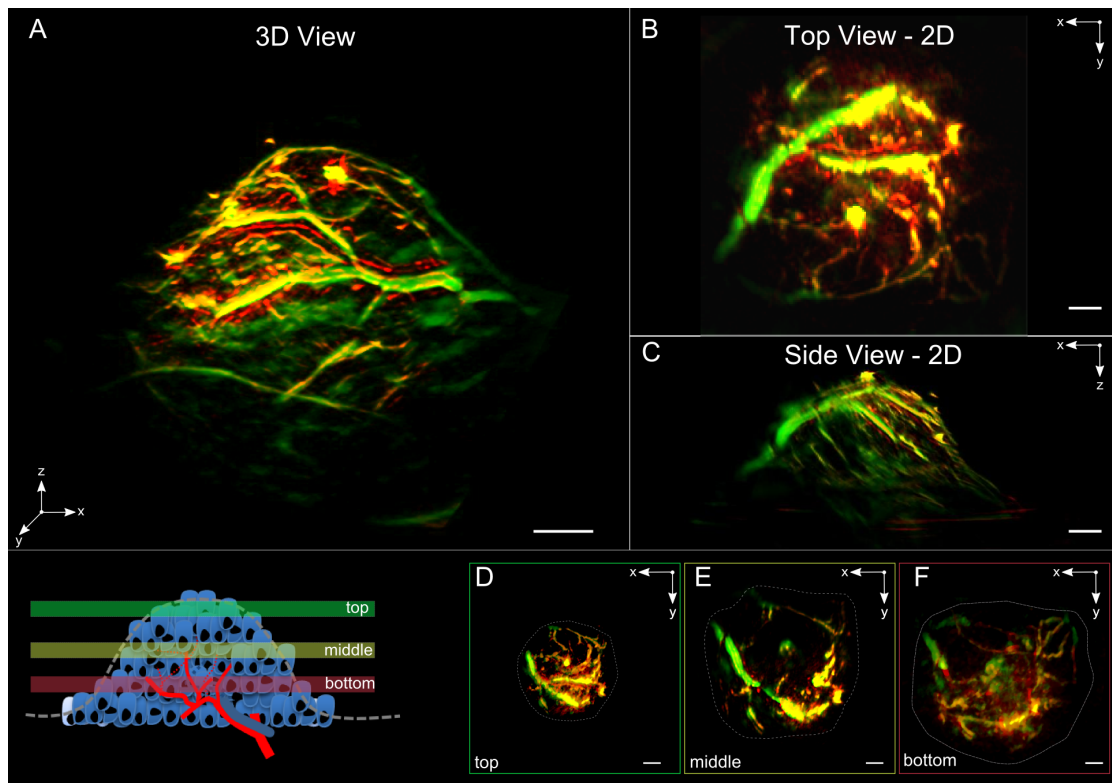the local blood flow, tissue oxygenation capabilities and drug delivery efficacy,

Figure 7.10.: *In-vivo* imaging of endogenous contrast agent: Subcutaneous *4T1* tumor model (a) Volume rendered image of the entire tumor reconstruction; (**b**) $2D$ MIP top view of the tumor mass; (**c**) $2D$ MIP side view of the tumor. Inset - Representation of the different vertical positions selected from the top, middle, and bottom of the tumor mass. (**d-f**) Visualization of $2D$ (*xy*) planes of the tumor mass at top(**d**), middle(**e**) and bottom(**f**).

enhancing the success of cancer therapy [142]. Moreover, the branching and tortuosity aspects of cancerous vessels can severely affect delivery and monitoring of injected drugs, further enhancing the necessity to accurately image, measure, quantify and follow the development of vascular networks in tumors [143]. To illustrate the potential of the optoacoustic system to evaluate the vessel diameter and branching order, two regions of interest were selected from the reconstructed optoacoustic data of the tumor-bearing mouse #1. *Figure* 7.12 **a** and **b** represent two different regions of interest selected inside the tumor mass. *Figure* 7.12 **a** shows a MIP image selected on the top area of the tumor, and shows the vascular network and the corresponding branching of superficial vessels. The second region of interest (*fig.* 7.12 **b**) was selected on the periphery of the

Figure 7.11.: Subcutaneous 4T1 tumor model monitored by MSOM. (**a**) Schematic of the subcutaneous model. (**b**) Color photograph of the mouse model used and (**c**) High magnification of the tumor. (**d**) 2D MIP top view of the tumor mass by MSOM. Co-registration of the tumor margins (dashed line), necrotic spot (Ns), and superficial vasculature (sV) and branching (asterisk).

tumor, and depicts part of the vascular system surrounding the tumor mass. The successive branching was identified and classified from $B1$ (bigger diameter size - close to the main vessel source) to $B5$ (smaller diameter size - distant from main vessel source). The calculations of vessel diameter were performed on the regions identified by dashed squares on *fig.* 7.12 **a** and **b**. *Figure* 7.12 **c-e** demonstrates how the identification and the measurement of the lateral profile of the vessel was performed. After selecting and identifying the branching of a particular vessel, a measurement of the diameter on different points perpendicular to the vessel orientation is performed. In figure 7.12 **f** and **g** a plot of the mean diameter with respect to the branching order for each region of interest is presented, and shows the capability to record up to 5 branches of vessels with diameters ranging from $70\,\mu\mathrm{m}$ up to $250\,\mu\mathrm{m}$.

7.3.3. Exogenous contrast agent detection in cancer tumor models

An orthotopic $4T1$ tumor model was scanned on day 14 post-inoculation (1 million tumor cells) in order to asses the system ability to resolve exogeneously injected agents. The tumor was implanted on the ventral side of the animal, in the mammalian pad. *Figure* 7.13 **a** depicts the MIP of the top view of the tumor mass, 1 hour after the injection of gold nanoparticles. The anatomical image is depicted in gray, while the gold detection is depicted in yellow colormap. *Figure* 7.13 **b** shows a high magnification view of the periphery of the tumor (identified by a square box on *fig.* 7.13 **a**), where the tumor margins (squared lines) and several vessels (arrow) can be distinguished. The high-magnification allows the
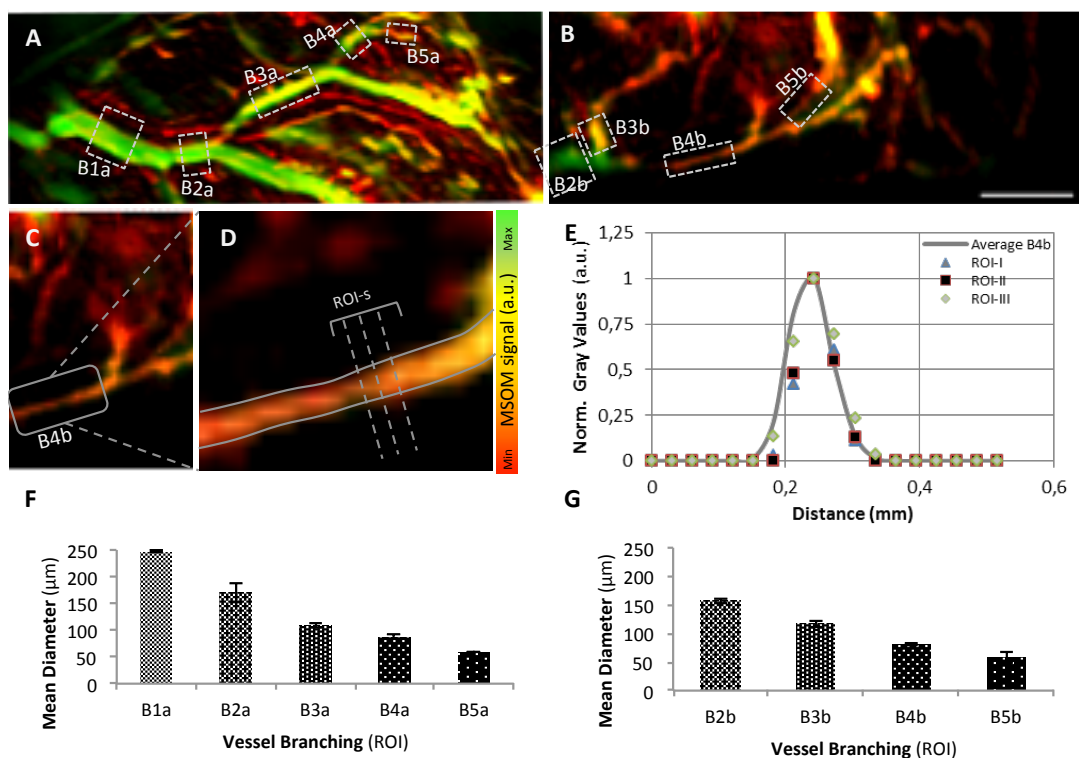
Figure 7.12.: Vascular metrics on *in-vivo* OA tumor imaging: (**a** & **b**) show the vascular network of different regions of the tumor acquired 11 days after inoculation of the cells. On each panel, the successive branching order of the vessels was identified from $B1$ to $B6$. (**c**) Represents a zoom-in of a region integrating the vessel branch $B4$ from panel B. To calculate the mean vessel diameter, different position of the vessel were identified and measured perpendicularly to the vessel orientation (**d**). The lateral profile of the vessel (**e**) and mean vessel diameter were computed. (**f** & **g**) depict the mean diameter according to branching order on each field of view identified as dashed squares on **a** and **b**.

identification of further interaction between vasculature and tumor mass: two large vessels (one identified as B1) extending from the periphery of the tumor interacting with the tumor mass and branching into smaller vessels B2. B1 represented one of the feeding vessels that provide blood supply to the tumor mass, while B2a and B2b represent two examples of smaller vessels resulting from the initial B1 branching. The identification of the two large vessels was also confirmed with H&E staining and ultramicroscopy (*fig.* 7.14). On *fig.* 7.13 **c**, the same magnified view is presented, and the colormap encodes different structures resolved by means of endogenous contrast. The green colormap translates bigger sized vessels, while smaller vasculature, present deep inside the tumor mass is encoded in red. The same region visualized under high-magnification on *fig.* 7.13 **b** was further analyzed to assess functional and molecular patterns. *Figure* 7.13 **d** shows an oxygenation map where highly oxygenated regions (red color) are co-localized with the prominent vessel-like structure identified in *fig.* 7.13 **b**. Deoxygenated regions, mainly located within the tumor mass were identified and are highlighted in blue. In *fig.* 7.13 **e**, the identification of the vessels within the tumor mass were based on the un-mixing of external reporter probe - the gold nanoparticles, vasculature reporter probe, predictable to be located in the vasculature up to 1-hour post injection [9]. As expected, the results show that AuNR particles were located within the vessels. In *fig.* 7.13 **f**, the lateral profile of the vessel labeled $B1$ is presented and the mean diameter is determined to be $250\,\mu m$. *Figure* 7.13 **g** plots the mean diameter values obtained on three different vessels ($B1$, $B2a$ and $B2b$), confirming the values expected for either main feeding vessels - $B1$ (around $250\,\mu m$) and smaller but detectable "branched" vessels (around $70\text{-}150\,\mu m$).
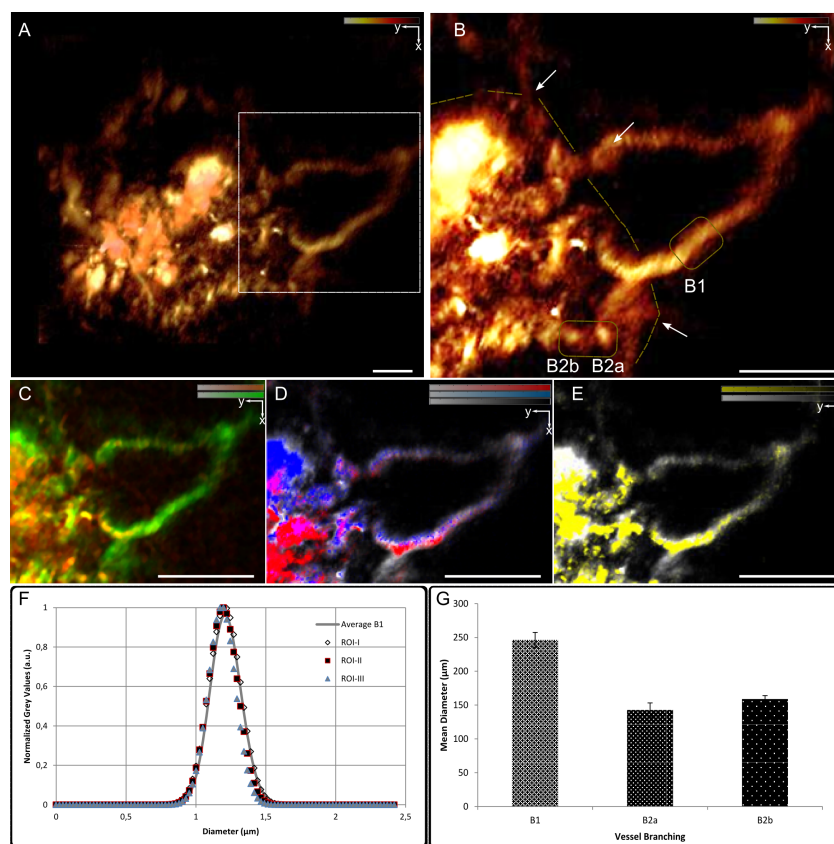
Figure 7.13.: *In-vivo* imaging of exogeneously injected contrast agent: (**a**) MIP (2D) of the top view of the tumor mass, 1 hour after injection with a vascular marker - gold nanoparticles. (**b**) High magnification of dashed square selected in **a**. tumor margins are delimited by square line and "feeding" vasculature identified with a asterisk. (**c**) Same regions as **b** was further presented after size filtering (**c**), un-mixing of oxy/deoxy hemoglobin (**d**) and un-mixing of Gold Nanoparticles (**e**). (**f**) the lateral profile of the vessel $B1$ after Gaussian curve fitting. (**g**) Mean diameter of 3 vessels identified on **b**.

For validation purposes, after the optoacoustic experimental procedure, the tumor was excised, chemically cleared, and scanned using an ultramicroscopy method, as described in section 2.6. *Figure* 7.15 **a** shows a top-view MIP of the tumor, where the vasculature is color-coded in red, while the autofluorescence channel is coded in green. It can be observed that the core of the tumor is rather free of vasculature, while big and small vasculature is present on the periphery. The same results are depicted in the H&E slides, presented on the panels *fig.* 7.15 **b** - **d**, where vessels are present only on the sides of the cross-sections, and the core of the tumor is affected by necrosis. A similar view is depicted

in *fig.* 7.14 **b**, where two major distinct vessels can be seen providing vascular
supply to the inner core of the tumor. *Figure* 7.14 **a** corresponds to a lateral
view of the tumor, and is visualized as an MIP. There can be seen two major
vessels branchings feeding the core of the tumor. In *fig.* 7.14 **c** and **d** an H&E
slice, selected at the base of the tumor, is presented, together with a magnified
view. For comparison reasons in **fig.** 7.14 **e** and **f**, ultramicroscopy results of the
visualized vasculature are presented.
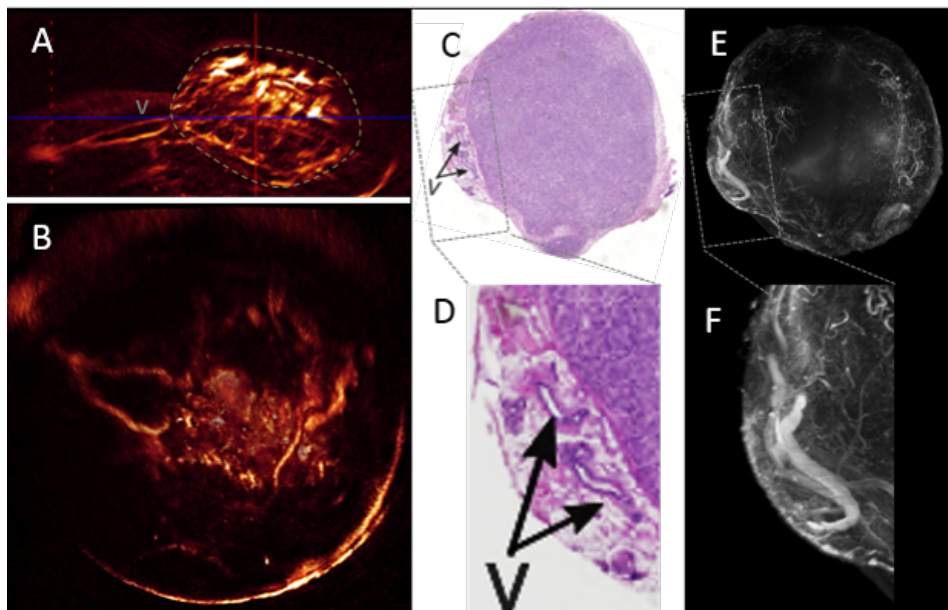
Figure 7.14.: Orthotopic 4T1 tumor model monitored by MSOM. (**a-b**) 2D MIP lateral
and bottom view of the tumor mass by MSOM, respectively. (**c**) H&E staining of a coro-
nal section of the tumor. (**d**) High magnification of the H&E staining at the periphery
of the tumor. (**e**) Ultramicroscopy of a coronal volume of the tumor. (**f**) High magnifi-
cation of the Ultramicroscopy at the periphery of the tumor. A detailed visualization of
the main feeding vessels of the tumor is identified in all panels by (v).

7.3.4. Discussion

The ability to accurately visualize vasculature in the vicinity and within tumor
mass with high spatial resolution is of critical importance for understanding
vascular structure, function and angiogenesis of tumors, as well as on the mon-
itoring of anti-angiogenesis treatment response [130, 131, 132]. While optoa-
coustic technology has been applied so far in several preclinical cancer stud-
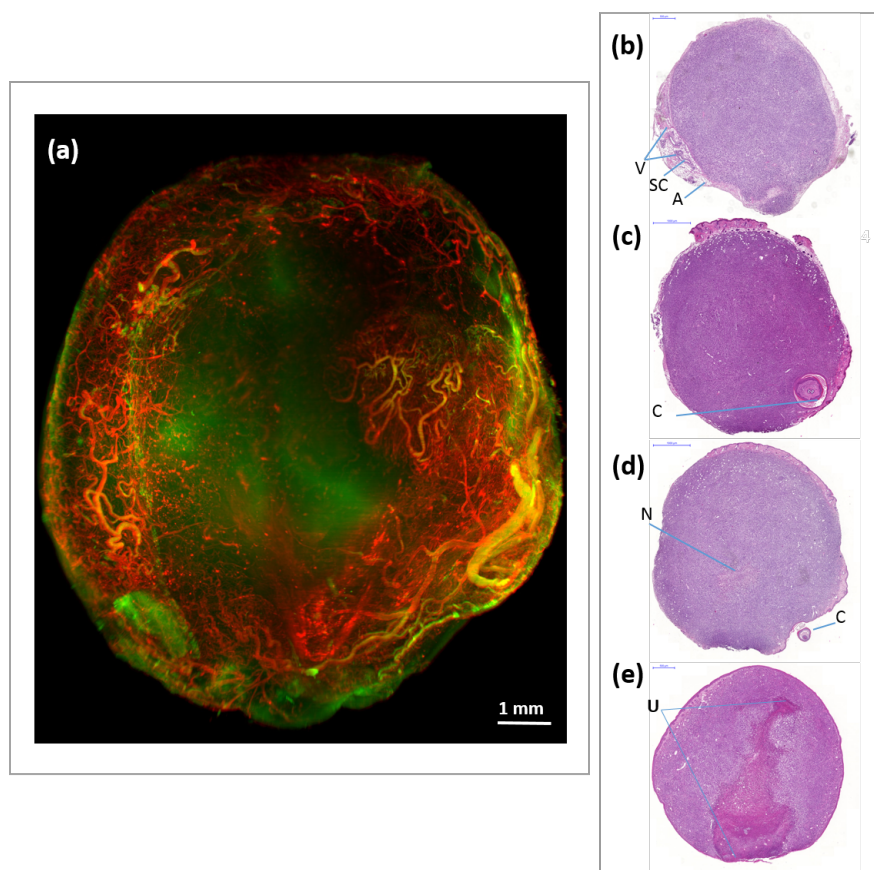
Figure 7.15.: Ultramicroscopy and H&E validation of the orthotopically implanted tumor. (**a**) MIP view of the ultramicroscopy results. Red - channel corresponding to the Lectin680, marker for vasculature imaging, and green - channel of the autofluorescence. (**b**) - (**e**) 2D H&E stained slices corresponding to different levels through the tumor: from body (**b**) to tip of the tumor (**e**). Legend: V - vessels; SC - sebaceous glands and ducts; A - Adipose tissue; c - cyst; N - necrotic area; U - ulcus.

ies [9, 144, 34], most of these investigations had to restrict to superficial imaging and single wavelengths acquisition, being unable to observe the dynamics of vasculature in whole tumor volume [24, 139]. Herein, we introduced a novel scanning geometry, based on the translate-rotate detecting modality for *in-vivo* imaging of tumor vasculature. We show that the combination of a high-frequency linear transducer with an optimal arrangement of detector positions can provide the ability to image the entire tumor mass, as large as $1\,\mathrm{cm}^3$ with a nearly homogeneous spatial resolution of $70\,\mu\mathrm{m}$. By operating on a continuous acquisition routine the system provides scanning times in the order of 10

minutes per wavelength, enabling the acquisition of multispectral datasets, in a
non-invasive and volumetric fashion, of anatomical and functional information
from living samples.

In order to compare the current state-of-the-art in optical imaging for cancer,
an overview of different tumors models analyzed throughout this work is pre-
sented in the context of ultramicroscopy imaging. Ultramicroscopy provides
resolution numbers of $< 10\,\mu m$ and the capacity to perform true volumetric
imaging by virtual sectioning of the sample. *Figure* 7.16 shows an overview
of ultramicroscopy results performed on different tumor models at different
tumor growth stages [2]. Briefly summarizing, the animals followed the proto-
col presented in section 2.6, where 15 minutes before euthanasia a Lectin injec-
tion was administered, for enhancing the vascular visualization in the imaging
stage. In *fig.* 7.16 **a**, a KPL4 orthotopic tumor model scanned 33 days post inoc-
ulation is presented. It can be seen that the tumor presents a high-vessel density
within the entire tumor. Moreover, as a general observation, it can be seen that
the average vessel diameter is rather constant and no major vasculature can be
observed in the ultramicroscopy dataset. For comparison reasons, in *fig.* 7.16
d, the same tumor model at 25 days post-inoculation is presented. It can be ob-
served that the level of vascular density is much lower compared to the tumor
displayed in panel **a**. Two additional tumor models are presented in *fig.* 7.16
b and **c**, where an MDA and a 4T1 tumor model are displayed. It can be seen
that the MDA tumor model does not contain an increased level of vasculature.
The 4T1 tumor model contains some vascular features inside the tumor core,
while the outside boundary presents strong absorbing tissue, which might be a
reason of increased vasculature, sized below the resolution capabilities of this
ultramicroscopy implementation. Although all tumor models were mammary
cancer models, only the KPL4 and MDA are human cell-lines, while the 4T1
is a mouse model. The observations are two fold: on one hand it can be seen
that the same tumor model, implanted on different animals, around the same
development stage, will present a different level of vascularization. This inter-
subject variation patterns are well known aspects of cancer vascularization and
have been previously reported [142]. On the other hand, it can seen that dif-
ferent tumor models present a different level of vascularization, as well as a
particular displacement of vessels around and inside the tumor core. Moreover,
the entire chemical procedure the tumors undergo, combined with the excision
and preparation phases, will hinder the ability to understand the real tumoral
environment, by possibly destroying vessels and altering tissue properties.

Based on the previous observation, we propose the currently introduced sys-

---

[2]Experimental acquisition performed in collaboration with Dr. Annette Feuchtinger
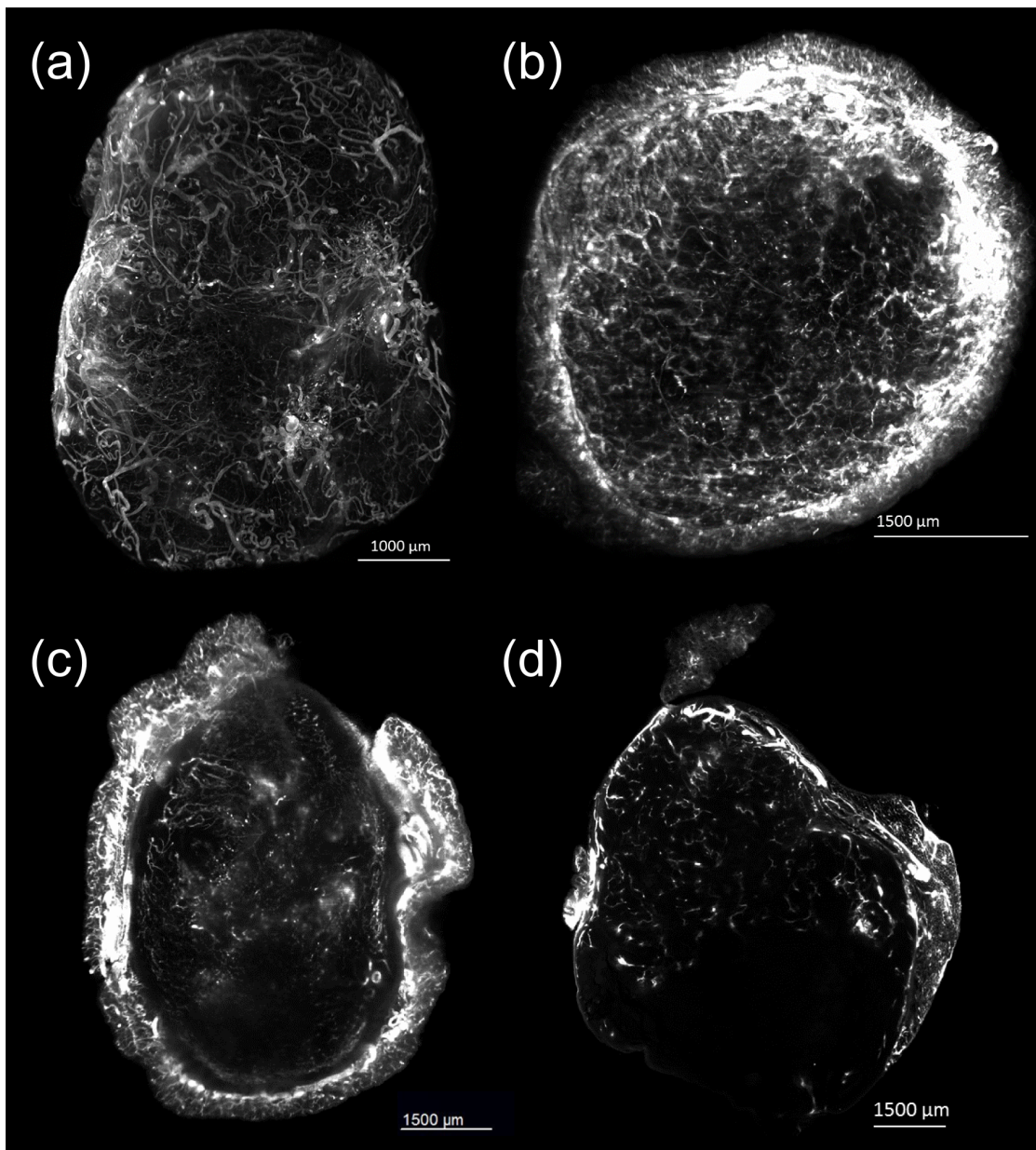
Figure 7.16.: Ultramicroscopy of different orthotopic cancer tumor models. MIP of the Lectin680 channel corresponding to (**a**) KPL4 tumor model, (**b**) MDA tumor model, (**c**) 4T1 xenograft and (**d**) KPL4 tumor model.

tem to offer a new perspective on studying entire volumetric samples at meso-scopic resolution. The scanning geometry allows a broad angle of detection and

true volumetric recording of the OA signals generated deep into tissue. This feature constitutes an advantage over previously introduced optoacoustic systems using a single element detector to record the pressure signals, which are limited in terms of access around the sample, and impractical for full three-dimensional imaging due to the long required scanning times. Moreover, in the case of longitudinal studies, compared to systems that record only a cross-section of the sample under investigation, MSOM can provide full-view visualization of the entire sample, removing the challenging procedure of consistently choosing the same 2D plane. The geometry presented in chapter 5, used a cylindrical geometry to extract anatomical and functional information from excised samples, but due to the enclosed angle, the sample under investigation could measure not more than $12\,\mathrm{mm}$. This geometry fulfilled the full-view in-plane criterion, but was only applied to *ex-vivo* studies, due to the accessibility constraints around the sample. In the present chapter, by including an inclination angle of the transducer along the long axis, we generate a conical detection surface, enabling a larger detection surface. By tilting the linear array, a degradation of the in-plane resolution is observed, while overall resolution numbers tend to become homogeneous. The current implementation of the translate-rotate geometry introduces an optimal balance between the field of view necessary for *in-vivo* tumor imaging and resolution performance.

To evaluate the newly developed MSOM's ability to provide volumetric imaging of entire tumors with high spatial resolution we performed a number of *in-vivo* experiments in mice. Initially, we investigated vascular distribution in 4T1 subcutaneous mouse model. We reconstructed the volumetric dataset and we identified a range of large vessels in the margins of the tumor, as well as thinner vasculature within the tumor mass. Optoacoustic-based visualization of detailed vasculature in the vicinity of tumor margins or mouse body was previous reported by other studies, however, in-depth visualization of tumor vasculature in three dimensions with sub $70\,\mathrm{\mu m}$ resolution, has not yet been presented so far. In our results, in addition to the superficial vasculature, we have also identified a number of smaller vessels and sequential branching inside the tumor mass *in-vivo*. In the following, we studied the MSOM performance for measuring vessel diameter and identifying vessel branching order within *in-vivo* tumors. Vessel diameter measurements were consistently performed in different tumor regions on two different tumor models: mammalian implanted and subcutaneous implanted 4T1 tumor models. We have shown vascular imaging deep inside the tumor and the possibility of tracking up to 5 vessel branches in several regions. To validate the data obtained *in-vivo*, we applied *ex-vivo* validation techniques (H&E and ultramicroscopy) on tumor slices and spatially correlated

this information with the MSOM data. In both tumor models studied, a similar pattern was observed, with a more prominent identification of vessels and their branches in the periphery of the tumor mass. This was further confirmed by ultramicroscopy and H&E staining of 4T1 orthotopic tumors, where the core of the tumor comprised vital tumor cells with low density of small vessels, or necrotic tissue, whereas regions on the edge of the tumor contain adipose tissue with glands and main vessels (*fig.* 7.14). These vessels are key elements to support the tumor angiogenesis, which is characterized by inefficient vascular network formation [130]. These newly formed vessels are effectively endothelial cell tubes, which lack well-developed wall structures and exhibit a limited capacity for blood flow. Finally, we successfully extracted functional parameters (vessel oxygenation and nanoparticle distribution), by multispectral analysis of endogenous and exogenous reporter probes for tumor vasculature imaging. MSOM could resolve and analyze *in-vivo* specific signals for blood oxygenation and gold nanoparticle contrast agents upon multiple wavelength acquisition. Currently, the system's temporal resolution is limited by the pulse repetition rate (PRL) of the OPO laser used in this study. Nevertheless, an increased PRL would present several benefits from a reduced acquisition time enabling monitoring of faster biological processes, to increase resolution and more accurate ultrasonic detection at the cost of broader scanning ranges, exceeding 180 degrees. Finally, apart from the inherent spatial and temporal resolution, the combination of tissue and probe information achieved by multispectral acquisition will prove useful for future studies on tumor distribution and cancer heterogeneity mapping.

7.4. Conclusion

The reported imaging system widens the application range for optoacoustic technology revealing detailed high-fidelity *in-vivo* imaging of tumor vasculature. We present a conical geometry enabling the ability of multispectral mesoscopic setups to volumetrically image entire tumor mass *in-vivo*, overcoming a longstanding challenge. Throughout the current work, initial proof of concept was provided by using a low-frequency 6 MHz transducer. Initial conical data analysis and tumor imaging was performed using this transducer array. After the validation of the concept, the system was further altered to include the high-frequency (24 MHz) linear array, providing a higher resolution and better matched to the task of *in-vivo* tumor vascularization imaging. From a technological perspective, we have characterized the system using both transducer

arrays, and we have concluded on the resolution and field of view capacity. From an application point of view, the developed system was used to present the results of imaging different tumor models implanted in different positions, orthotopically, on the mammalian fat pad, or subcutaneously injected on the dorsal surface of the animal. Based on the extracted vascular networks we trace several branching orders, and we computed vessel metrics. Moreover, multispectral acquisitions allowed the detection and identification of endogenous and exogenous optoacoustic contrast sources for tumor vasculature imaging. Overall, the high resolution and good tissue penetration depth of MSOM provides the ability to extract unique insight on neovasculature studies, potentially driving future investigations into the heterogeneous aspects of murine tumors.

Chapter 8.

Conclusion and Future outlook

The work presented in this thesis, describes the efforts and outcomes performed in the context of optoacoustic imaging using linear array transducers covering a broad range of recorded frequencies. The work presents the design, implementation and characterization of three different optoacoustic systems using linear arrays scanned in different configurations. The main objective of this efforts was to provide adequate mesoscopic imaging systems able to answer complex biological questions in the context of small-animal imaging in the preclinical phase.

The reported work aims at providing imaging tools for biological observations of samples in the mesoscopic regime, where classic microscopy techniques are severely affected by the light scattering in tissue. The first detection geometry is presented in chapter 4, where a high-frequency linear array is used to detect optoacoustic signals generated by a sample translated through a thin plane of illumination. The geometry was implemented in the context of a selective plane illumination microscope (SPIM). The advantages of using such a system are two fold: on one hand, the same sample can be observed throughout several of it's development stages, using two different imaging techniques: the microscopy approach can image the sample in the infant stages, when the sample is relatively small in size, and transparent, while the optoacoustic technique can be used in later evolution stages, when the samples become opaque. Moreover, along the same lines, the advantage of combining both these modalities will render in a complementarity of contrasts and biomarker detection. The second advantage this implementation provided, was the ability to use linear arrays in a translation geometry, with good resolution in the translation direction, due to the light confinement in a plane. This was due to the thin plane of illumination, co-aligned with the detection plane of the array, along which, in standard broad illumination geometries, the resolution is severely deteriorated. The system enabled simultaneously co-registration of SPIM and OA data at single time point, and is expected to be further modified and used in observing

and tracking living organisms throughout their evolutionary stages.

The first system was however unable to maintain this enhanced resolution for strongly scattering tissue. For scattering tissue, a simple translation of the array results in a single side detection and to limited view and resolution artifacts. In order to mitigate the artifacts introduced by a single sided detection and to increase the size of the imaged objects, in chapter 5, the proposed tomographic geometry accounted for the geometrical properties of the sensitivity patterns of linear arrays. The array was translated and rotated around the sample of interest, in order to record optoacoustic signals. The geometry was implemented using two different linear arrays, and had successfully imaged in an *ex-vivo* state an entire mouse and other small animal organs. By using two arrays, with different central frequencies, the system achieved the ability to combine complementary information provided by two separate frequency bands. Moreover, the enhanced detection capabilities over a broad range of frequencies was performed with a resolution of up to $30\,\mu m$ in intact samples sized up to $1\,cm^3$ (using the high-frequency array), and up to $120\,\mu m$ resolution in samples sized up to $4\,cm^3$. In chapter 6, the broadband capabilities of the system have been used to report first time insights, by using optical imaging modalities, into 3D visualization of exogeneously administered agent detection in intact, non-processed biological samples, with resolution of down to $30\,\mu m$.

The third implementation presented in this thesis is detailed in chapter 7, where the translate-rotate geometry is employed in the context of cancer imaging in small animals. *In-vivo* imaging of cancerous tumors is achieved by translating the previous scanning geometry into a cone shape like arrangement of detectors around the sample. By combining algorithmic developments on optimal frequency visualization techniques using single detector arrays, with modalities of compensating for sound attenuation in tissue at high-frequencies, homogeneous resolution 3D multispectral OA images in the mesoscopic regime was reported. In the context of cancer imaging the system was used to record anatomical, functional and molecular information recorded from *in-vivo* subcutaneous and orthotopic tumor models implanted on laboratory mice. Further optimization of the detector frequency is expected to provide additional details in tumor uptake, metabolization and cancer therapy based on exogeneously injected agents.

The future hardware improvements as well as from an application development point of view the outlook perspective could be summarized on four different levels:

1. Acoustic detection: Detector frequency and specifications (focusing distance and number of elements) matched to the envisioned application,

combined with the detection geometries presented in this work, will enable optimal image quality and visualization with respect to the the desired outcome. Furthermore, given the fast pace of developments in the hardware of ultrasound imaging, we expect the possibility to use detectors with technology capabilities of higher sensitivity over a broader of frequencies. Furthermore, improvements on the detection geometry and sensitivity of the elements will possibly reduce the necessary number of scanning positions, further reducing the acquisition time, and implicitly simplifying the reconstruction phase.

2. Optical excitation: Faster repetition rate lasers, combined with fast tuning capabilities, will considerably reduce the acquisition time, opening up a much wider range of applications. Currently available, 100 Hz lasers will reduce the scanning time by 10 times. Furthermore, innovative positioning of the illumination bundles, without blocking the transducer array's view, or fibers with a smaller foot print, would allow a broader coverage of the detection aperture, resulting in an improved image quality.

3. Signal and image processing: Improvements on the reconstruction methods taking into account the sensitivity and particular size and geometry of the transducer elements will generate higher quality images. Additionally, a modeling of the detector shape during the reconstruction phase, would enable a reduction in detector positions during the scanning, at the expense of computationally intensive post-processing. Further improvements on the unmixing and visualization of data-sets will enable a better understanding of the biological processes recorded by the system. An improved volumetric visualization of the reconstructed data-sets will open the way to a variety of image processing modalities. Parameters regarding the accurate volume occupied by a dye, or tracing and extracting quantification details regarding the complexity and tortosity of the vascular networks can further enrich the information provided by using these systems.

4. Biological question: Based on the current modularity of the proposed systems, depending on the biological process and question to be monitored, different ultrasound detectors and lasers can be used by easily interchanging the components. The volumetric capabilities of the system, combined with the good resolution and multispectral abilities will open up the possibility of answering complex biological questions.

From a final perspective, throughout the work presented in this thesis, several significant conclusions regarding optoacoustic imaging implemented using linear arrays are to be noted, both from a hardware perspective, as well as from an application point of view.

From a detection perspective, we consider linear arrays as adequate detectors for optoacoustic imaging and combined with fast acquisition cards, they can provide parallel acquisition of optoacoustic signals. Furthermore, additional care must be taken in deciding on a detection geometry by considering their properties and characteristics. In addition to the geometrical specifications of the array, defining their sensitivity patterns, the emission characteristics of absorbing structures and their directivity must be taken into account. In the current work, we proposed three different approaches, with their strengths and limitations, but in general, the envision application together with the biological and hardware limitations will dictate the detection geometry to be used in a special situation.

From an application perspective, we have to note that linear arrays are characterized by their central frequency, and although they record a broad range of frequencies, they are much more sensitive around the central nominal value. In optoacoustic imaging, different sized structures will emit different frequencies. Attaining a complete picture of the biological underling processes requires a broadband detection of optoacoustic signals. A demonstration of the importance of broadband optoacoustic signal detection, from a hardware perspective, has reveled the ability to detect the complex distribution patterns of two differently localized contrast agents. Moreover, in respect to *in-vivo* imaging of subcutaneous and orthotopic cancer tumors in the current work the focus laid on imaging the vascular networks and their distribution patterns in different models. Based on the findings presented in this thesis, with respect to tumor imaging combined with adequate frequency considerents previously discussed, we consider highly appropriate to conclude that suitable applications including dynamic visualization on targeted agents, coupled with the right detection geometry and frequency, will provide a valuable tool in cancer imaging.

Appendix A.

List of publications

- **Andrei Chekkoury**[*], Antonio Nunes[*], Jerome Gateau, Panagiotis Symvoulidis, Annette Feuchtinger, Nicolas Beziere, Saak V. Ovsepian, Axel Walch and Vasilis Ntziachristos - *"High Resolution Multispectral Optoacoustic Tomography of the Vascular System and Constitutive Hypoxemia of Cancerous Tumors"* - in preparation

- **Andrei Chekkoury**, Jérôme Gateau, Wouter Driessen, Panagiotis Symvoulidis, Nicolas Bèziére, Annette Feuchtinger, Axel Walch, and Vasilis Ntziachristos - *"Optical mesoscopy without the scatter: broadband multispectral optoacoustic mesoscopy"* published in Biomedical Optics Express, Vol. 6, Issue 9, (July 2015) [15].

- Hsiao-Chun Amy Lin[*], **Andrei Chekkoury**[*], Murad Omar[*], Tobias Schmitt-Manderbach, Benno Koberstein-Schwarz, Timo Mappes, Hernán López-Schier, Daniel Razansky and Vasilis Ntziachristos - *"Selective plane illumination optical and optoacoustic microscopy for postembryonic imaging"* published in Laser &

Photonics Reviews (September 2015) [102].

- Amir Rosenthal, Stephan Kellnberger, Dmitry Bozhko, **Andrei Chekkoury**, Murad Omar, Daniel Razansky, and Vasilis Ntziachristos - "Sensitive interferometric detection of ultrasound for minimally invasive clinical imaging applications" in Laser and Photonics Reviews, 8(3), 450-457 (March 2014) [123]

- Jérôme Gateau, **Andrei Chekkoury** and Vasilis Ntziachristos - "*Ultra-wideband three-dimensional optoacoustic tomography*" published in Optics Letters, Vol. 38, No. 22, (November 2013)[115]

- Jérôme Gateau, **Andrei Chekkoury** and Vasilis Ntziachristos - "*High-resolution optoacoustic mesoscopy with a* 24 *MHz multidetector translate-rotate scanner*" published in the Journal of Biomedical Optics 18(10), 106005, (October 2013) [111].

- **Andrei Chekkoury**, Jérôme Gateau and Vasilis Ntziachristos - "Multiple bandwidth volumetric optoacoustic tomography using conventional ultrasound linear arrays" in Proceedings of SPIE - European Conferences on Biomedical Optics (June 2013), [145]

---

* equal contribution

List of Figures

List of Tables

Bibliography

[1] Ralph Weissleder and Mikael J Pittet. Imaging in the era of molecular oncology. *Nature*, 452(7187):580–589, 2008.

[2] Vasilis Ntziachristos. Going deeper than microscopy: the optical imaging frontier in biology. *Nature methods*, 7(8):603–614, 2010.

[3] Angelique Ale, Vladimir Ermolayev, Eva Herzog, Christian Cohrs, Martin Hrabé de Angelis, and Vasilis Ntziachristos. Fmt-xct: in vivo animal studies with hybrid fluorescence molecular tomography-x-ray computed tomography. *Nature methods*, 9(6):615–620, 2012.

[4] David Boas, Dana H Brooks, Eric L Miller, Charles DiMarzio, Misha Kilmer, Richard J Gaudette, Quan Zhang, et al. Imaging the body with diffuse optical tomography. *Signal Processing Magazine, IEEE*, 18(6):57–75, 2001.

[5] Hao F Zhang, Konstantin Maslov, George Stoica, and Lihong V Wang. Functional photoacoustic microscopy for high-resolution and noninvasive in vivo imaging. *Nature biotechnology*, 24(7):848–851, 2006.

[6] George J Tserevelakis, Dominik Soliman, Murad Omar, and Vasilis Ntziachristos. Hybrid multiphoton and optoacoustic microscope. *Optics letters*, 39(7):1819–1822, 2014.

[7] Vasilis Ntziachristos, Jorge Ripoll, Lihong V Wang, and Ralph Weissleder. Looking and listening to light: the evolution of whole-body photonic imaging. *Nature biotechnology*, 23(3):313–320, 2005.

[8] Xueding Wang, Yongjiang Pang, Geng Ku, Xueyi Xie, George Stoica, and Lihong V Wang. Noninvasive laser-induced photoacoustic tomography for structural and functional in vivo imaging of the brain. *Nature biotechnology*, 21(7):803–806, 2003.

[9] Eva Herzog, Adrian Taruttis, Nicolas Beziere, Andrey A Lutich, Daniel Razansky, and Vasilis Ntziachristos. Optical imaging of cancer heterogeneity with multispectral optoacoustic tomography. *Radiology*, 263(2):461–468, 2012.

[10] Xosé Luís Deán-Ben, Steven James Ford, and Daniel Razansky. High-frame rate four dimensional optoacoustic tomography enables visualization of cardiovascular dynamics and mouse heart perfusion. *Scientific reports*, 5, 2015.

[11] Neal C Burton, Manishkumar Patel, Stefan Morscher, Wouter HP Driessen, Jing Claussen, Nicolas Beziere, Thomas Jetzfellner, Adrian Taruttis, Daniel Razansky, Bohumil Bednar, et al. Multispectral opto-acoustic tomography (msot) of the brain and glioblastoma characterization. *Neuroimage*, 65:522–528, 2013.

[12] Shriram Sethuraman, Salavat R Aglyamov, James H Amirian, Richard W Smalling, and Stanislav Y Emelianov. Intravascular photoacoustic imaging using an ivus imaging catheter. *Ultrasonics, Ferroelectrics, and Frequency Control, IEEE Transactions on*, 54(5):978–986, 2007.

[13] Joon-Mo Yang, Christopher Favazza, Ruimin Chen, Junjie Yao, Xin Cai, Konstantin Maslov, Qifa Zhou, K Kirk Shung, and Lihong V Wang. Simultaneous functional photoacoustic and ultrasonic endoscopy of internal organs in vivo. *Nature Medicine*, 18(8):1297–1302, 2012.

[14] Robert A Kruger, Richard B Lam, Daniel R Reinecke, Stephen P Del Rio, and Ryan P Doyle. Photoacoustic angiography of the breast. *Medical physics*, 37(11):6096–6100, 2010.

[15] Andrei Chekkoury, Jérôme Gateau, Wouter Driessen, Panagiotis Symvoulidis, Nicolas Bézière, Annette Feuchtinger, Axel Walch, and Vasilis Ntziachristos. Optical mesoscopy without the scatter: broadband multispectral optoacoustic mesoscopy. *Biomed. Opt. Express*, 6(9):3134–3148, Sep 2015.

[16] Claudio Vinegoni, Chrysoula Pitsouli, Daniel Razansky, Norbert Perrimon, and Vasilis Ntziachristos. In vivo imaging of. *Nature Methods*, 5(1):45, 2008.

[17] Piper M Treuting and Suzanne M Dintzis. *Comparative Anatomy and Histology: A Mouse and Human Atlas (Expert Consult)*. Academic Press, 2011.

[18] FJB Sampaio and AHM Aragao. Anatomical relationship between the intrarenal arteries and the kidney collecting system. *J Urol*, 143(4):679–681, 1990.

[19] Michael Marxen, Michael M Thornton, Cameron B Chiarot, Giannoula Klement, Janet Koprivnikar, John G Sled, and R Mark Henkelman. Microct scanner performance and considerations for vascular specimen imaging. *Medical physics*, 31(2):305–313, 2004.

[20] Hans-Ulrich Dodt, Ulrich Leischner, Anja Schierloh, Nina Jährling, Christoph Peter Mauch, Katrin Deininger, Jan Michael Deussing, Matthias Eder, Walter Zieglgänsberger, and Klaus Becker. Ultramicroscopy: three-dimensional visualization of neuronal networks in the whole mouse brain. *Nature methods*, 4(4):331–336, 2007.

[21] James Sharpe, Ulf Ahlgren, Paul Perry, Bill Hill, Allyson Ross, Jacob Hecksher-Sørensen, Richard Baldock, and Duncan Davidson. Optical projection tomography as a tool for 3d microscopy and gene expression studies. *Science*, 296(5567):541–545, 2002.

[22] Tomas Alanentalo, Amir Asayesh, Harris Morrison, Christina E Lorén, Dan Holmberg, James Sharpe, and Ulf Ahlgren. Tomographic molecular imaging and 3d quantification within adult mouse organs. *Nature methods*, 4(1):31–33, 2007.

[23] Jan Huisken, Jim Swoger, Filippo Del Bene, Joachim Wittbrodt, and Ernst HK Stelzer. Optical sectioning deep inside live embryos by selective plane illumination microscopy. *Science*, 305(5686):1007–1009, 2004.

[24] Jan Laufer, Peter Johnson, Edward Zhang, Bradley Treeby, Ben Cox, Barbara Pedley, and Paul Beard. In vivo preclinical photoacoustic imaging of tumor vasculature development and therapy. *Journal of biomedical optics*, 17(5):0560161–0560168, 2012.

[25] Kwang Hyun Song, Erich W Stein, Julie A Margenthaler, and Lihong V Wang. Noninvasive photoacoustic identification of sentinel lymph nodes containing methylene blue in vivo in a rat model. *Journal of biomedical optics*, 13(5):054033–054033, 2008.

[26] Vasilis Ntziachristos and Daniel Razansky. Molecular imaging by means of multispectral optoacoustic tomography (msot). *Chemical reviews*, 110(5):2783–2794, 2010.

[27] Daniel Razansky, Martin Distel, Claudio Vinegoni, Rui Ma, Norbert Perrimon, Reinhard W Köster, and Vasilis Ntziachristos. Multispectral opto-acoustic tomography of deep-seated fluorescent proteins in vivo. *Nature Photonics*, 3(7):412–417, 2009.

[28] Richard Su, Sergey A Ermilov, Anton V Liopo, and Alexander A Oraevsky. Three-dimensional optoacoustic imaging as a new noninvasive technique to study long-term biodistribution of optical contrast agents in small animal models. *Journal of biomedical optics*, 17(10):1015061–1015067, 2012.

[29] Hans-Peter Brecht, Richard Su, Matthew Fronheiser, Sergey A Ermilov, Andre Conjusteau, and Alexander A Oraevsky. Whole-body three-dimensional optoacoustic tomography system for small animals. *Journal of biomedical optics*, 14(6):064007–064007, 2009.

[30] Robert A Kruger, William L Kiser Jr, Daniel R Reinecke, and Gabe A Kruger. Thermoacoustic computed tomography using a conventional linear transducer array. *Medical physics*, 30(5):856–860, 2003.

[31] Andreas Buehler, Marcin Kacprowicz, Adrian Taruttis, and Vasilis Ntziachristos. Real-time handheld multispectral optoacoustic imaging. *Optics letters*, 38(9):1404–1406, 2013.

[32] Daniel Razansky, Andreas Buehler, and Vasilis Ntziachristos. Volumetric real-time multispectral optoacoustic tomography of biomarkers. *Nature protocols*, 6(8):1121–1129, 2011.

Bibliography

[33] Andreas Buehler, Eva Herzog, Daniel Razansky, and Vasilis Ntziachristos. Video rate optoacoustic tomography of mouse kidney perfusion. *Optics letters*, 35(14):2475–2477, 2010.

[34] Gina F Lungu, Meng-Lin Li, Xueyi Xie, Lihong V Wang, and George Stoica. In vivo imaging and characterization of hypoxia-induced neovascularization and tumor invasion. *International journal of oncology*, 30(1):45–54, 2007.

[35] Geng Ku, Xueding Wang, Xueyi Xie, George Stoica, and Lihong V Wang. Imaging of tumor angiogenesis in rat brains in vivo by photoacoustic tomography. *Applied optics*, 44(5):770–775, 2005.

[36] Xueding Wang, David L Chamberland, Paul L Carson, J Brian Fowlkes, Ronald O Bude, David A Jamadar, and Blake J Roessler. Imaging of joints with laser-based photoacoustic tomography: an animal study. *Medical physics*, 33(8):2691–2697, 2006.

[37] Alexander Graham Bell. On the production and reproduction of sound by light. *American Journal of Science*, (118):305–324, 1880.

[38] BT Cox, JG Laufer, and PC Beard. The challenges for quantitative photoacoustic imaging. In *SPIE BiOS: Biomedical Optics*, pages 717713–717713. International Society for Optics and Photonics, 2009.

[39] GJ Diebold, T Sun, and MI Khan. Photoacoustic monopole radiation in one, two, and three dimensions. *Physical review letters*, 67(24):3384, 1991.

[40] Lihong V Wang and Hsin-i Wu. *Biomedical optics: principles and imaging*. John Wiley & Sons, 2012.

[41] Lihong V Wang. Tutorial on photoacoustic microscopy and computed tomography. *Selected Topics in Quantum Electronics, IEEE Journal of*, 14(1):171–179, 2008.

[42] Changhui Li and Lihong V Wang. Photoacoustic tomography and sensing in biomedicine. *Physics in medicine and biology*, 54(19):R59, 2009.

[43] Bradley E Treeby. Acoustic attenuation compensation in photoacoustic tomography using time-variant filtering. *Journal of biomedical optics*, 18(3):036008–036008, 2013.

[44] X Luís Deán-Ben, Daniel Razansky, and Vasilis Ntziachristos. The effects of acoustic attenuation in optoacoustic signals. *Physics in medicine and biology*, 56(18):6129, 2011.

[45] Yuan Xu, Lihong V Wang, Gaik Ambartsoumian, and Peter Kuchment. Reconstructions in limited-view thermoacoustic tomography. *Medical physics*, 31(4):724–733, 2004.

[46] Alexander H Delaney and Yoram Bresler. Globally convergent edge-preserving regularized reconstruction: an application to limited-angle tomography. *Image Processing, IEEE Transactions on*, 7(2):204–221, 1998.

[47] Xiaochuan Pan and Mark A. Anastasio. Minimal-scan filtered backpropagation algorithms for diffraction tomography. *J. Opt. Soc. Am. A*, 16(12):2896–2903, Dec 1999.

[48] John Gamelin, Andres Aguirre, Anastasios Maurudis, Fei Huang, Diego Castillo, Lihong V Wang, and Quing Zhu. Curved array photoacoustic tomographic system for small animal imaging. *Journal of biomedical optics*, 13(2):024007–024007, 2008.

[49] Alfred K Louis and Eric Todd Quinto. *Local tomographic methods in Sonar*. Springer, 2000.

[50] Mark A Anastasio and Jin Zhang. Image reconstruction in photoacoustic tomography with truncated cylindrical measurement apertures. In *Biomedical Optics 2006*, pages 608610–608610. International Society for Optics and Photonics, 2006.

[51] G Paltauf, R Nuster, and P Burgholzer. Weight factors for limited angle photoacoustic tomography. *Physics in medicine and biology*, 54(11):3303, 2009.

[52] Xiaochuan Pan, Yu Zou, Mark Anastasio, et al. Data redundancy and reduced-scan reconstruction in reflectivity tomography. *Image Processing, IEEE Transactions on*, 12(7):784–795, 2003.

[53] G Paltauf, R Nuster, M Haltmeier, and P Burgholzer. Experimental evaluation of reconstruction algorithms for limited view photoacoustic tomography with line detectors. *Inverse Problems*, 23(6):S81, 2007.

[54] Robert A Kruger, Pingyu Liu, C Robert Appledorn, et al. Photoacoustic ultrasound (paus)-reconstruction tomography. *Medical physics*, 22(10):1605–1609, 1995.

[55] Liangzhong Xiang, Bin Han, Colin Carpenter, Guillem Pratx, Yu Kuang, and Lei Xing. X-ray acoustic computed tomography with pulsed x-ray beam from a medical linear accelerator. *Medical physics*, 40(1):010701, 2013.

[56] Daniel Razansky, Stephan Kellnberger, and Vasilis Ntziachristos. Near-field radiofrequency thermoacoustic tomography with impulse excitation. *Medical physics*, 37(9):4602–4607, 2010.

[57] Amit P Jathoul, Jan Laufer, Olumide Ogunlade, Bradley Treeby, Ben Cox, Edward Zhang, Peter Johnson, Arnold R Pizzey, Brian Philip, Teresa Marafioti, et al. Deep in vivo photoacoustic imaging of mammalian tissues using a tyrosinase-based genetic reporter. *Nature Photonics*, 2015.

[58] Stéphane Michau, Pascal Mauchamp, and Rémi Dufait. Piezocomposite 30mhz linear array for medical imaging: design challenges and performances evaluation of a 128 elements array. In *Ultrasonics Symposium, 2004 IEEE*, volume 2, pages 898–901. IEEE, 2004.

[59] Ioanna G Mina. *High frequency transducers from PZT films*. PhD thesis, Pennsylvania State University, 2007.

[60] Srikant Vaithilingam, Te-Jen Ma, Yukio Furukawa, Ira O Wygant, Z Xuefeng, Adam De La Zerda, Omer Oralkan, Aya Kamaya, R Brooke Jeffrey, Butrus T Khuri-Yakub, et al. Three-dimensional photoacoustic imaging using a two-dimensional cmut array. *Ultrasonics, Ferroelectrics, and Frequency Control, IEEE Transactions on*, 56(11):2411–2419, 2009.

[61] Sri-Rajasekhar Kothapalli, Te-Jen Ma, Srikant Vaithilingam, Ömer Oralkan, Butrus T Khuri-Yakub, and San-jiv Sam Gambhir. Deep tissue photoacoustic imaging using a miniaturized 2-d capacitive micromachined ultrasonic transducer array. *Biomedical Engineering, IEEE Transactions on*, 59(5):1199–1204, 2012.

[62] Richard Bouchard, Ozge Sahin, and Stanislav Emelianov. Ultrasound-guided photoacoustic imaging: current state and future development. *Ultrasonics, Ferroelectrics, and Frequency Control, IEEE Transactions on*, 61(3):450–466, 2014.

[63] Edward Zhang, Jan Laufer, and Paul Beard. Backward-mode multiwavelength photoacoustic scanner using a planar fabry-perot polymer film ultrasound sensor for high-resolution three-dimensional imaging of biological tissues. *Applied optics*, 47(4):561–577, 2008.

[64] Miguel Angel Araque Caballero, Amir Rosenthal, Andreas Buehler, Daniel Razansky, and Vasilis Ntziachristos. Optoacoustic determination of spatio-temporal responses of ultrasound sensors. *Ultrasonics, Ferroelectrics, and Frequency Control, IEEE Transactions on*, 60(6):1234–1244, 2013.

[65] Miguel Ángel Araque Caballero. *Incorporating Sensor Properties in Optoacoustic Imaging*. PhD thesis, München, Technische Universität München, Diss., 2013, 2013.

[66] Amir Rosenthal, Vasilis Ntziachristos, and Daniel Razansky. Optoacoustic methods for frequency calibration of ultrasonic sensors. *Ultrasonics, Ferroelectrics, and Frequency Control, IEEE Transactions on*, 58(2):316–326, 2011.

[67] Murad Omar, Jérôme Gateau, and Vasilis Ntziachristos. Raster-scan optoacoustic mesoscopy in the 25-125 mhz range. *Optics Letters*, 38(14):2472–2474, 2013.

[68] Rui Ma, Adrian Taruttis, Vasilis Ntziachristos, and Daniel Razansky. Multispectral optoacoustic tomography (msot) scanner for whole-body small animal imaging. *Optics Express*, 17(24):21414–21426, 2009.

[69] Minghua Xu and Lihong V Wang. Universal back-projection algorithm for photoacoustic computed tomography. In *Biomedical Optics 2005*, pages 251–254. International Society for Optics and Photonics, 2005.

[70] Amir Rosenthal, Vasilis Ntziachristos, and Daniel Razansky. Acoustic inversion in optoacoustic tomography: A review. *Current medical imaging reviews*, 9(4):318, 2013.

[71] Jérôme Gateau, Miguel Ángel Araque Caballero, Alexander Dima, and Vasilis Ntziachristos. Three-dimensional optoacoustic tomography using a conventional ultrasound linear detector array: whole-body tomographic system for small animals. *Medical physics*, 40(1):013302, 2013.

[72] Athanasios Sarantopoulos, George Themelis, and Vasilis Ntziachristos. Imaging the bio-distribution of fluorescent probes using multispectral epi-illumination cryoslicing imaging. *Molecular imaging and biology*, 13(5):874–885, 2011.

[73] Bilge Ergin, Stephan Meding, Rupert Langer, Marcel Kap, Christian Viertler, Christina Schott, Uta Ferch, Peter Riegman, Kurt Zatloukal, Axel Walch, et al. Proteomic analysis of paxgene-fixed tissues. *Journal of proteome research*, 9(10):5188–5196, 2010.

[74] Michael Dobosz, Vasilis Ntziachristos, Werner Scheuer, and Steffen Strobel. Multispectral fluorescence ultramicroscopy: three-dimensional visualization and automatic quantification of tumor morphology, drug penetration, and antiangiogenic treatment response. *Neoplasia*, 16(1):1–W7, 2014.

[75] Paul Beard. Biomedical photoacoustic imaging. *Interface focus*, page rsfs20110028, 2011.

[76] Richard B Lam, Robert A Kruger, Daniel R Reinecke, Stephen P DelRio, Michael M Thornton, Paul A Picot, and Timothy G Morgan. Dynamic optical angiography of mouse anatomy using radial projections. In *BiOS*, pages 756405–756405. International Society for Optics and Photonics, 2010.

[77] Robert A Kruger, Cherie M Kuzmiak, Richard B Lam, Daniel R Reinecke, Stephen P Del Rio, and Doreen Steed. Dedicated 3d photoacoustic breast imaging. *Medical physics*, 40(11):113301, 2013.

[78] X Luís Deán-Ben and Daniel Razansky. Portable spherical array probe for volumetric real-time optoacoustic imaging at centimeter-scale depths. *Optics express*, 21(23):28062–28071, 2013.

[79] Daniel Razansky, Claudio Vinegoni, and Vasilis Ntziachristos. Imaging of mesoscopic-scale organisms using selective-plane optoacoustic tomography. *Physics in medicine and biology*, 54(9):2769, 2009.

[80] A Buehler, XL Deán-Ben, J Claussen, V Ntziachristos, and D Razansky. Three-dimensional optoacoustic tomography at video rate. *Optics express*, 20(20):22712–22719, 2012.

[81] Jun Xia, Muhammad R Chatni, Konstantin Maslov, Zijian Guo, Kun Wang, Mark Anastasio, and Lihong V Wang. Whole-body ring-shaped confocal photoacoustic computed tomography of small animals in vivo. *Journal of biomedical optics*, 17(5):0505061–0505063, 2012.

[82] L. Song, K. Maslov, R. Bitton, K. K. Shung, and L. V. Wang. Fast 3-d dark-field reflection-mode photoacoustic microscopy in vivo with a 30-mhz ultrasound linear array. *J Biomed Opt*, 13(5):054028, 2008.

[83] Kwang Hyun Song and Lihong V Wang. Deep reflection-mode photoacoustic imaging of biological tissue. *Journal of biomedical optics*, 12(6):060503–060503, 2007.

[84] Leonardo G Montilla, Ragnar Olafsson, Daniel R Bauer, and Russell S Witte. Real-time photoacoustic and ultrasound imaging: a simple solution for clinical ultrasound systems with linear arrays. *Physics in medicine and biology*, 58(1):N1, 2013.

[85] Andrew Needles, Andrew Heinmiller, John Sun, Catherine Theodoropoulos, David Bates, Desmond Hirson, Melissa Yin, and F Stuart Foster. Development and initial application of a fully integrated photoacoustic microultrasound system. *Ultrasonics, Ferroelectrics and Frequency Control, IEEE Transactions on*, 60(5):888–897, 2013.

[86] Yu Wang, Todd N Erpelding, Ladislav Jankovic, Zijian Guo, Jean-Luc Robert, Guillaume David, and Lihong V Wang. In vivo three-dimensional photoacoustic imaging based on a clinical matrix array ultrasound probe. *Journal of biomedical optics*, 17(6):0612081–0612085, 2012.

[87] Todd N Erpelding, Chulhong Kim, Manojit Pramanik, Ladislav Jankovic, Konstantin Maslov, Zijian Guo, Julie A Margenthaler, Michael D Pashley, and Lihong V Wang. Sentinel lymph nodes in the rat: Noninvasive photoacoustic and us imaging with a clinical us system 1. *Radiology*, 256(1):102–110, 2010.

[88] Liang Song, Chulhong Kim, Konstantin Maslov, K Kirk Shung, and Lihong V Wang. High-speed dynamic 3d photoacoustic imaging of sentinel lymph node in a murine model using an ultrasound array. *Medical physics*, 36(8):3724–3729, 2009.

[89] Laetitia Vionnet, Jérôme Gateau, Mathias Schwarz, Andreas Buehler, Volodymir Ermolayev, and Vasilis Ntziachristos. 24-mhz scanner for optoacoustic imaging of skin and burn. *Medical Imaging, IEEE Transactions on*, 33(2):535–545, 2014.

[90] Alexander Dima, Neal C Burton, and Vasilis Ntziachristos. Multispectral optoacoustic tomography at 64, 128, and 256 channels. *Journal of biomedical optics*, 19(3):036021–036021, 2014.

[91] Adrian Taruttis, Eva Herzog, Daniel Razansky, and Vasilis Ntziachristos. Real-time imaging of cardiovascular dynamics and circulating gold nanorods with multispectral optoacoustic tomography. *Optics express*, 18(19):19592–19602, 2010.

[92] Stefan Morscher, Wouter H.P. Driessen, Jing Claussen, and Neal C. Burton. Semi-quantitative multispectral optoacoustic tomography (msot) for volumetric {PK} imaging of gastric emptying. *Photoacoustics*, 2(3):103 – 110, 2014.

[93] Liang Song, Konstantin Maslov, K Kirk Shung, and Lihong V Wang. Ultrasound-array-based real-time photoacoustic microscopy of human pulsatile dynamics in vivo. *Journal of biomedical optics*, 15(2):021303–021303, 2010.

[94] Matthew P Fronheiser, Sergey A Ermilov, Hans-Peter Brecht, Andre Conjusteau, Richard Su, Ketan Mehta, and Alexander A Oraevsky. Real-time optoacoustic monitoring and three-dimensional mapping of a human arm vasculature. *Journal of biomedical optics*, 15(2):021305–021305, 2010.

[95] Joël J Niederhauser, Michael Jaeger, Robert Lemor, Peter Weber, and Martin Frenz. Combined ultrasound and optoacoustic system for real-time high-contrast vascular imaging in vivo. *Medical Imaging, IEEE Transactions on*, 24(4):436–440, 2005.

[96] Di W Yang, Da Xing, Si H Yang, and Liang Z Xiang. Fast full-view photoacoustic imaging by combined scanning with a linear transducer array. *Optics express*, 15(23):15566–15575, 2007.

[97] Minghua Xu and Lihong V Wang. Analytic explanation of spatial resolution related to bandwidth and detector aperture size in thermoacoustic or photoacoustic reconstruction. *Physical Review E*, 67(5):056605, 2003.

[98] Stefan Preisser, Nigel L Bush, Andreas G Gertsch-Grover, Sara Peeters, Arthur E Bailey, Jeffrey C Bamber, Martin Frenz, and Michael Jaeger. Vessel orientation-dependent sensitivity of optoacoustic imaging using a linear array transducer. *Journal of biomedical optics*, 18(2):026011–026011, 2013.

[99] Bin Huang, Jun Xia, Konstantin Maslov, and Lihong V Wang. Improving limited-view photoacoustic tomography with an acoustic reflector. *Journal of biomedical optics*, 18(11):110505–110505, 2013.

[100] Guo Li, Jun Xia, Kun Wang, Konstantin Maslov, Mark A Anastasio, and Lihong V Wang. Tripling the detection view of high-frequency linear-array-based photoacoustic computed tomography by using two planar acoustic reflectors. *Quantitative imaging in medicine and surgery*, 5(1):57, 2015.

[101] Guo Li, Jun Xia, Lei Li, Lidai Wang, and Lihong V Wang. Isotropic-resolution linear-array-based photoacoustic computed tomography through inverse radon transform. In *SPIE BiOS*, pages 93230I–93230I. International Society for Optics and Photonics, 2015.

Bibliography

[102] Hsiao-Chun Amy Lin, Andrei Chekkoury, Murad Omar, Tobias Schmitt-Manderbach, Benno Koberstein-Schwarz, Timo Mappes, Hernán López-Schier, Daniel Razansky, and Vasilis Ntziachristos. Selective plane illumination optical and optoacoustic microscopy for postembryonic imaging. *Laser & Photonics Reviews*, 9(5):L29–L34, 2015.

[103] Philipp J Keller. Imaging morphogenesis: technological advances and biological insights. *Science*, 340(6137):1234168, 2013.

[104] Jan Huisken and Didier YR Stainier. Even fluorescence excitation by multidirectional selective plane illumination microscopy (mspim). *Optics letters*, 32(17):2608–2610, 2007.

[105] Philipp J Keller, Annette D Schmidt, Joachim Wittbrodt, and Ernst HK Stelzer. Reconstruction of zebrafish early embryonic development by scanned light sheet microscopy. *science*, 322(5904):1065–1069, 2008.

[106] Thomas A Planchon, Liang Gao, Daniel E Milkie, Michael W Davidson, James A Galbraith, Catherine G Galbraith, and Eric Betzig. Rapid three-dimensional isotropic imaging of living cells using bessel beam plane illumination. *Nature methods*, 8(5):417–423, 2011.

[107] Rui Ma, Martin Distel, X Luís Deán-Ben, Vasilis Ntziachristos, and Daniel Razansky. Non-invasive whole-body imaging of adult zebrafish with optoacoustic tomography. *Physics in medicine and biology*, 57(22):7227, 2012.

[108] Mathias Schwarz, Andreas Buehler, and Vasilis Ntziachristos. Isotropic high resolution optoacoustic imaging with linear detector arrays in bi-directional scanning. *Journal of biophotonics*, 9999, 2014.

[109] Andreas Buehler, X Luís Dean-Ben, Daniel Razansky, and Vasilis Ntziachristos. Volumetric optoacoustic imaging with multi-bandwidth deconvolution. *Medical Imaging, IEEE Transactions on*, 33(4):814–821, 2014.

[110] Jérôme Gateau, Marc Gesnik, Jean-Marie Chassot, and Emmanuel Bossy. Single-side access, isotropic resolution, and multispectral three-dimensional photoacoustic imaging with rotate-translate scanning of ultrasonic detector array. *Journal of biomedical optics*, 20(5):056004–056004, 2015.

[111] Jérôme Gateau, Andrei Chekkoury, and Vasilis Ntziachristos. High-resolution optoacoustic mesoscopy with a 24 mhz multidetector translate-rotate scanner. *Journal of biomedical optics*, 18(10):106005–106005, 2013.

[112] Subhamoy Mandal, X Luís Deán-Ben, and Daniel Razansky. Automated calibration of temporal changes in the speed of sound in optoacoustic tomography. In *European Conferences on Biomedical Optics*, pages 88000K–88000K. International Society for Optics and Photonics, 2013.

[113] Takamasa Iwaki, Hiroshi Yamashita, Toshiyuki Hayakawa, et al. *color atlas of sectional anatomy of the mouse=*. Adosuri, 2005.

[114] George Paxinos, Charles RR Watson, and Piers C Emson. Ache-stained horizontal sections of the rat brain in stereotaxic coordinates. *Journal of neuroscience methods*, 3(2):129–149, 1980.

[115] Jérôme Gateau, Andrei Chekkoury, and Vasilis Ntziachristos. Ultra-wideband three-dimensional optoacoustic tomography. *Optics letters*, 38(22):4671–4674, 2013.

[116] MI Khan and GJ Diebold. The photoacoustic effect generated by an isotropic solid sphere. *Ultrasonics*, 33(4):265–269, 1995.

[117] Nikolai V Sushilov and Richard SC Cobbold. Frequency–domain wave equation and its time–domain solutions in attenuating media. *The Journal of the Acoustical Society of America*, 115(4):1431–1436, 2004.

[118] Johannes Bauer-Marschallinger, Thomas Berer, Heinz Roitner, Hubert Grün, Bernhard Reitinger, and Peter Burgholzer. Ultrasonic attenuation of biomaterials for compensation in photoacoustic imaging. In *SPIE BiOS*, pages 789931–789931. International Society for Optics and Photonics, 2011.

[119] Patrick J La Rivière, Jin Zhang, and Mark A Anastasio. Image reconstruction in optoacoustic tomography for dispersive acoustic media. *Optics letters*, 31(6):781–783, 2006.

[120] Milton V Marshall, Daniel Draney, Eva M Sevick-Muraca, and D Michael Olive. Single-dose intravenous toxicity study of irdye 800cw in sprague-dawley rats. *Molecular Imaging and Biology*, 12(6):583–594, 2010.

[121] Adrian Taruttis, Stefan Morscher, Neal C Burton, Daniel Razansky, and Vasilis Ntziachristos. Fast multispectral optoacoustic tomography (msot) for dynamic imaging of pharmacokinetics and biodistribution in multiple organs. *PLoS One*, 7(1):e30491, 2012.

[122] Geng Ku, Xueding Wang, George Stoica, and Lihong V Wang. Multiple-bandwidth photoacoustic tomography. *Physics in medicine and biology*, 49(7):1329, 2004.

[123] Amir Rosenthal, Stephan Kellnberger, Dmitry Bozhko, Andrei Chekkoury, Murad Omar, Daniel Razansky, and Vasilis Ntziachristos. Sensitive interferometric detection of ultrasound for minimally invasive clinical imaging applications. *Laser & Photonics Reviews*, 8(3):450–457, 2014.

[124] Jan Laufer, Edward Zhang, Gennadij Raivich, and Paul Beard. Three-dimensional noninvasive imaging of the vasculature in the mouse brain using a high resolution photoacoustic scanner. *Applied optics*, 48(10):D299–D306, 2009.

[125] Stratis Tzoumas, Nikolaos Deliolanis, Stefan Morscher, and Vasilis Ntziachristos. Unmixing molecular agents from absorbing tissue in multispectral optoacoustic tomography. *Medical Imaging, IEEE Transactions on*, 33(1):48–60, 2014.

[126] Miguel Angel Araque Caballero, Jérôme Gateau, Xosé-Luis Déan-Ben, and Vasilis Ntziachristos. Model-based optoacoustic image reconstruction of large three-dimensional tomographic datasets acquired with an array of directional detectors. *Medical Imaging, IEEE Transactions on*, 33(2):433–443, 2014.

[127] Reinaldo Manalich, Leonardo Reyes, Mercedes Herrera, Clara Melendi, and Isabel Fundora. Relationship between weight at birth and the number and size of renal glomeruli in humans: a histomorphometric study. *Kidney international*, 58(2):770–773, 2000.

[128] Marco Feuerstein, Hauke Heibel, José Gardiazabal, Nassir Navab, and Martin Groher. Reconstruction of 3-d histology images by simultaneous deformable registration. In *Medical Image Computing and Computer-Assisted Intervention–MICCAI 2011*, pages 582–589. Springer, 2011.

[129] Rakesh K Jain. Determinants of tumor blood flow: a review. *Cancer research*, 48(10):2641–2658, 1988.

[130] Gabriele Bergers and Laura E Benjamin. Tumorigenesis and the angiogenic switch. *Nature reviews cancer*, 3(6):401–410, 2003.

[131] M Heijblom, JM Klaase, FM van den Engh, TG van Leeuwen, W Steenbergen, and S Manohar. Imaging tumor vascularization for detection and diagnosis of breast cancer. *Technology in cancer research & treatment*, 10(6):607–623, 2011.

[132] Donald M McDonald and Peter L Choyke. Imaging of angiogenesis: from microscope to clinic. *Nature medicine*, 9(6):713–725, 2003.

[133] Beatrice Nico, Vicenzo Benagiano, Doménica Mangieri, Nicola Maruotti, Angelo Vacca, and Doménico Ribatti. Evaluation of microvascular density in tumors, pro and contra. 2008.

[134] Se Hyung Kim, Aya Kamaya, and Jürgen K Willmann. Ct perfusion of the liver: principles and applications in oncology. *Radiology*, 272(2):322–344, 2014.

[135] Fabian Kiessling, Susanne Greschus, Matthias P Lichy, Michael Bock, Christian Fink, Silvia Vosseler, Jens Moll, Margareta M Mueller, Norbert E Fusenig, Horst Traupe, and W Semmler. Volumetric computed tomography(vct): a new technology for noninvasive, high-resolution monitoring of tumor angiogenesis. *Nature medicine*, 10(10):1133–1138, 2004.

[136] Tony Jeswani and Anwar R Padhani. Imaging tumour angiogenesis. *Cancer Imaging*, 5(1):131, 2005.

Bibliography

[137] Dmitriy Kedrin, Bojana Gligorijevic, Jeffrey Wyckoff, Vladislav V Verkhusha, John Condeelis, Jeffrey E Segall, and Jacco van Rheenen. Intravital imaging of metastatic behavior through a mammary imaging window. *Nature methods*, 5(12):1019–1021, 2008.

[138] RI Siphanto, KK Thumma, RGM Kolkman, TG Van Leeuwen, FFM De Mul, JW Van Neck, LNA van Adrichem, and Wiendelt Steenbergen. Serial noninvasive photoacoustic imaging of neovascularization in tumor angiogenesis. *Optics express*, 13(1):89–95, 2005.

[139] Murad Omar, Mathias Schwarz, Dominik Soliman, Panagiotis Symvoulidis, and Vasilis Ntziachristos. Pushing the optical imaging limits of cancer with multi-frequency-band raster-scan optoacoustic mesoscopy (rsom). *Neoplasia*, 17(2):208–214, 2015.

[140] Yeqi Lao, Da Xing, Sihua Yang, and Liangzhong Xiang. Noninvasive photoacoustic imaging of the developing vasculature during early tumor growth. *Physics in medicine and biology*, 53(15):4203, 2008.

[141] Nicolas Beziere, Neus Lozano, Antonio Nunes, Juan Salichs, Daniel Queiros, Kostas Kostarelos, and Vasilis Ntziachristos. Dynamic imaging of pegylated indocyanine green (icg) liposomes within the tumor microenvironment using multi-spectral optoacoustic tomography (msot). *Biomaterials*, 37:415–424, 2015.

[142] Joanne R Less, Thomas C Skalak, Eva M Sevick, and Rakesh K Jain. Microvascular architecture in a mammary carcinoma: branching patterns and vessel dimensions. *Cancer research*, 51(1):265–273, 1991.

[143] Rakesh K Jain. Molecular regulation of vessel maturation. *Nature medicine*, 9(6):685–693, 2003.

[144] Meng-Lin Li, Jung-Taek Oh, Xueyi Xie, Geng Ku, Wei Wang, Chun Li, Gina Lungu, George Stoica, and Lihong V Wang. Simultaneous molecular and hypoxia imaging of brain tumors in vivo using spectroscopic photoacoustic tomography. *Proceedings of the IEEE*, 96(3):481–489, 2008.

[145] Andrei Chekkoury, Jérôme Gateau, and Vasilis Ntziachristos. Multiple bandwidth volumetric optoacoustic tomography using conventional ultrasound linear arrays. In *European Conferences on Biomedical Optics*, pages 880003–880003. International Society for Optics and Photonics, 2013.